Observational Study of Gradual Solar Energetic Particle Events Focusing on Timescale

Kosuke Kihara

A thesis presented for the degree of

Doctor of Science

Astronomical Observatory

Kyoto University

Japan

January 2023

Observational Study of Gradual Solar Energetic Particle Events Focusing on Timescale

Kosuke Kihara

Abstract

Solar Energetic Particles (SEPs) are high-energy particles that originate from solar active phenomena. SEPs cause radiation hazards for astronauts and airline passengers or damage satellites, which results in serious social impacts. Therefore, it is an important subject in space weather research both scientifically and practically to elucidate the mechanism of SEPs and to forecast the occurrence of SEP events and, if it occurs, also arrival times and the scale of SEP events. One of the major origins of SEPs is considered to be coronal mass ejections (CMEs), in which the shock waves driven by CME accelerate the particles. The SEP events derived from CMEs are called "Gradual SEP events". In this thesis, in order to clarify the relationship between CMEs and gradual SEP events, especially what determines the timescales of SEPs, we studied gradual SEP events mainly focusing on the timescales. In Chapter 2, we compiled a large event list of SEPs and performed the statistical analysis. In Chapter 3, we extracted two events that are characterized by their timescales from our event list and investigated their observational characteristics in detail.

Chapter 2 presents a statistical study of SEP occurrences and timescales with respect to the CME source locations and speeds, considering all 257 fast ($v_{CME} \geq 900$ km s^{-1}) and wide (angular width $\geq 60°$) CMEs that occurred between December 2006 and October 2017. Examination of the source region of each CME reveals that CMEs more often accompany SEP events if they originate from the longitude of E20 – W100 relative to the observer. For the associated CME-SEP pairs, we measure three timescales for each of the SEP events: (1) TO, the SEP onset time at 1 AU with respect to the CME launch, (2) TR, the rise time from the SEP onset time to the SEP half-peak during the rising phase, and (3) TD, the duration between SEP half-peak during the rising and declining phases. They are correlated with the longitude of the CME source region relative to the footpoint of the Parker spiral ($\Delta\Phi$) and v_{CME}. TO tends to be short for $|\Delta\Phi| < 60°$. A similar trend is seen in TR and TD, but weaker, and they are more continuously distributed. The SEP timescales are only weakly correlated with v_{CME}. Positive correlations of both TR and TD with v_{CME} are seen in poorly connected (large $|\Delta\Phi|$) events. Additionally, TO appears to be negatively correlated with v_{CME} for events with small $|\Delta\Phi|$.

In Chapter 3, we focused on TO, which has a distribution of at least an order of magnitude, even when the source region is not far from the well-connected longitudes. We studied two SEP events from the western hemisphere that are different in TO on

the basis of >10 MeV proton data from the Geostationary Operations Environmental Satellite, despite similar in the CME speed and longitude of the source regions. We tried to find the reasons for different TO, or proton release times, in how the CME-driven shock develops and the Alfvén Mach number of the shock wave reaches some threshold, by combining the CME height-time profiles with radio dynamic spectra. We also discussed how CME-CME interactions and active region properties may affect proton release times.

Supervisor: Ayumi Asai

Acknowledgements

Foremost, I would like to express my sincere gratitude to my supervisor Prof. Ayumi Asai. Thanks to her excellent support, I was able to complete my Ph.D. course in a field that interested me. I appreciate Dr. Nariaki V. Nitta, Dr. Seiji Yashiro, and Prof. Kiyoshi Ichimoto. Without their contributions, I would not have been able to accomplish my study. I also appreciate all the members of the Astronomical Observatory and Department of Astrophysics of Kyoto University for their helpful comments, fruitful discussion, and kind support beyond the research. I would like to thank especially my colleagues Daiki Yamasaki and Yuji Kotani. We enhanced each other not only academically but also in our personal lives throughout the Ph.D. course.

The majority of my study is based on the discussion at the Coordinated Data Analysis Workshops held in August 2018 and 2019 held under the auspice of the Project for Solar-Terrestrial Environment Prediction (PSTEP). This work is supported by JSPS KAKENHI grant No. JP22J11442 and also by the joint research project of the Unit of Synergetic Studies for Space, Kyoto University, and BroadBand Tower, Inc. (BBT).

Last but not least, I would like to thank my family for their dedication and support throughout my life.

Contents

List of Figures vi

List of Tables viii

1 General introduction 1

1.1 Flares, CMEs, and SEPs 1

1.1.1 Overview 1

1.1.2 Solar Flares 3

1.1.3 Coronal Mass Ejections 8

1.1.4 Two Class Paradigm of SEP 10

1.2 Gradual SEP events 13

1.2.1 Motivation 13

1.2.2 Gradual SEP and CME 14

1.2.3 Timescale of SEP 16

1.2.4 Aim of this Thesis 16

2 Statistical Analysis of the Relation between Coronal Mass Ejections and Solar Energetic Particles 18

2.1 Introduction 18

2.2 Event List 19

2.3 SEP Association of Fast and Wide CMEs 22

2.4 SEP Timescales 29
2.5 Discussion 34
2.6 Summary 37

3 Solar Energetic Particle Events with Short and Long Onset Times 54

3.1 Introduction 54
3.2 Observations 56
3.2.1 Event Selection 56
3.2.2 Overview of the Events 57
3.3 Further Analysis of SEP Events 60
3.4 Factors that may control the particle release time 63
3.4.1 Evolution of Shock Waves with Height 63
3.4.2 CME-CME Interaction 65
3.4.3 Properties of the Active Regions 67
3.5 Summary 70

4 Concluding Remarks 72

4.1 Conclusion 72
4.2 Future Direction 73

Bibliography 75

List of Figures

1.1 The particle storm observed by C3 on the SOHO/LASCO on 14 Jul 2000. . . 2

1.2 A typical time profile of a solar flare in various wavelengths from radio to X-ray. 3

1.3 Schematic representation of flare reconnection model. 4

1.4 A soft X-ray image of a cusp-shaped loop structure in a solar flare observed by Yohkoh satellite. 5

1.5 The illustration of the sequence of solar flares in impulsive (left) and gradual (right) phases. 6

1.6 The examples of solar radio bursts. 7

1.7 (a) The classical three-part structure of a CME. (b) A typical observation of a halo CME. 9

1.8 Schematic illustrations of the acceleration mechanism and the typical time profile of two classes of SEP events. 11

1.9 Correlation between CME speed and peak proton flux. 14

1.10 Three cases of the behavior of protons when CMEs are observed from different locations. 15

2.1 Distribution of CMEs with source longitude (in 20° bins) relative to the observer 23

2.2 Distribution of CMEs with speed in 200 km s^{-1} bins 25

2.3 SEP heat maps, showing how the SEP association rate varies with the source longitude and speed of the CMEs 26

2.4 Correlations between the parameters of flare, CME, and SEP. 28
2.5 An example showing the four timescales defined in the text 30
2.6 (a) SEP onset time from the CME launch (TO) vs the longitude of the CME source region relative to the footpoint of the Parker spiral. (b) and (c) The same plot, but for the SEP rise time TR and SEP duration TD 31
2.7 SEP onset time TO vs CME speed (v_{CME}) 32
2.8 SEP rise time TR vs CME speed (v_{CME}) 33
2.9 SEP duration TD vs CME speed (v_{CME}) 33
2.10 SEP onset time TO vs peak proton flux 34

3.1 The soft X-ray (SXR) and the integrated flux of >10 MeV protons observed by GOES satellite. 58
3.2 Radio dynamic spectra of the two events in the combined metric and DH ranges. 59
3.3 Low coronal and coronagraph images. 60
3.4 VDA analysis based on ERNE/HED data. 61
3.5 Summary of the timeline. 62
3.6 Shock speed profile and M_A profiles. 66
3.7 The observations of the solar surface at each event. 68
3.8 The decay index vs height for the regions. 69

List of Tables

1.1 Properties of Gradual and Impulsive SEP Events 12

2.1 Properties of Fast and Wide CMEs and Associated SEP Events 38

2.2 Timescales of SEP Events 48

3.1 Basic Parameters of the Two SEP Events 57

CHAPTER 1

General introduction

1.1 Flares, CMEs, and SEPs

1.1.1 Overview

Solar Energetic Particles (SEPs) are high-energy particles or events that observe particles originating from solar active phenomena. It is known that protons, electrons, and heavy ions from He to Fe are accelerated from a few keV to a maximum of a few GeV. High-energy particles are found not only in the solar phenomena but everywhere in the universe, but the question of what is the source of the high-energy particles is a common and difficult problem unsolved across all fields of astrophysics.

SEP event was first reported by Forbush (1946). Forbush discovered that ion chambers on the ground, which observe secondary particles generated when galactic cosmic rays interact with the Earth's atmosphere, showed an irregular rise three times in 1942 Feb 28, in 1942 Mar 7, and in 1946 Jul 25. High-energy particles from space are usually not observed on the ground because the Earth's atmosphere acts as a "shelter". However, extreme SEPs accelerated to a few GeV rarely intrude into the Earth's atmosphere and generate secondary particles, which result in SEPs being observed indirectly on the ground. These events are now called Ground Level Enhancement (GLE) events and are an important research subject as extreme events of SEPs (e.g., Gopalswamy et al., 2012). Forbush noted that these irregular rises occurred when the active region of the Sun was toward the Earth and suggested that those high-energy particles are derived from the Sun.

Environmental changes in near-Earth space caused by solar active phenomena such as high-energy particles are called space weather. In a modern society in which human beings advance into space and make extensive use of space, space weather disasters can cause very serious damage to our infrastructure. The radiation hazard due to SEPs is one of the most serious incidents in space weather along with the electromagnetic radiation

from solar flares (see Section 1.1.2) and the geomagnetic storms from coronal mass ejections (CMEs; see Section 1.1.3). The National Oceanic and Atmospheric Administration (NOAA) has announced three space weather scales, including "solar radiation storms." There are five scales from S1 "Minor" to S5 "Extreme" according to the flux level of >10 MeV particles observed by GOES satellite*. Each scale covers three areas (biological, satellite operations, and other systems such as high-frequency communications) and characterizes the severity of the effects. High-energy particles exceeding several tens of MeV cause serious radiation damage for astronauts operating in space with very little shielding (Malandraki & Crosby, 2018). In the polar regions of the Earth, magnetic field lines are open and particles from interplanetary space are easily accessible, which can cause radiation damage to the crews of aircraft navigating at high latitudes. In addition, high-energy particles provide noise to the satellite imaging data and cause the abnormality or failure of semiconductor devices, called single event effects. It is sometimes observed as a "particle storm" (see Figures 1.1) in the coronagraph C2/C3 on board the Large Angle and Spectrometric Coronagraph Experiment (LASCO; Brueckner et al., 1995) of the Solar and Heliospheric Observatory (SOHO; Domingo et al., 1995) satellite.

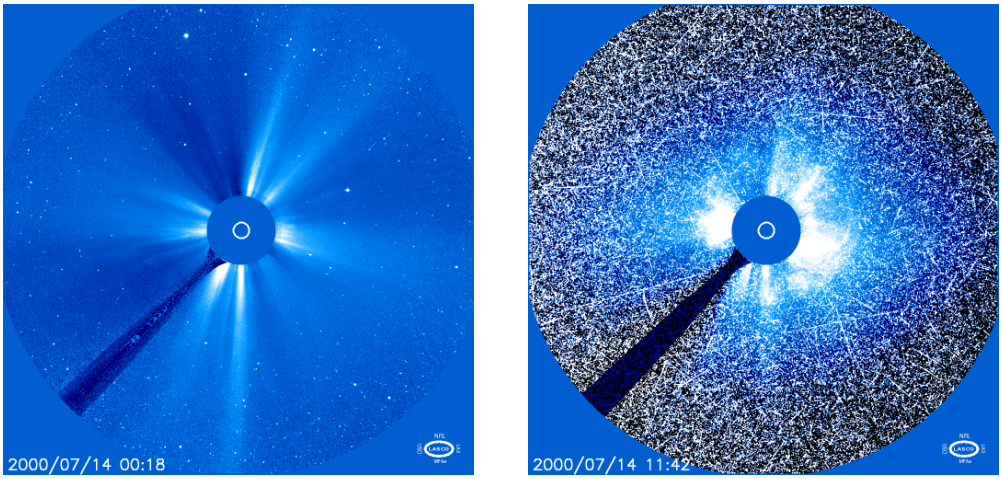

(a) (b)

Figure 1.1: The particle storm observed by the coronagraph C3 on the SOHO/LASCO on 14 Jul 2000. (a) Before the particle storm and (b) during the storm. Cited from https://soho.nascom.nasa.gov/hotshots/2000_07_14/.

This section briefly introduces the solar active phenomena and reviews the discussion of the origin of SEPs, focusing on solar flares and coronal mass ejections (CMEs), which are the two major sources of SEPs in their simplest classification.

*https://www.swpc.noaa.gov/noaa-scales-explanation

1.1.2 Solar Flares

Solar flares are sudden brightening phenomena observed in the solar atmosphere. The first observation of a solar flare was carried out in white light by Carrington (1859) or Hodgson (1859). The brightening of a solar flare is often observed in wide wavelengths such as radio waves, visible, ultraviolet, and X-rays, as shown in Figure 1.2 (Kane, 1974). Solar flares also release energy in various forms such as radiation, kinetic, thermal, and non-thermal, and the amount of release energy is as much as $10^{28} - 10^{32}$ erg during minutes to hours (Benz, 2017).

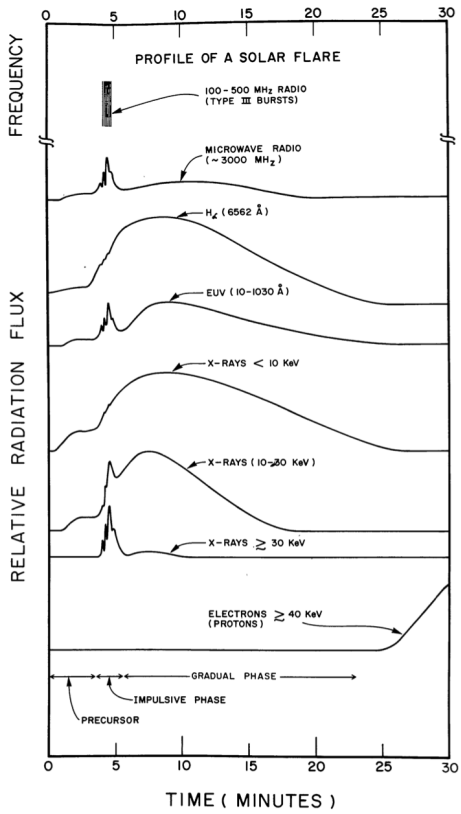

Figure 1.2: A typical time profile of a solar flare in various wavelengths from radio to X-ray. Cited from Kane (1974)

It is now widely accepted that solar flares are caused by magnetic reconnection in the solar corona (Shibata & Magara, 2011). Magnetic reconnection is a phenomenon in which the topology of the magnetic field is changed by the reconnection of antiparallel magnetic fields to a state of lower energy. A part of the magnetic energy released in magnetic reconnection is observed as a brightening in solar flares. Since the late 1940s, the theory that solar flares occur due to magnetic reconnection has been proposed (Giovanelli, 1946;

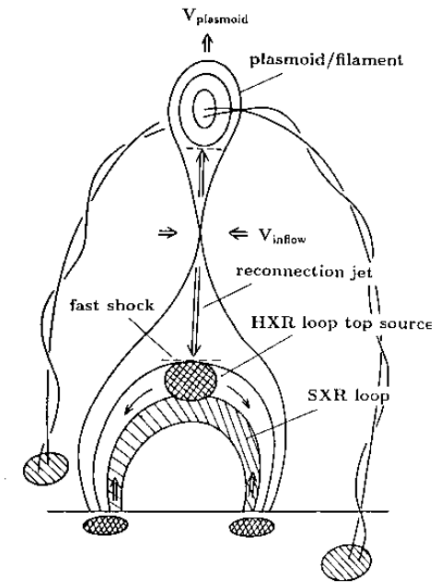

Figure 1.3: Schematic representation of flare reconnection model. Note that this is not the original CSHKP model but is modified with the findings of later observation so that it includes the process of a plasmoid/filament eruption. Cited from Shibata et al. (1995).

Hoyle, 1949; Sweet, 1958; Parker, 1957; Petschek, 1964). The current "standard model" for describing solar flares is called CSHKP model (see Figure 1.3), named after the pioneers who contributed to the model construction (Carmichael, 1964; Sturrock, 1966; Hirayama, 1974; Kopp & Pneuman, 1976). This model was supported by the observations in the 1990s (Figure 1.4; Tsuneta et al., 1992; Tsuneta, 1996; Forbes & Acton, 1996) thanks to the launch of the Yohkoh satellite (Ogawara et al., 1991). In addition, it has been proposed that many solar phenomena accompanied by brightening or eruption in different spatial scales and time scales can be explained by one model (unified model) using magnetic reconnection, and this model is now common (Shibata et al., 1995; Shibata, 1996, 1997, 1999).

Solar flares are often associated with plasma ejections. An example of what is ejected is a prominence, which is a cool ($\sim 10^4$ K) and dense plasma structure floating in the solar corona ($>10^6$ K). A prominence is observed as a dark structure sometimes called "filament" for example in the Hα line. A prominence inside an active region is short-lived and can erupt in minutes to hours, while a prominence outside an active region is relatively stable and typically exists for several weeks. It is sometimes observed that a prominence rises and erupts or it disappears without being observed. These are called "prominence (filament) eruption" or "prominence (filament) disappearance". The erupted prominence (or a plasmoid, a bubble of plasma that is not so cold as prominence) sometimes escapes

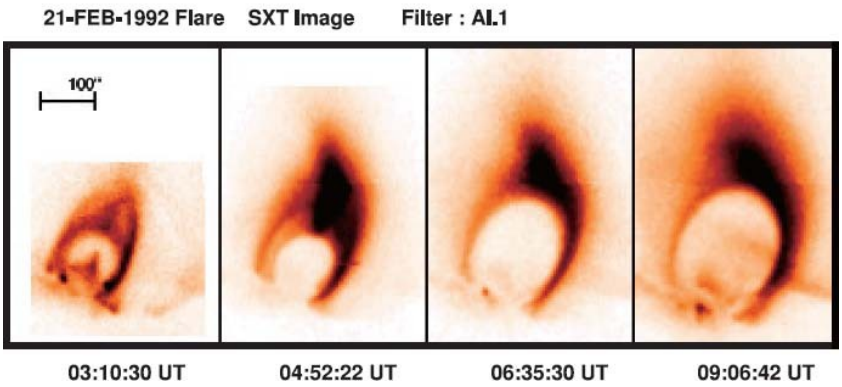

Figure 1.4: A soft X-ray image of a cusp-shaped loop structure in a solar flare observed by Yohkoh satellite (Tsuneta et al., 1992; Tsuneta, 1996). The colored region is the area that emits soft X-rays and is consistent with the lower structure of the reconnection model. Cited the modified version (contrast is shown in reversed) from Shibata & Magara (2011).

from the Sun's gravity and can be ejected into interplanetary space with the plasma in the corona. This phenomenon is thought to be strongly linked to coronal mass ejection (CME) and is described in Section 1.1.3. This series of processes can be described by the CSHKP model or the unified model. Figure 1.5 illustrates the sequence of solar flares in two phases (or two types). As shown in Figure 1.2, at the start of a flare, an impulsive phase (the left of Figure 1.5) represented by the emission of hard X-ray (HXR) or microwave continues for several minutes, and then it shifts to a gradual phase (the right of Figure 1.5) in which soft X-ray (SXR) or Hα is dominant. As a prominence (or a plasmoid) rises, extended antiparallel magnetic field lines are pressed down at the bottom of the prominence, causing intermittent magnetic reconnection. This reconnection generates high-speed outflows in the vertical direction, and the upward flow itself accelerates the prominence eruption. Due to the downward flow of energetic electrons generated in the reconnection region and thermal conduction, chromospheric plasma is heated to 10^7 K. This causes the chromospheric plasma to move up and down while being trapped by the magnetic flux tube due to the increased gas pressure so that the magnetic loop is observed as an SXR loop. A phenomenon in which the heated plasma rises from the chromosphere to the corona is called "chromospheric evaporation" (Fisher et al., 1985). The foot of the loop is also heated to 10^4 K, and two ribbons (or flare ribbons, Hα ribbons) are observed in the Hα line. The SXR loops are then cooled by radiation, and the low temperature ($\sim 10^4$ K) loops are sometimes observed in Hα.

In general, the existence of high-energy particles cannot be directly detected by any methods other than observing particles that reach the observer, but observational evidence has been found suggesting that various types of particle acceleration can occur in solar flares.

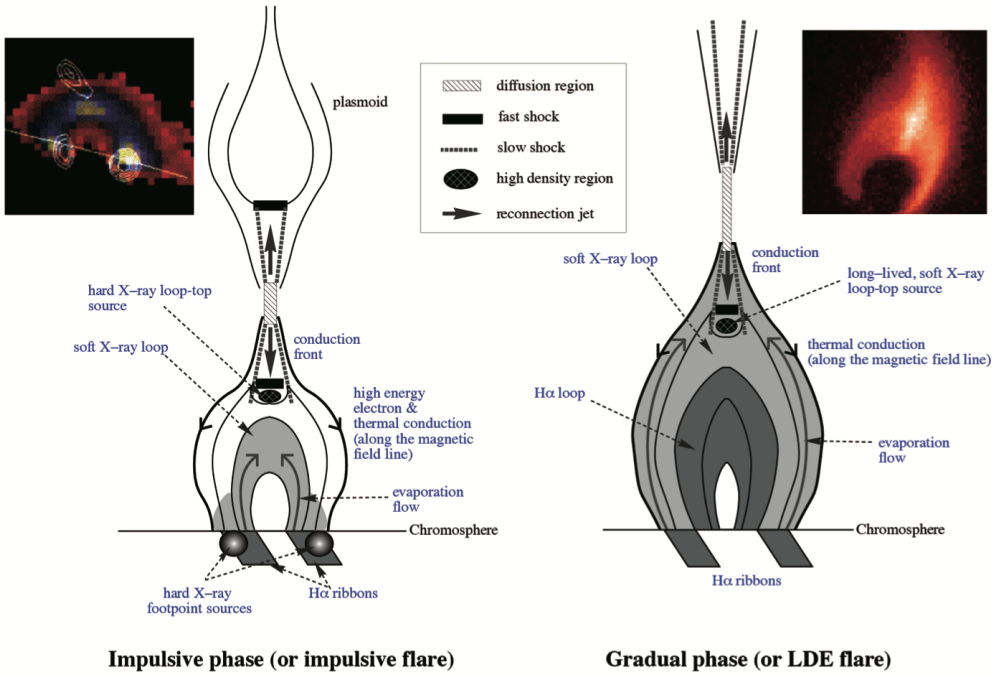

Figure 1.5: The illustration of the sequence of solar flares in impulsive (left) and gradual (right) phases. The source regions of various emissions are also shown. Cited from Shibata & Magara (2011) but the original version of schematic illustration and the observational examples originate from Magara et al. (1996), Masuda et al. (1994) (top left), and Tsuneta (1996) (top right), respectively.

For example, HXR emission sources observed at the foot of the SXR loop are believed to be due to bremsstrahlung by the high-energy electrons accelerated in the reconnection region and descending along the magnetic field of the SXR loop. HXR emission has also been detected at the top of the SXR loop (Masuda et al., 1994). It is considered that a downward flow derived from reconnection generates a shock wave at the top of the SXR loop to form an acceleration region of high-energy particles. Although the particle acceleration mechanism at this location is not yet clear, it is a piece of important observational evidence that solar flares are derived from magnetic reconnection and generate reconnection outflow. These high-energy electrons radiate microwaves due to gyrosynchrotron motion as they move along the magnetic loop. Furthermore, as high-energy electrons move upward through the solar atmosphere along the open magnetic fields, the instability caused by electron beams with different speeds generates Langmuir waves (Ginzburg & Zhelezniakov, 1958). They are converted to electromagnetic radiation and produce radio emissions at the local plasma frequency (and two times that frequency) (e.g., Reid & Ratcliffe, 2014). Thus, solar radio bursts, classified as “type III” among several types, are often observed. Type III radio bursts are characterized by strong and short-duration emis-

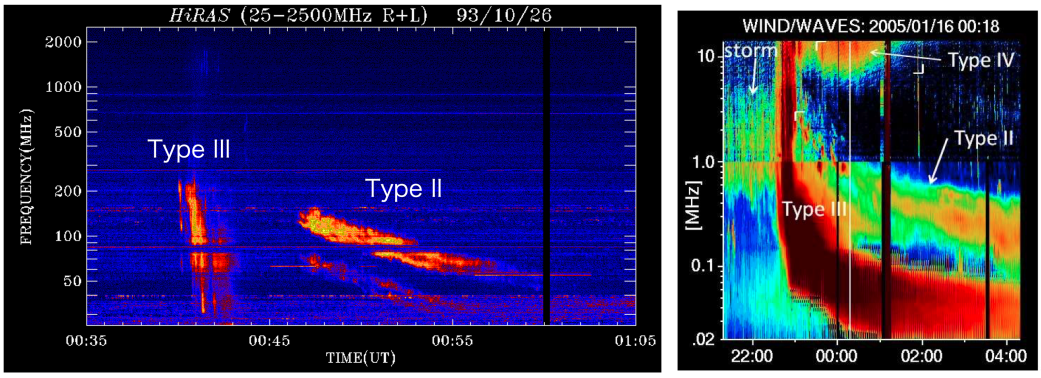

(a) (b)

Figure 1.6: The examples of solar radio bursts. (a) Typical type II and III radio bursts by Hiraiso RAdio Spectrograph (HiRAS) ground-based observation. (b) Type II, III, and IV radio bursts observed by the Radio and Plasma Wave Experiment (WAVES; Bougeret et al., 1995) on the Wind spacecraft. "Type IV" radio bursts, which are not described in the text are thought to be derived from synchrotron radiation from high-energy electrons trapped in closed magnetic loops. The difference between the two panels is the observed frequencies, i.e., the local plasma frequencies. Since the source of emissions is (a) in the solar corona and (b) in interplanetary space, the latter is often called interplanetary radio bursts. The original image of (a) is extracted from `https://sunbase.nict.go.jp/solar/denpa/hiras/gif/93102600.gif` and (b) is cited from Gopalswamy et al. (2019).

sions over a wide range of frequencies immediately after the occurrence of solar flares (see Figure 1.6).

Coronal shock waves are frequently observed in association with solar flares. The earliest observation of wave propagation is carried out in Hα line (Moreton, 1960; Moreton & Ramsey, 1960; Athay & Moreton, 1961) and is called Moreton wave. It is widely accepted that it is derived from fast-mode MHD shock waves propagating in the solar corona (Uchida, 1968). Also in other wavelengths, those observed in extreme ultraviolet (EUV) range (e.g., Moses et al., 1997; Thompson et al., 1998; Chen & Wu, 2011) are called EUV waves, and in SXR range (e.g., Khan & Hudson, 2000) are called X-ray waves. Although there have been many simultaneous observations suggesting relationships between them (e.g., Khan & Aurass, 2002; Narukage et al., 2002; Asai et al., 2012), it is still unclear what drives the shock waves in the solar corona. The coronal shock waves are believed to cause radio emissions at high frequencies (typically several tens to hundred MHz) through plasma oscillation of electrons and are responsible for "type II" radio bursts. Type II radio bursts are characterized by drifting of observed frequencies with time as the shock wave propagates (Figure 1.6), which is often discussed in correlation with Morton waves (e.g., Uchida, 1974) and EUV waves (e.g., Nitta et al., 2013, 2014; Muhr et al., 2014), and especially with CMEs described in Section 1.1.3.

1.1.3 Coronal Mass Ejections

Coronal mass ejection (CME) is a phenomenon in which a magnetized plasma is ejected from the solar atmosphere into interplanetary space, and is observed mainly by white light coronagraphs. CME was first observed by the coronagraph on board Orbiting Solar Observatory 7 (OSO-7; Koomen et al., 1975) from 13 to 14 December 1971 (Tousey, 1973), delayed from the detection of flares and SEPs. OSO-7 subsequently observed ∼30 CMEs by 1974. The next mission which continuously observed CMEs was NASA's Skylab. Gosling et al. (1974) reported in detail the morphology and the speed of more than 30 CMEs observed by the Skylab mission. From the latter half of the 1970s to the 1980s, Solwind white light coronagraph on P78-1 satellite and Solar Maximum Mission (SMM) satellite respectively observed >1000 CMEs (e.g., Howard et al., 1985; Hundhausen, 1993). The primary CME observations at present are carried over to C2/C3 on board SOHO/LASCO launched in 1996, and COR1/COR2 on board the Sun-Earth Connection Coronal and Heliospheric Investigation (SECCHI; Howard et al., 2008) of the Solar-Terrestrial Relations Observatory (STEREO; Kaiser et al., 2008) satellite launched in 2006.

Previous observations have shown that CMEs typically have a "three-part" structure consisting of a leading edge, core, and cavity (Illing & Hundhausen, 1985, see also Figure 1.7(a)). The outermost dense plasma "shell" is called a leading edge (or a bright front) and is the region where the flux rope, detached from the solar surface, sweeps the plasma in interplanetary space. The speed of a CME is generally measured by tracking this leading edge. The innermost bright feature, called the core, is believed to be a prominence because it is often observed in Hα line. Many previous studies (e.g., Munro et al., 1979) have investigated how CMEs are related to prominence eruptions and the correlations have been reported to vary from a few % to almost 100% (Al-Omari et al., 2010, and references therein) (see also Parenti, 2014, for review). The CME width, i.e., how wide the CMEs are observed on the field of view (FOV) of the coronagraph, is one of the indicators of the magnitude of CMEs. In particular, a CME covering the whole occulting disk of the coronagraph is called "Halo CME" (Howard et al., 1982, Figure 1.7(b)), where the CME is ejected along the Sun-observer line (or is ejected from the opposite of the solar surface to the observer).

Since LASCO was launched, more than 30000 CMEs have been observed and they are summarized in the LASCO CME catalog* (Yashiro et al., 2004). According to the major statistics using LASCO observation data (e.g., Yashiro et al., 2004; Gopalswamy et al., 2009), the speed of CMEs is ∼30 km s^{-1} at minimum and ∼3000 km s^{-1} at maximum. The average is ∼450 km s^{-1}, but depending on the 11-year solar cycle; it is ∼300 km s^{-1} in the solar minimum and ∼500 km s^{-1} in the solar maximum. Approximately 3% of all

*https://cdaw.gsfc.nasa.gov/CME_list/

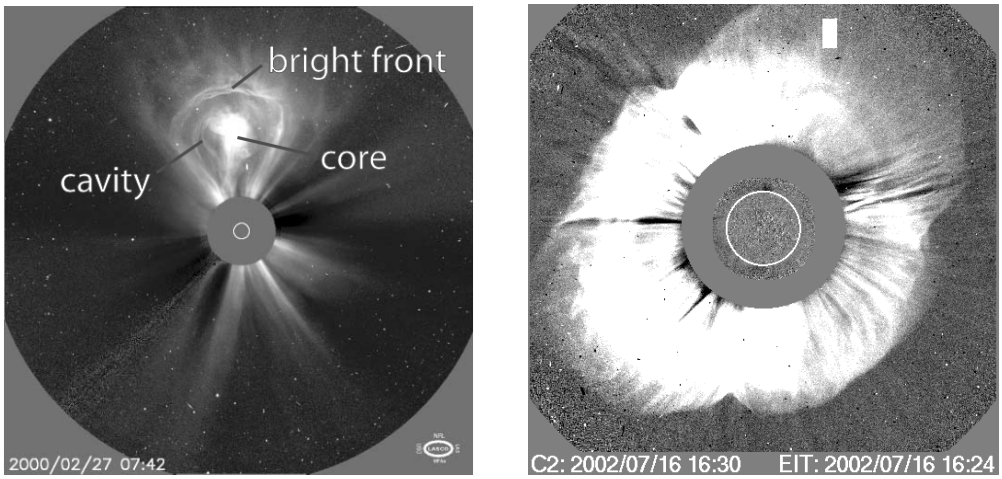

(a) (b)

Figure 1.7: (a) The classical three-part structure of a CME. The "bright front" corresponds to the leading edge of a CME. Cited from Riley et al. (2008) (b) A typical observation of a halo CME observed by the C2 coronagraph on board SOHO/LASCO. The image is the running difference between the two observations. The white ejecta covers the occulting disk. The running difference of the extreme ultraviolet (EUV) image observed by Extreme-Ultraviolet Imaging Telescope (EIT; Delaboudinière et al., 1995) of SOHO is shown inside the occulting disk, and the white circle is the limb of the Sun. Extracted from the LASCO CME catalog (Yashiro et al., 2004)

CMEs are Halo CMEs with an average speed of $\sim$900 km s^{-1}.

The ejection of magnetized plasma by a CME is one of the sources of disturbances in space weather. The CME ejected into interplanetary space is called interplanetary CME and it propagates in interplanetary space with a magnetic field detached from the solar surface, forming a shock wave in front of it. When a CME is released toward the Earth (i.e., observed as a Halo CME in most cases), it reaches the Earth within a few days. If the magnetic field associated with the released CME is southward, in other words, in the opposite direction of the Earth's magnetic field, a geomagnetic storm can occur (e.g., Gosling et al., 1991). For example, most of the intense geomagnetic storms that occurred in solar cycle 23 were caused by halo CMEs with a source near the central meridian of the Sun (Gopalswamy, 2010). The Carrington Flare, which occurred in 1859 and was the first observed flare event (Carrington, 1859), also generated the largest geomagnetic storm in the observation history which is considered to be originating from the associated CME (Tsurutani et al., 2003).

1.1.4 Two Class Paradigm of SEP

In the history of solar observations, it would have been natural to assume that solar flares were the primary cause of disturbances in interplanetary space and space weather effects on the Earth, given that the explosive phenomena known as solar flares were first detected and CMEs were observed more than 100 years later. However, even if a filament erupts with a solar flare, it cannot always reach interplanetary space, and a solar flare is not always accompanied by a CME. On the other hand, even if a rapid brightening as a flare is not observed, a CME can be observed (Webb & Howard, 2012; Parenti, 2014). In addition, as a unified model using magnetic reconnection has been constructed, it has been considered that solar flares and CMEs are related phenomena. They are only from different aspects of a single magneto-hydrodynamic energy release phenomenon and one does not cause the other.

The idea that solar flares are the primary cause of interplanetary disturbances such as SEPs, the so-called "Solar Flare Myth" (Gosling, 1993), has long been the subject of discussion. However, as it becomes clear that flares and CMEs are different aspects of a single phenomenon, the different ideas of the origin of SEPs are gradually becoming clear. It was radio observations that first showed that there can be two distinct processes for high-energy particles from the Sun. Wild et al. (1963) proposed that electrons are related to type III radio bursts and protons are related to type II radio bursts. Each type of radio burst is currently associated with solar flares and CMEs, respectively.

Soon after the discovery of CMEs, it was found that they were essential for the occurrence of proton events (Kahler et al., 1978). Moreover, it became clear that 26/27 cases of the proton event associated with solar flares were also associated with CMEs, and the speed and the width of CMEs were found to be correlated with the peak proton flux (Kahler et al., 1984). The close relationship between proton events and CMEs gradually collapses the "Solar Flare Myth". Besides, the idea that there are two origins of SEPs began to emerge. Pallavicini et al. (1977) distinguished SXR flares into impulsive events and long-duration events (LDE), although both of which are now described together by the unified model, and LDE flares were associated with CMEs (Sheeley et al., 1975). Cane et al. (1986) showed that the SEP events associated with impulsive flares and LDE flares (i.e., CMEs) exhibit different characteristics in electron/proton ratio and radio observations. Thus, in the late 1990s, the "two-class paradigm" of SEPs began to be accepted (Reames, 1999, 2013).

The mechanism and observational features of two classes of SEPs, gradual SEP and impulsive SEP, are shown in Figure 1.8 and Table 1.1. Gradual SEP is thought to be derived from particles accelerated by the shock wave driven by the CME, and impulsive SEP is thought to be derived from particles accelerated in the reconnection region of the solar

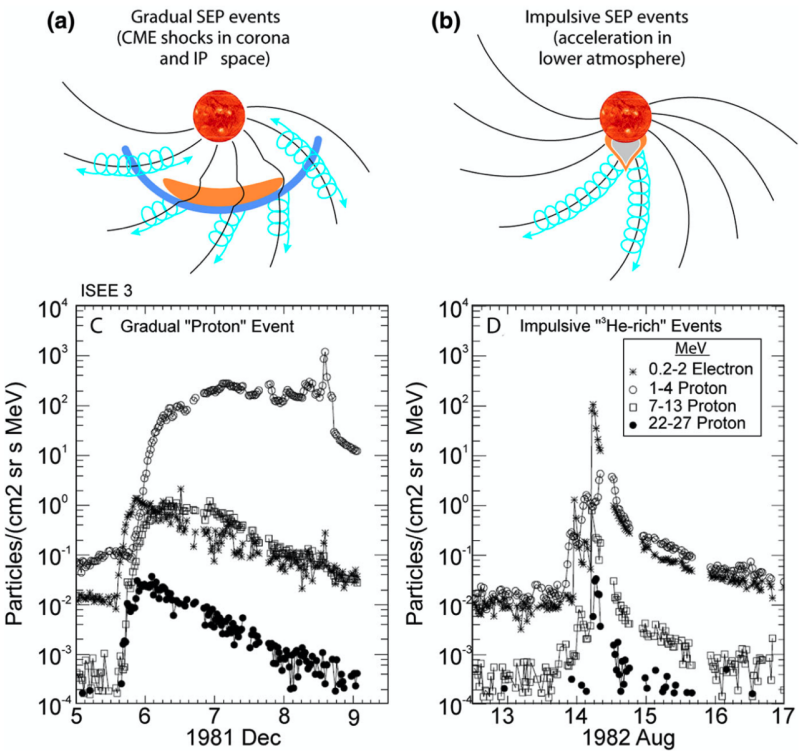

Figure 1.8: Schematic illustrations of the acceleration mechanism (top) and the typical time profile (bottom) of gradual SEP events ((a) and (c)) and impulsive SEP events ((b) and (d)). Cited from Desai & Giacalone (2016) but the original figures are from Reames (1999).

flare. Figure 1.8(a) shows that the accelerated particles are transported over a wide area by the widely spread shock wave driven by the CME, whereas the particles accelerated in solar flares are only transported and observed along the limited field lines extending therefrom (Figure 1.8(b)).

The events shown at the bottom of Figure 1.8 are (c) a proton event generated by a CME derived from a filament eruption without solar flares, and (d) a ^{3}He-rich event derived from impulsive flare without CMEs (Reames, 1999). A typical difference between the two is in their timescales. In gradual SEP events, particles are continuously accelerated by the shock wave driven by the associated CME, so that particles are observed for a long time. In impulsive SEP events, a short-time electron peak associated with acceleration in flare is observed, and the duration is determined by the scattering of particles during propagation in interplanetary space. The event rate of SEP events depends on the solar cycle, but at the solar maximum, it is about 10 events per year for gradual SEP events and about 1000 events per year for impulsive SEP events (Reames, 1995). The elemental

composition ratio is also an important difference that separates the two classes. Impulsive SEP events are sometimes referred to as electron-rich events or ^{3}He-rich events. In this classification, $\sim$1 – 100 keV electrons are dominant and the electron/proton ratio is high. The Fe/O and ^{3}He/^{4}He ratios are about 10 and 1000 times the typical coronal values, respectively. In addition, the ionization rate of iron is $\sim$20, and may simply originate from a high-temperature region of $\sim 10^7$ K during magnetic reconnection of solar flares. In gradual SEP events, the proton ratio is high, but Fe/O, ^{3}He/^{4}He, and the ionization rate of iron typically indicate an average value of the solar corona. On the other hand, events in which typical features of both are mixed have also been observed. For example, it has been reported that an increase in ^{3}He is also detected in the particle acceleration derived from interplanetary shock waves and is not necessarily limited to impulsive SEP events (Desai et al., 2001), that the high ionization rate of iron is also observed in gradual SEP events (e.g., Leske et al., 1995; Oetliker et al., 1997), and that there are impulsive SEP events associated with CMEs (e.g., Nitta et al., 2006). Cane et al. (2010) found that the features of 280 $\sim$25 MeV proton events observed from 1997 to 2006 are not simply separated into two groups, but are continuously distributed, and proposed that both flares and CMEs contribute to large SEP events (Cane et al., 2010, and references therein).

Table 1.1: Properties of Gradual and Impulsive SEP Events. Data are extracted from Desai & Giacalone (2016) but some data originate in Reames (1995) and Kallenrode (2003).

Property	Gradual SEP	Impulsive SEP
Electron/Proton	$\sim$50 – 100	$\sim 10^2 - 10^4$
^{3}He/^{4}He	$\sim 4 \times 10^{-4}$	~ 1
Fe/O	~ 0.1	~ 1
Ionization rate of iron	$\sim$14	$\sim$20
SEP Duration	$<$1 – 3 days	$<$1 – 20 h
Seed Particles	Ambient Corona or Solar Wind	Heated Corona
Radio type	II	III
X-ray duration	$\gtrsim$1 h	$\sim$10 min – 1 h
Coronagraph	CME	–
Event rate	$\sim$10 / year	$\sim$1000 / year

As described above, the acceleration mechanism of high-energy particles is one of the major unsolved problems in the whole of astrophysics. Three acceleration mechanisms that are considered to contribute to the generation of SEPs are only briefly introduced here (see also Miller et al., 1997; Aschwanden, 2002; Desai & Giacalone, 2016; Klein & Dalla, 2017, for review). The first mechanism is electric DC field acceleration by a strong direct

current (DC) generated by magnetic reconnection. It is effective for the acceleration of $\sim$100 keV electrons in the reconnection region of solar flares and is considered the main source of electrons in impulsive SEP events. The second mechanism, called stochastic acceleration or second order Fermi acceleration, is that particles gain energy in the long term while repeating the gain and loss of energy in the short term due to interaction with complex electromagnetic fields caused by turbulence or wave resonance. This is also considered to be related to turbulent flow associated with magnetic reconnection of solar flares and contributes to impulsive SEP events. The third one is shock acceleration, which can be divided into Shock-Drift Acceleration and Diffusive Shock Acceleration (first order Fermi acceleration). In the former mechanism, at quasi-perpendicular shock (i.e., the shock normal and the upstream magnetic field make a large angle), particles gain energy from an electric field $\mathbf{E} = -\mathbf{V} \times \mathbf{B}$, where $\mathbf{V}$ is the particle speed and $\mathbf{B}$ is the magnetic field upstream of the shock wave. In the latter, particles gain energy from the velocity difference between upstream and downstream as they move back and forth through the shock front due to the turbulent flow. The major contribution of shock acceleration is the gradual SEP events by the shock wave driven by CMEs. On the other hand, the existence of shock waves, such as termination shock due to the collision of the reconnection outflow of the flare and the magnetic loop, has been suggested everywhere in solar active phenomena, and it is conceivable that the shock acceleration accompanying solar flares can also contribute more or less to SEPs. Therefore, these acceleration mechanisms cannot completely correspond to the classification of SEPs and may cause a large event-to-event variation of SEPs.

1.2 Gradual SEP events

1.2.1 Motivation

Many unsolved problems such as acceleration mechanisms and elemental compositions remain for the two classes of SEPs. Among them, it is crucial to forecast the occurrence and arrival of SEPs in light of the active use of space in recent years. Even though numerous SEP models have been developed and efforts have been made to forecast SEPs (e.g., Whitman et al., 2022, and references therein), reliable SEP forecasting has not been successful even after the observation of possibly associated solar active phenomenon. This is obviously because our understanding of the origins of SEP events is not sufficient. From the aspect of practical forecasting of SEPs, the long duration due to continuous acceleration by shock waves and the wide observation range over which particles can be observed even when CMEs occur directly behind the observer, both are often found in gradual SEP events, are crucial factors. Therefore, in order to establish the basis of practical forecast-

ing, especially the arrival of SEPs, this thesis focuses on the relationship between gradual SEP events and CMEs, in particular, on what determines the timescales of SEPs. This section introduces the observational characteristics of gradual SEP events associated with CMEs, including the timescales of SEPs, and describes the aim of this thesis.

1.2.2 Gradual SEP and CME

Among the relationships between gradual SEPs (hereinafter, "SEP" refers to gradual SEP) and CMEs, the most well-known one is the positive correlation between the CME speed and the peak proton flux (Kahler, 2001). As shown in Figure 1.9, the higher the CME speed, the larger the maximum observed proton flux in several energy ranges. However, even if CMEs of the same speed are the source, the peak proton flux varies up to four orders of magnitude. This represents a wide variation of SEP events and also means that our understanding of the generation of SEPs is lacking.

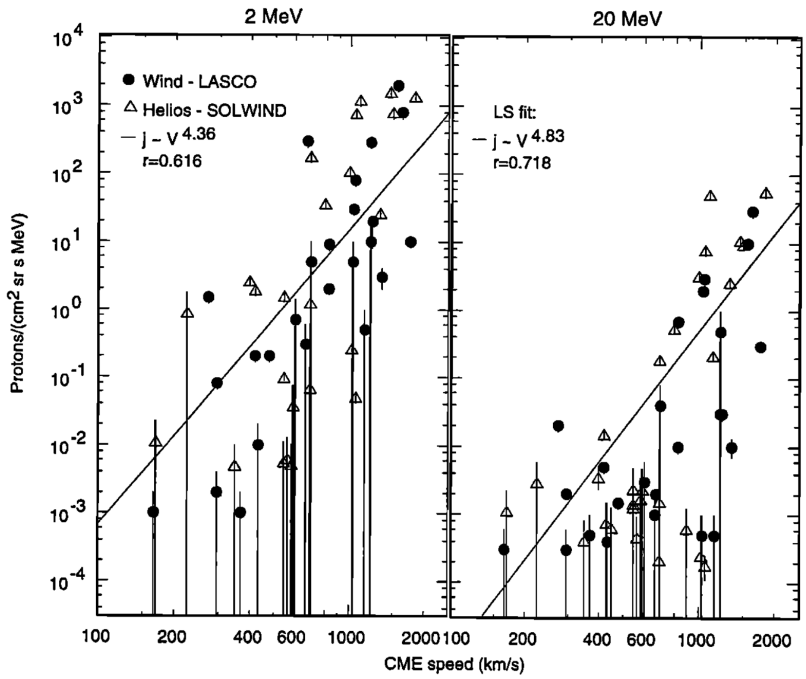

Figure 1.9: Correlation between CME speed and peak proton flux of 2 MeV (left) and of 20 MeV (right) from the two data sets. Cited from Kahler (2001).

How the SEPs are observed in 1 AU depends on where the source CME was launched from. Particles released from the Sun basically travel in interplanetary space along the magnetic field lines extending from the solar surface. The magnetic fields are spiral due to the effect of the rotation of the Sun (Parker Spiral; Parker, 1958) so that the footpoints

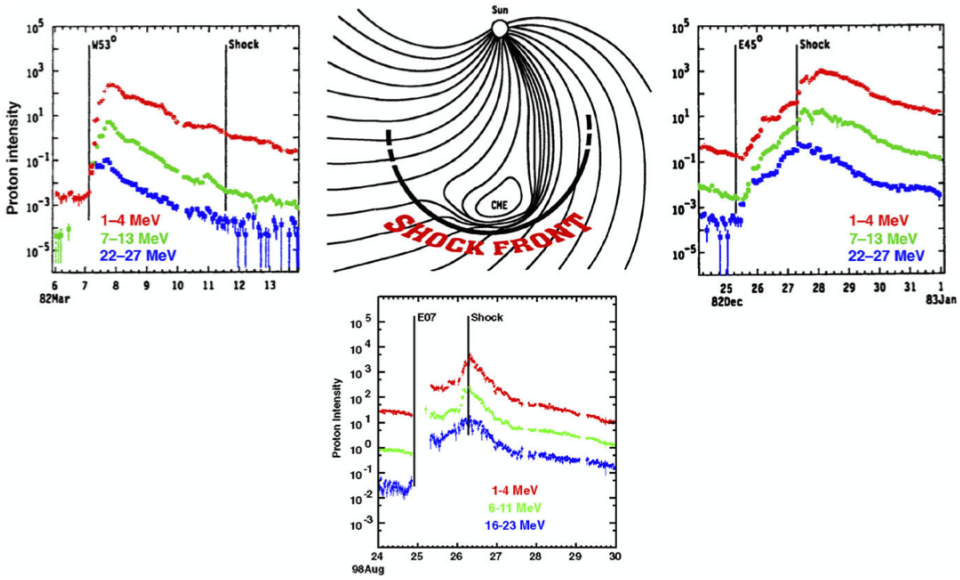

Figure 1.10: Three cases of the behavior of protons when CMEs are observed from different locations. Each panel represents how the time profile varies when the source CME is launched downward and the protons are observed from near where the panel is located. Cited from Desai & Giacalone (2016) but the original concept is shown by Cane et al. (1988) or Reames (1999)

of the lines connected to the observer are not located directly in front of the observer but on the west side of the solar surface. This longitudinal range in which those footpoints are located is called "well-connected longitude", and SEPs are frequently observed when CMEs are launched around these longitudes. In addition, the typical time profile of SEPs is also roughly determined by the released longitude of CMEs.

Figure 1.10 introduces three cases of the behavior of protons when CMEs are observed from different locations (Cane et al., 1988). The first (left panel) is the case where the solar longitude of the observation instrument is located east for the launched direction of the CME. In this case, the source region of the CME is on the west side seen from the instrument and is magnetically well-connected to the "nose" corresponding to the front part of the shock wave driven by CME. The acceleration efficiency is thought to be high in this region (e.g., Gopalswamy et al., 2013), and the particles are observed immediately after the launch of the CME and reach the peak. The proton flux gradually decreases as the shock wave (acceleration region) is separated from the magnetic field lines connected to the instrument. The second (middle panel) is the case where the instrument is located in the launch direction of the CME. When the CME is launched, the shock wave is far from the well-connected magnetic field lines, but they intersect as the shock wave propagates

and spreads, and the proton flux increases. Since the shock wave driven by the CME propagates straight toward the instrument, the flux rises or reaches the peak when the shock wave reaches the instrument, and it decreases after the shock wave passes. The third (right panel) is the case where the instrument observes the CME on the east side of the solar surface, which has the worst connectivity among the three cases. Therefore, the connectivity increases with the temporal spread of the shock wave, and the flux also increases. Finally, the connectivity becomes the best and it reaches the peak after the shock wave passes through the instrument.

1.2.3 Timescale of SEP

While the work by Cane et al. (1988) does well describe the characteristics of SEPs according to the longitudes of CMEs, the timescales of SEPs are still unclear in many cases. When the particles reach the Earth and how long they keep high levels are essential information to prevent radiation hazards. One of the earliest investigations of SEP timescales was by Van Hollebeke et al. (1975), which showed that the time between the onset and maximum of a proton event is a minimum of 2.5 hours when the source event (but a flare, not a CME) is near W50. Kahler (2005, 2013) and Pan et al. (2011) analyzed three timescales related to SEP defined by Kahler (2005) and reported that the timescales of SEPs had large variations between events but sometimes correlated with the CME speed, the CME width, and proton peak flux. In particular, the SEP onset time (the time from the occurrence of a CME to the detection of SEPs in 1 AU, which corresponds to "TO" defined by Kahler (2005)) is the most important information for warning of radiation hazard on the Earth, but it is not yet clear on what timescales SEPs are accelerated and released either theoretically or by observation.

When and at what height in the solar corona or interplanetary space the particles are accelerated and released also affects the timescales of SEPs. Since it is not possible to capture the release of particles by remote observation, various attempts have been made to investigate the acceleration source of particles (more specifically, the release timing and released height) based on numerical simulation (e.g., Rouillard et al., 2016; Kouloumvakos et al., 2019) or observation (e.g., Kahler, 1994; Tylka et al., 2003; Huttunen-Heikinmaa et al., 2005; Reames, 2009a,b; Gopalswamy et al., 2012; Kouloumvakos et al., 2015). Details are described in Section 3.1, but variable results have been obtained depending on the event, and further analysis is required.

1.2.4 Aim of this Thesis

The three main topics addressed in this thesis are as follows:

Q1. How are SEPs associated with CMEs?

Q2. How are the timescales of SEPs related to the parameters of the CMEs?

Q3. What are the factors that determine the timescales of SEPs with large variations between events, especially the SEP onset time (TO)?

Chapter 1 traced the history of the discovery of SEPs and the search for their origins, and introduced the discussion of the relationship between gradual SEPs and CMEs. Chapter 2 is a statistical study of the relationship between CMEs and SEPs, and the timescales of SEPs. This chapter discusses Q1 and Q2 based on the published paper Kihara et al. (2020), which compiles one of the largest SEP event lists. In Chapter 3, we report the results of the detailed event analysis of two examples of SEP events with characteristic timescales extracted from the event list complied in Kihara et al. (2020). The detailed analysis from the observations of the solar surface to the conditions of the upper solar atmosphere is conducted to investigate when and how SEPs are accelerated and transported to the Earth, and it provides implications for Q3. The contents of this chapter are based on the submitted paper Kihara et al. (2022, submitted). Finally, Chapter 4 concludes with a current understanding of SEPs based on these analyses.

CHAPTER 2

Statistical Analysis of the Relation between Coronal Mass Ejections and Solar Energetic Particles

The content of this chapter is based on Kihara et al. (2020). Some content has been changed due to the structure of the thesis.

2.1 Introduction

This thesis deals with gradual SEP events, but as described in Section 1.1.4, the roles of solar flares cannot be ignored. There has been renewed interest in the role of solar flares in producing large gradual SEP events. This is due to the intimate association of gradual SEP events with type III radio bursts (which have been considered "flare" attributes, see Cane et al., 2002) and to the apparent correlations between SEPs and flare parameters (Dierckxsens et al., 2015; Grechnev et al., 2015; Trottet et al., 2015). However, these arguments may not exclude CMEs as the main contributor for gradual SEP events for the following reasons. First, CMEs are also frequently accompanied by type III bursts. Second, the parameters of large flares may vary in proportion to CME parameters as a result of the so-called "big-flare syndrome" (Kahler, 1982). Moreover, there are no SEPs from intense flares if they are not associated with CMEs (e.g., all the X-class flares in AR 12192 in October 2014, see Sun et al., 2015), and some of the most intense SEP events can be associated with flares that are quite modest (Cliver, 2016).

Therefore, we assume that particles in gradual SEP events, at least the large ones, are accelerated by CME-driven shock waves. In this assumption, we may expect a correlation between the SEP peak flux and the CME speed, which is generally the case, although for

a given CME speed, a scatter of up to four orders of magnitude in the SEP peak fluxes was found (Kahler, 2001). This large scatter can be attributed to a number of factors, ranging from the conditions for particle acceleration at the CME-driven shocks to the transport processes undergone by the particles. Earlier events may set up preconditioning in favor of SEP production by providing seed particles and producing enhanced levels of turbulence at the shock (e.g., Li & Zank, 2005). Observationally, a CME preceded by another CME within a short interval tends to be more SEP-productive (Gopalswamy et al., 2004; Kahler & Vourlidas, 2005). Additionally, even though the CME speed is a good measure of the shock speed, the efficiency of particle acceleration depends on various shock parameters that may vary significantly over the shock surface. The SEP flux may be affected by where on the shock the observer is dynamically connected to (e.g., Kouloumvakos et al., 2019, and references therein). These factors, together with the transport effects, that might involve cross-field diffusion (e.g., Zhang et al., 2009), affect not only the measured SEP peak but also the SEP temporal variations. The latter may often be consistent with the patterns expected from the longitude of the source region relative to the observer (Cane et al., 1988), but occasionally SEP events with prompt onsets may be observed even from poorly connected longitudes (e.g., Cliver, 1982; Gómez-Herrero et al., 2015). It is likely that the observed SEP peak fluxes and temporal variations result from a combination of the above-mentioned factors. With this in mind, it is meaningful to study SEP events statistically in relation to the CME speed and the longitude of the source region.

In this chapter, we present a statistical study of SEP occurrences and timescales with respect to CME source locations and speeds. Here we start from fast and wide CMEs and relate them to SEP properties. Most previous studies have started from SEP events and have then studied the properties of the associated CMEs and flares, ignoring CMEs not associated with SEP events. The recent study of 11 CMEs which did not produce SEP events by Lario et al. (2020) may be an exception. Our work focuses on the presence/absence and timescales of SEP events in association with individual CMEs, as presented in Sections 2.3 and 2.4, respectively. These are preceded by a description of our event list (Section 2.2) and followed by a discussion of how to explain our findings (Section 2.5). We summarize our findings in Section 2.6.

2.2 Event List

Our ultimate goal is to understand how the properties of CMEs may affect the properties of SEP events, such as their occurrence, peak fluxes and timescales. To acknowledge the fact that some energetic CMEs, even from well-connected longitudes, produce no SEPs or that CMEs from poorly-connected regions produce SEP events that quickly rise to a peak, it is meaningful to study all those CMEs irrespective of their associated SEPs and then to

investigate the reasons for the wide variety of SEP properties. This approach complements one that discusses the properties of only those CMEs that are associated with SEP events (e.g., Kahler, 2001).

Our study is based on fast ($v_{CME} \geq 900$ km s^{-1}) and wide (angular width $\geq 60°$) CMEs. In the first approximation, these CMEs may be considered to drive the shocks that are responsible for accelerating the protons observed at 1 AU, although the occurrence of a shock wave depends not only on the CME speed, but also on the conditions of the ambient solar wind. We imposed the restriction on angular width in order to exclude narrow CMEs, which are typically associated with small impulsive SEP events (Kahler et al., 2001). We selected them from the CDAW SOHO LASCO CME catalog* (Yashiro et al., 2004), which is a complete manually-generated catalog of CMEs as observed by the Large Angle and Spectrometric Coronagraph Experiment (LASCO: Brueckner et al., 1995) on board the Solar and Heliospheric Observatory (SOHO). Measurements of the kinematic parameters of CMEs included in the catalog come from visual inspection of all the available difference images.

Another important factor that can affect the properties of SEP events is the magnetic field connection between the observer and the CME-driven shock wave, which may be assumed to expand concentrically from the source region of the CME. If the region is on the visible side of the Sun, we can locate it using known low coronal signatures of CMEs, such as coronal dimming and post-eruption arcades (e.g., Zhang et al., 2007; Hudson & Cliver, 2001; Nitta et al., 2014). These signatures are found in coronal images at extreme-ultraviolet (EUV) wavelengths. In order to maximize the number of CMEs for which source regions can be identified, including those from the far side, we have studied those CMEs that occurred since December 2006, so that we can make use of information from the EUV imagers on board the Solar-Terrestrial Relations Observatory (STEREO), in addition to those near the Sun-Earth line from SOHO (until 2010) and the Solar Dynamics Observatory (SDO: Pesnell et al., 2012, from 2010). All the fast and wide CMEs in solar cycle 24 were included in the period of our investigation (i.e., from December 2006 to October 2017). After examining the EUV images taken around the times of the 257 CMEs that meet our criteria for speed and angular width, we removed 18 CMEs for which source regions could not be identified. Almost all of them occurred while no STEREO data were available around the great conjunction in 2015.

Instead of discussing common SEP events observed by multiple spacecraft at separate longitudes (e.g., Richardson et al., 2014) or CMEs without SEPs at any of these spacecraft (Lario et al., 2020), we studied the SEP events (or lack thereof) at Earth, STEREO-A, and STEREO-B that are associated with each of the 239 CMEs. We thus have a total of 717 potential measurements. We extracted the time profiles of >10 MeV proton fluxes by

*https://cdaw.gsfc.nasa.gov/CME_list/

using data with five-minute temporal resolution from the Energetic Particle Sensor (EPS: Onsager et al., 1996) on the Geostationary Operations Environmental Satellite (GOES) and from the High-Energy Telescope (HET: von Rosenvinge et al., 2008) and the Low-Energy Telescope (LET: Mewaldt et al., 2008), which belong to the suite of instruments for the In Situ Measurements of Particles and CME Transients (IMPACT: Luhmann et al., 2008) on STEREO. The >10 MeV integral flux is one of the standard products of GOES, but for STEREO / IMPACT we had to compute it by combining the HET and LET data, as illustrated by Gopalswamy et al. (2016).

Now we show how the >10 MeV proton flux compares between GOES and STEREO. Rodriguez et al. (2017) performed a cross-calibration between GOES and STEREO using two SEP events that occurred in 2006 December while STEREO-A and STEREO-B were still located near Earth. They reported that the STEREO 10 – 100 MeV flux were smaller than GOES: the first, the second, and the third quartile of STEREO-A (STEREO-B) to GOES ratios are 0.850 (0.874), 0.926 (0.948), and 1.017 (1.071), respectively. We carried out the same analysis for the >10 MeV integral flux and confirmed that the first, the second, and the third quartile are 0.841, 0.921, and 1.008 for STEREO-A, and 0.858, 0.935, and 1.042 for STEREO-B. The 5th and 95th percentiles of the ratios are 0.736 and 1.215 for STEREO-A, and 0.767 and 1.272 for STEREO-B. Therefore 90% of >10 MeV integral fluxes agree within 27%.

In Table 2.1, we list the selected CMEs. The first three columns show the onset date and time, the projected speed, and the angular width of the CME, taken from the CDAW SOHO LASCO CME catalog. Note that the CME onset time is calculated by extrapolating the height-time profile in the LASCO field of view to the solar surface (1 solar radius from the Sun center). The next two columns show the magnitude and location of the associated solar flare. The remaining columns show the quality and the peak proton flux, if it exceeded 1 particle flux unit (pfu: defined as particles s^{-1} sr^{-1} cm^{-2}), separately for GOES, STEREO-A, and STEREO-B. The "quality" is one of the following.

- Good (110 events): SEPs are detected unambiguously with the peak >10 MeV proton flux exceeding 1 pfu. It is >10 pfu in 69 events and ≤10 pfu in 41 events. They are sufficiently well-observed that we can compute all the timescales (see Section 2.4).
- Contaminated (26 events): The observed SEP onset is clearly associated with the CME, but the later, post-peak temporal variations are contaminated by another SEP event due to a later CME or an energetic storm particle (ESP) event due to the shock wave driven by the present or an earlier CME*. In 15 events, the peak >10 MeV

*There are a few confusing cases, where an ESP-related shock arrived during the SEP event in question. We identified a non-ESP peak before the shock arrival as the SEP peak.

proton flux exceeds 10 pfu. We were able to measure all the timescales but the duration (see Section 2.4).

- No SEP (395 events): No >10 MeV protons are detected exceeding the 1 pfu level during the normal background. The normal background is about 0.2 pfu for GOES and about 0.1 pfu for STEREO-A and STEREO-B. In 71 of them, we noted a smaller enhancement (≤1 pfu), and they are so indicated.

- HiB_N (85 events): The background was elevated from the normal due to earlier events, preventing a small SEP event from being detected. Despite the higher background, however, we clearly find the presence of a SEP event in 18 cases, of which 16 have the peak >10 MeV proton flux that exceeds 10 pfu. An approximate background level (in pfu) is indicated by N. Subsets of these events, depending on N, are excluded in the discussion of the SEP association rate of CMEs (see Section 2.3).

- No data (79 events): No SEP data are available around the time of the CME. This includes the periods of no STEREO data due to the great conjunction in 2015, no STEREO-B data since its contact was lost in October 2014, and occasional data gaps for various reasons. These events are excluded in the following analysis.

- Multiple (22 events): No link can be established between the CME in question and the SEP event because of multiple CMEs and ESP events that occurred in succession. These events are excluded in the following analysis.

We note that the required threshold $v_{CME} \geq 900$ km s^{-1} excluded some large SEP events. Four >10 MeV proton events with peak fluxes exceeding 10 pfu are not included in this study. The starting dates of these events are 2012 July 12, 2013 April 11, 2014 November 1, and 2015 October 29. The speeds of their associated CMEs were 885 km s^{-1}, 861 km s^{-1}, 740 km s^{-1}, and 530 km s^{-1}, respectively. We also point out that our selected events are different from those in previous statistical studies of SEP events that were not restricted in CME parameters. For example, the fraction of CMEs with $v \geq 900$ km s^{-1} was only 147/217 and 85/214, respectively, in the works by Kahler (2013) and by Richardson et al. (2014). Accordingly, these authors included SEP events as observed by Wind, SOHO and STEREO that were too weak to be observed by GOES; since the GOES background is higher than those of the other three missions.

2.3 SEP Association of Fast and Wide CMEs

This work involves careful analyses of EUV images to locate the region from which each of the selected CMEs originated, using known low coronal signatures of CMEs (e.g., Zhang

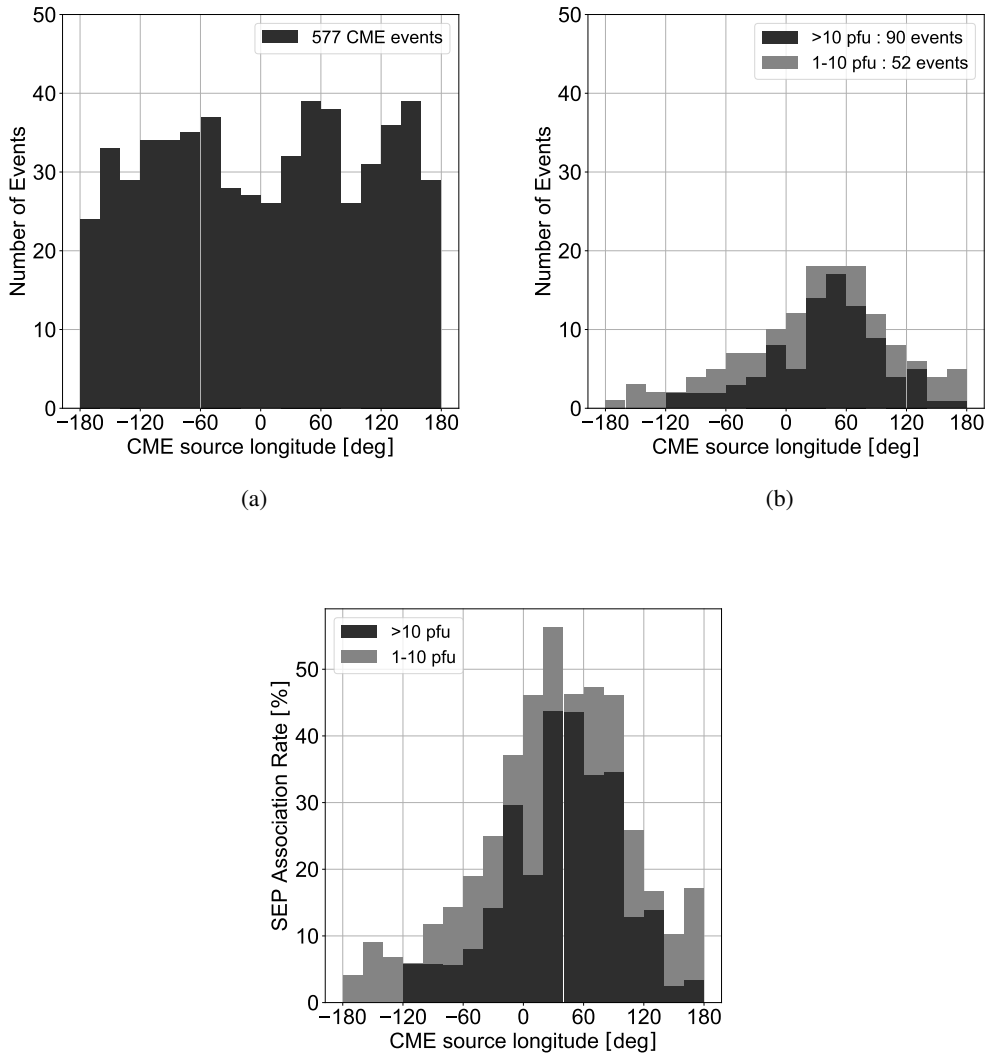

Figure 2.1: Distribution of CMEs with source longitude (in 20° bins) relative to the observer. (a) All the CMEs, irrespective of their associations with SEP events. CMEs that occurred during high background periods are excluded (39 HiB_N events, with $N \geq 10$, see Section 2.2). (b) Only the CMEs associated with a SEP event exceeding 10 pfu (black) and between 1 and 10 pfu (gray). (c) The percentage of CMEs associated with a SEP event (the color usage same as (b)). Panels (b) and (c) exclude 10 and 2 HiB_N events (with $N \geq 10$ and $N \geq 1$) for >10 pfu and 1 – 10 pfu, respectively.

et al., 2007; Hudson & Cliver, 2001; Nitta et al., 2014). Figure 2.1 shows the distribution of our CMEs with the longitude of the source region relative to the observer. Note that the same CME can appear up to three times at different longitudes, as seen from Earth, STEREO-A, and STEREO-B. In Figure 2.1(a), we include all the CMEs, irrespective of their associations with SEP events, except for 39 "HiB_N" ($N \geq 10$) events (Section 2.2). In these high background events, the association with a SEP event exceeding 10 pfu is uncertain, since it is possible that such an event could be buried under the background. Thanks to multi-spacecraft observations, we have at least 23 CMEs in each of the 20° bins. Figure 2.1(b) shows the distribution of SEP-associated CMEs, and Figure 2.1(c) the ratio of SEP-associated CMEs to all CMEs. In Figures 2.1(b) and 2.1(c), we show the association of CMEs with SEP events as defined by two thresholds for the peak flux: 10 pfu and 1 pfu. Figure 2.1(c) shows that the SEP association rate is elevated in the range of longitude of E20 – W100. We therefore refer to this range of longitude as "well-connected" in this section (i.e., Figures 2.2 and 2.4(a)). This is broader than what was shown in previous studies on the longitudinal distributions of SEP events (e.g., Smart & Shea, 1996; Laurenza et al., 2009). It is possible that the broader distributions in Figure 2.1(c) may be characteristic of our SEP events measured at >10 MeV, most of which come from solar cycle 24.

In Figure 2.2, we show the distribution of CMEs with speed in 200 km s^{-1} bins. Here we limit the CMEs to those from the well-connected longitudes (E20 – W100). As expected, there are more CMEs that are slower (but $\geq$ 900 km s^{-1}), although the SEP association rate rises sharply with the CME speed. All the CMEs faster than 2100 km s^{-1} are associated with a SEP event.

The dependence of the SEP association rate of CMEs on both the longitude of the source region and the CME speed can be visualized in heat maps, as shown in Figure 2.3. Here the maps come from a 2D array of the longitude relative to the observer (in 45° bins) and the speed (in 600 km s^{-1} bins) of the CME. Colors from yellow to red represent low to high association rates, as indicated in the color bars in the figure. Note that the SEP association rates have large uncertainties except for the bottom row because of the limited number of events. Figures 2.3(a) and 2.3(b) are heat maps for the SEP association rate for SEP events with threshold peak fluxes >10 pfu and >100 pfu, respectively. The number of all the CMEs and of the SEP-associated CMEs, together with the association rate, is also indicated in each cell. As in the previous figures, we exclude the HiB_N events that prevent us from determining the association of the CME with a SEP event. For the association with SEP events exceeding 10 pfu (panel (a)), 39 events with $N \geq 10$ are excluded. For SEP event exceeding 100 pfu (panel (b)), 9 events with $N \geq 100$ are excluded. As a result, the number of all the CMEs is greater in panel (b). Note that there was only one CME faster than 2700 km s^{-1}, which occurred on 2017 September

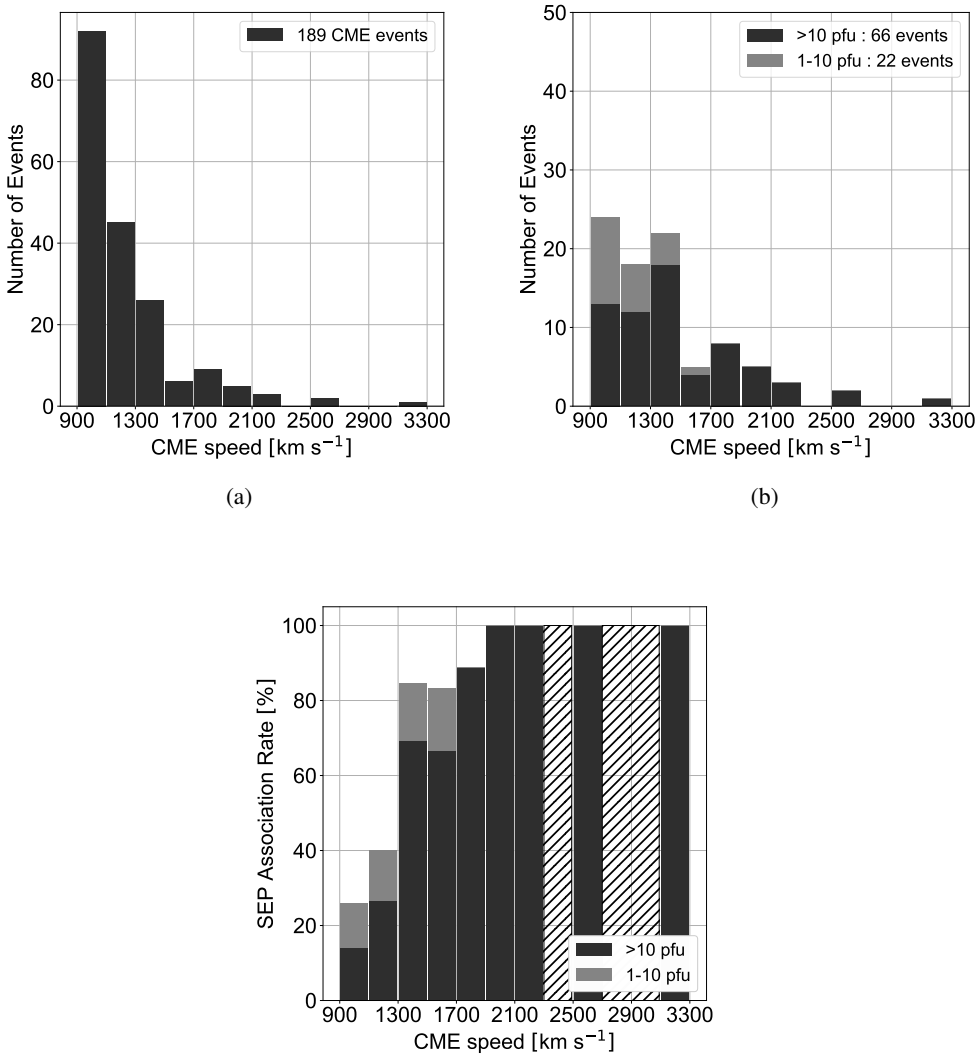

Figure 2.2: Distribution of CMEs with speed in 200 km s^{-1} bins. Here we limit the CMEs to those from the source longitudes E20 – W100. (a) All the CMEs, irrespective of their associations with SEP events. (b) Only CMEs associated with a SEP event exceeding 10 pfu (black) and between 1 and 10 pfu (gray). (c) The percentage of CMEs associated with a SEP event (the color usage is the same as in (b)). Note that there were no CMEs between 2300 km s^{-1} and 2500 km s^{-1} and between 2700 km s^{-1} and 3100 km s^{-1}, as indicated by the hatched areas in panel (c). As in Figure 2.1, HiB_N events are excluded ($N \geq$10 in (a), $N \geq$10 and $N \geq$1 in (b) and (c), for >10 pfu and 1 – 10 pfu, respectively.

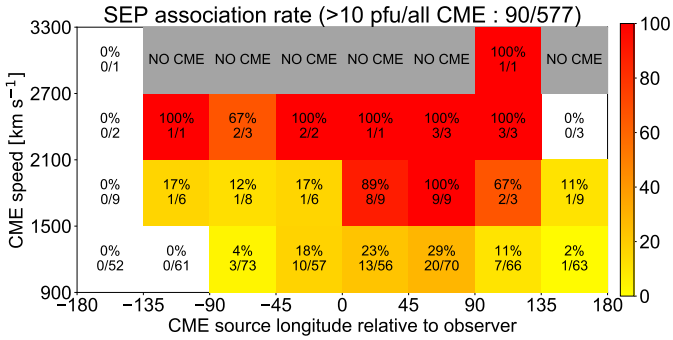

(a)

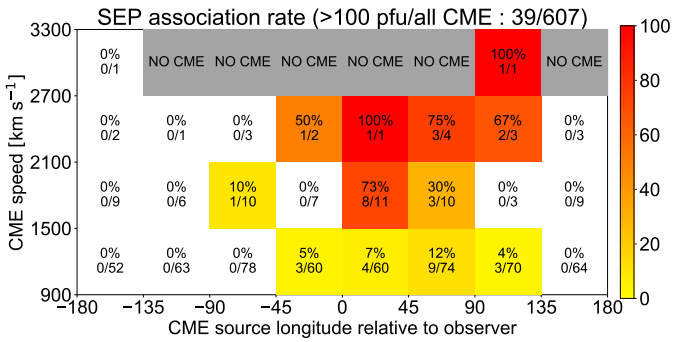

(b)

Figure 2.3: SEP heat maps, showing how the SEP association rate varies with the source longitude and speed of the CMEs. (a) and (b) show, respectively, a heat map for SEP events >10 pfu and >100 pfu. Higher (lower) association rates are shown in red (yellow). Cells in gray indicate no CMEs in those ranges of speed and source longitude. Cells in white indicate no SEP association. Different numbers of the HiB_N events are excluded in (a) and (b), depending on N; $N \geq 10$ and $N \geq 100$ for (a) and (b), respectively (see text).

10. Its speed was 3163 km s^{-1}. This CME appears twice in each heat map, since it occurred after the contact with STEREO-B was lost. Its source location was S09W90 from Earth. This translates to E142 from STEREO-A, at which only a weak SEP event was observed that seemed to be directly linked to the CME. The >10 MeV proton flux peaked on September 12*, and the peak flux was less than 10 pfu. Therefore the top left cell indicates no SEPs in Figures 2.3(a) and 2.3(b). There were fewer CMEs with higher speeds, and based on limited statistics, it appears that faster CMEs are associated with SEPs over wider longitudes. For the association rates of CMEs with SEP events for which the peak exceeded 10 pfu, we can confirm that faster CMEs contribute more to the SEP association rate. For example, Figure 2.1(c) shows that the SEP association rate of CMEs around W60 is ∼40%, which results from the 100% association rate for CMEs faster than 1500 km s^{-1} offsetting the lower association rate for slower CMEs. Figure 2.3(b) shows that the CMEs associated with >100 pfu SEP events not only are much rarer but also are limited to higher speeds and narrower ranges of longitude.

In space weather applications, the SEP peak flux is routinely forecast using basic properties of CMEs and flares. In Figure 2.4, we show the relations among the SEP peak flux, the CME speed, and the magnitude of the associated flare. Figure 2.4(a) shows the relation between the peak proton flux and the CME speed. Even though they appear to be weakly correlated, especially for those events in the well-connected longitudes (plotted in blue), there is considerable scatter, as found in past studies (e.g., Kahler, 2001); the peak proton flux for the same CME speed can vary by three orders of magnitude, even though we limit the CMEs to fast ones ($v_{CME} \geq 900$ km s^{-1}) in this study. This is unlike Kahler (2001), who included even CMEs slower than 200 km s^{-1}. The regression lines of each group of longitudes are also shown in Figure 2.4(a). The peak proton flux tends to be higher for the SEP events from well-connected longitudes. The difference is about one order of magnitude for a CME with 2000 km s^{-1}.

In Figure 2.4(b), we plot the peak soft X-ray (SXR) flux of the associated flare vs the CME speed, considering separately those CMEs associated with, and not associated with, >10 pfu protons. There is a somewhat higher correlation for SEP-associated CMEs, which tend to be faster (Figure 2.2(a)). This relation may largely reflect the big-flare syndrome (Kahler, 1982). Figure 2.4(c) shows a weak correlation between the peak SXR flux and peak proton flux, irrespective of whether the source region is in the western or eastern hemisphere. Note that this plot contains only flares that were associated with fast and wide CMEs. The scatter would be much more pronounced if all flares were included irrespective of their associations with CMEs.

*A higher (>100 pfu) >10 MeV proton flux was seen on September 14, but this appears to have been due to a stream interaction region rather than to the CME on September 10 (see Guo et al., 2018).

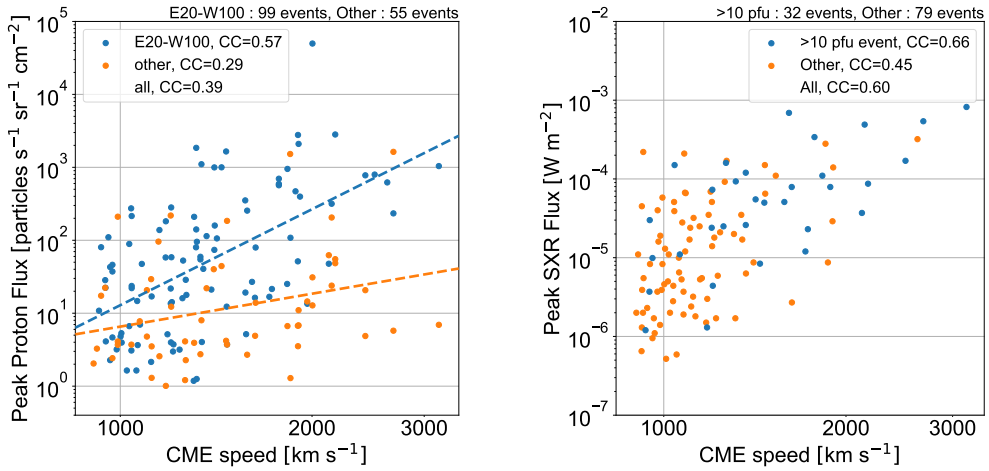

(a) (b)

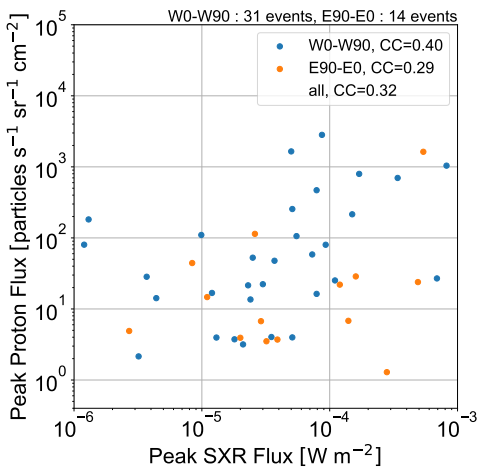

(c)

Figure 2.4: Correlations between the parameters of flare, CME, and SEPs. (a) Correlation between CME speed and peak proton flux. Each symbol shows whether or not the events come from well-connected longitudes. The dashed lines are the regression lines for each group. All the events in which the peak proton flux was measured are included ("Good", "Contaminated", and "HiB_N"). (b) Soft X-ray (SXR) flux vs CME speed as observed by GOES. This figure contains only the data from frontside events at longitudes E90-W90 from GOES. The symbols show whether or not each CME is associated with a >10 pfu SEP event. (c) Peak proton flux vs soft X-ray flux (both from GOES) for frontside events.

2.4 SEP Timescales

The timescales are also important properties of SEP events. Typical questions include: When does the SEP event start? How fast does it rise to the peak? And how long does it stay at a high level? We measured the key times of SEP events only when the onset was clearly found. They are labeled either "Good" or "Contaminated" in Table 2.1, not including events that have high pre-event background. If the quality in Table 2.1 is "Good"—we measured the following four times in this study: the SEP start time, the SEP half-peak (start), the SEP peak time, and the SEP half-peak (end). We measured all times on a log scale plot. We defined the SEP start time manually as the time when the proton flux increased above the background, typically in three consecutive 5 min intervals. The SEP peak time is usually the time after the SEP start time when the proton flux is the highest. More complex cases are described below. The SEP half-peak (start) and SEP half-peak (end), respectively, were automatically extracted as the times when the proton flux first exceeded—and last went below—half of the flux at the SEP peak time.

Many SEP events show simple rise-and-fall time profiles, and we were able to measure the four times defined above unambiguously for these events. However, in some events the proton flux time profile exhibited a second or even third peak, following a plateau or plateaus after the first peak. In such events, we usually took the time of the first peak as the SEP peak time. This is because later peaks may be produced by transport effects and thus may not directly reflect the CME properties. Other SEP events show a clear onset, but subsequent time profiles are contaminated either by another SEP event due to a later CME or by an ESP event locally produced by the passage of the shock wave driven by the present or an earlier CME. They are labeled "Contaminated" in Table 2.1. We did not measure the SEP half-peak (end) for any of these 26 events, but in all of them the SEP peak was clearly seen, allowing us to measure the SEP start time, SEP half-peak (start) and SEP peak time.

From these times, we calculated the four timescales listed in Table 2.2. They are illustrated in Figure 2.5 using an example of a real SEP event. Here, TO is the onset time, which measures how quickly the SEP event starts at 1 AU (defined as the SEP start time) after the CME launch at 1 $R_\odot$; TR is the rise time from the SEP start time to the SEP half-peak (start); Tm is the full rise time from the SEP start time to the SEP peak time; and TD is the duration, i.e., the length of time during which the proton flux stays above half the peak value, which is between SEP half-peak (start) and SEP half-peak (end). These notations—TO, TR, and TD—were adopted by Kahler (2013). He also used OR, which is the sum of TO and TR; that is, the time from the CME launch at 1 $R_\odot$ to SEP half peak (start). The timescale Tm is a redefinition of ΔT_m that was first used by Van Hollebeke et al. (1975).

Here we study the correlation of the SEP timescales TO, TR and TD with CME source

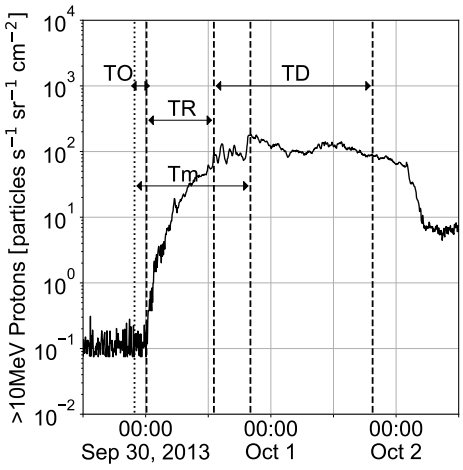

Figure 2.5: An example showing the four timescales defined in the text. The dashed lines, from left to right, are the SEP start time, the SEP half-peak time (start), the SEP peak time, and the SEP half-peak time (end). The dotted line is the CME launch time from SOHO LASCO CME catalog.

longitude and speed. The plots in Figure 2.6 show the correlation of TO and TR with the CME source longitude relative to the footpoint of the Parker spiral ($\Delta\Phi$). We calculated the longitude on the solar surface of the nominal footpoint of the Parker spiral that was connected to GOES, STEREO-A, and STEREO-B, using the solar wind speed around the time of the SEP onset, as sampled by Wind and STEREO. When the Wind data were missing, we used data from the Advanced Compositional Explorer (ACE). Some events had to be dropped because we were not able to calculate the longitude of the Parker spiral footpoint due to the unavailability of solar wind data. These timescales are plotted vs $\Delta\Phi$ in Figures 2.6(a – c), where larger and darker circles indicate faster CMEs. Figure 2.6(a) shows that CMEs from regions within 60° in longitude from the footpoint of the Parker spiral tend to be associated with SEPs with short onset times. In this region of $\Delta\Phi$, TO is almost always shorter than five hours but longer than one hour. Note that it takes 1.15 hours for 10 MeV protons to travel the distance of 1.2 AU, which is often used as a typical path length for the Parker spiral corresponding to a solar wind speed of $\sim$400 km s^{-1}. The longest TO is about 18 hours for an event that is far outside this range of $\Delta\Phi$. In Figure 2.6(b), we find a similar trend for TR with $\Delta\Phi$, but with more scatter, even for $|\Delta\Phi| < 60°$. In Figure 2.6(c), TD is characterized by a broad distribution for most ranges of $\Delta\Phi$, with occasional high values.

Next we consider how TO, TR, and TD depend on the CME speed (v_{CME}), as plotted in Figures 2.7, 2.8, and 2.9, respectively. Panel (a) in each of these figures plots individual

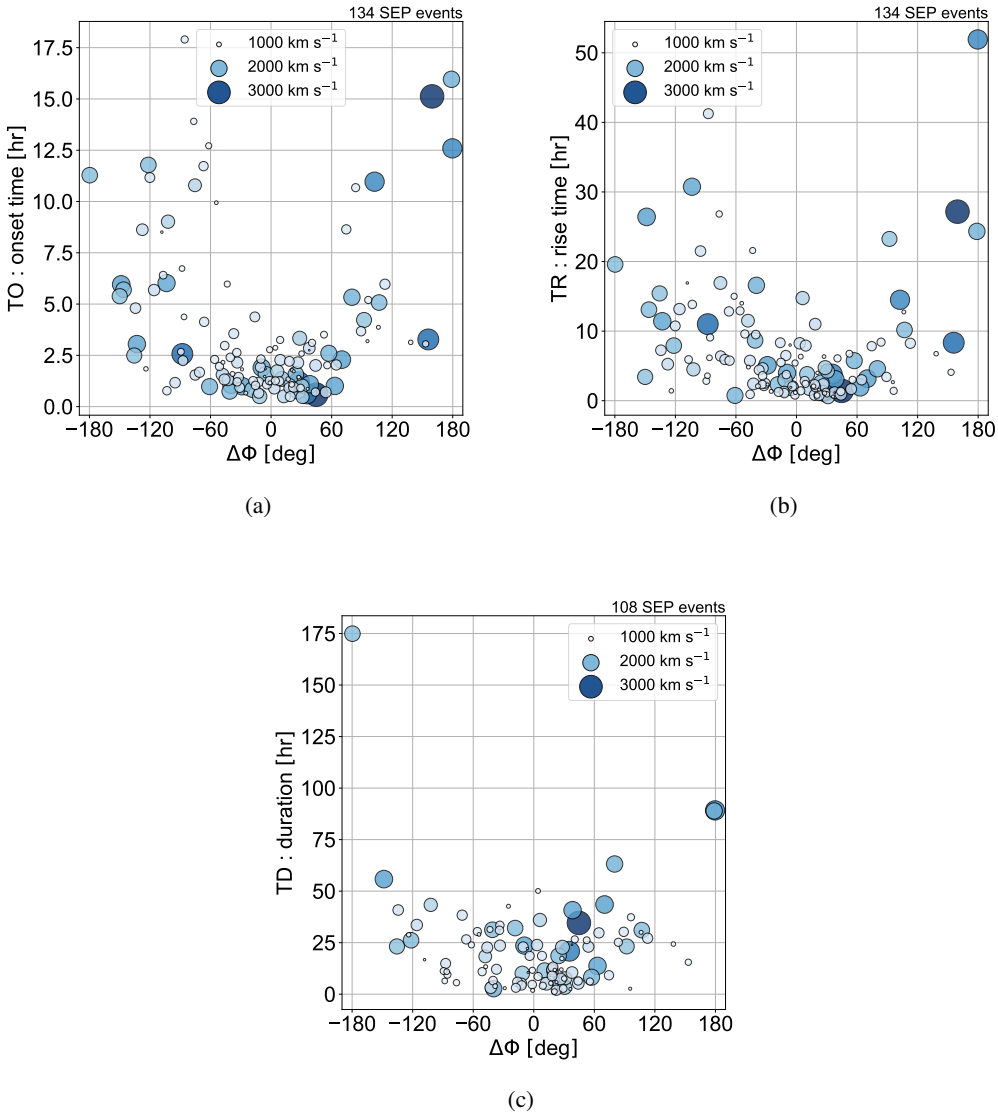

Figure 2.6: (a) SEP onset time from the CME launch (TO) vs the longitude of the CME source region relative to the footpoint of the Parker spiral. (b) and (c) The same plot, but for the SEP rise time TR and SEP duration TD. The size and darkness of the circles correspond to the CME speed. Almost all the SEP events listed in Table 2.2 are included in panel (a) and (b), except for the one on 2006 December 13 observed at STEREO-A and STEREO-B. This is because both STEREO were located near Earth and their data points are consistent with that of GOES. Events in the Contaminated category are excluded in panel (c) because TD cannot be measured.

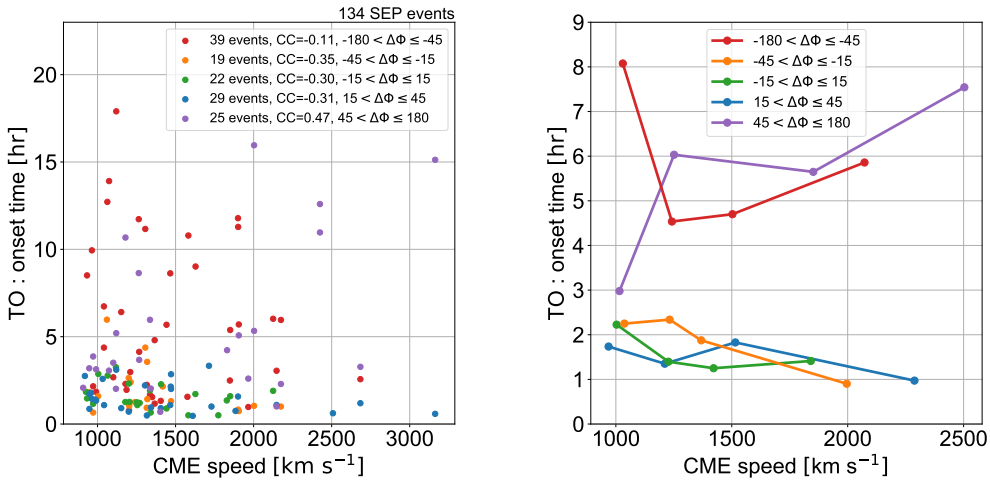

(a) (b)

Figure 2.7: SEP onset time TO vs CME speed (v_{CME}). Different colors are used for events in different ranges of longitude relative to the footpoint of the Parker spiral. Individual TO values are plotted in the left panel. In the right panel, averaged TO values are plotted after re-grouping all the data into four representative CME speeds. The number of data points is the same as in Figure 2.6(a).

data, color coded to distinguish five ranges of the relative longitude as indicated in the legends. We produced panel (b) by grouping all the events into five longitudinal ranges, sorting each group into four subgroups by v_{CME}, and finally taking the average in each of the four v_{CME} subgroups. This analysis follows the work by Kahler (2013), and it is intended to make statistical trends easier to discern. We adjusted the ranges of v_{CME} in the four subgroups in each longitude range so that each subgroup contains roughly the same number of events. In Figure 2.9, we note a reduced number of events that belong to each of the five longitudinal groups. This is because for a number of events the SEP half-peak (end) could not be measured, and therefore TD could not be calculated. According to Figures 2.7 – 2.9, the correlations of the timescales with v_{CME} are not strong. The apparent correlations are susceptible to grouping of the events in different longitude ranges, and taking medians instead of averages does not make the correlations any more solid. Nevertheless, we do see positive correlations for TR and TD with v_{CME}, especially for poorly connected (large $|\Delta\Phi|$) events. Furthermore, TO appears to be negatively correlated for small $|\Delta\Phi|$ events. These trends are consistent with previous results (e.g., Pan et al., 2011; Kahler, 2013). Finally, the relationship between TO and peak proton flux is shown in Figure 2.10. TO is the only timescale that shows a correlation with the peak proton flux. The correlation is rather strong especially near the footpoint of the Parker spiral. This trend was reported by Kahler (2013).

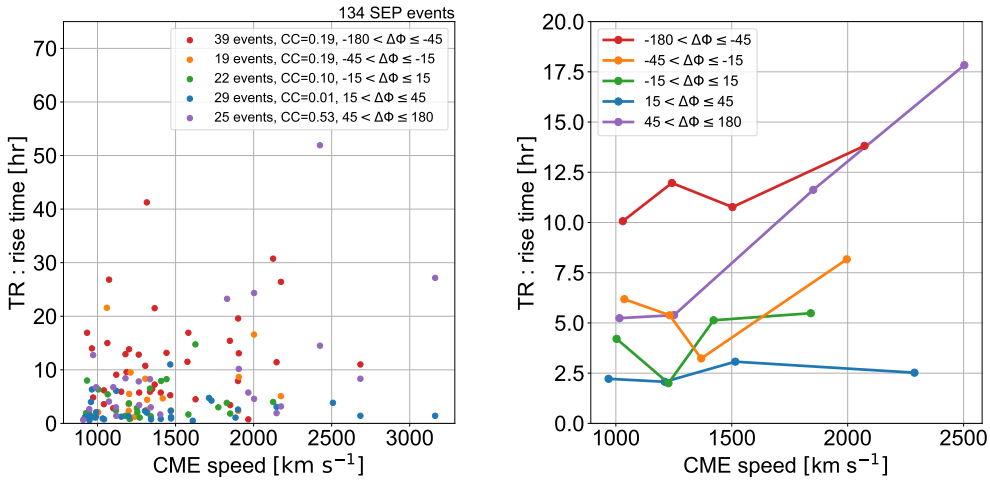

(a) (b)

Figure 2.8: SEP rise time TR vs CME speed (v_{CME}). Same as Figure 2.7, but for the rise time TR. The number of data points is the same as in Figure 2.6(b).

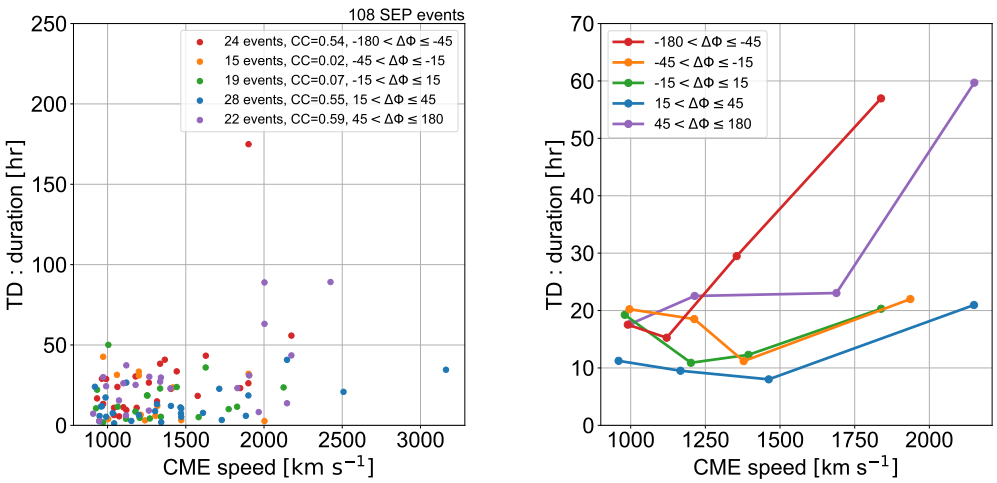

(a) (b)

Figure 2.9: SEP duration TD vs CME speed (v_{CME}). Same as Figure 2.7, but for the duration TD. The number of data points is the same as in Figure 2.6(c).

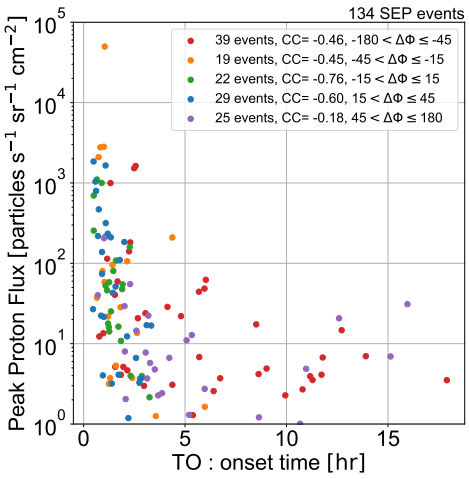

Figure 2.10: SEP onset time TO vs peak proton flux. The color and used data are same as Figure 2.7(a). The correlation coefficients are calculated between TO and logarithm of peak proton flux.

2.5 Discussion

In order to clarify further the roles of CME-driven shocks in generating SEP events, we have carried out a statistical study of the SEP occurrences, peak fluxes, and timescales with respect to the CME source locations and speeds. As noted in Section 2.1, there are several other factors that could affect the SEP properties, such as preconditioning by earlier events (e.g., Li & Zank, 2005, and references therein), spatial distributions of shock parameters closely related to particle acceleration and their time-dependent connections to the observer (e.g., Kouloumvakos et al., 2019, and references therein), transport effects (e.g., Zhang et al., 2009, and references therein), etc. How these factors as a whole affect the SEP properties can ideally be studied in individual events with a comprehensive approach that involves both data analyses and numerical simulations. On the other hand, it is also important to know the trend of how the SEP properties vary with respect to the CME source locations and speeds, as found in a large sample of events. Our approach of starting from CMEs, rather than from SEP events, complements other works that discuss the properties only of CMEs that are associated with SEP events. Recently, Lario et al. (2020) found 11 fast and wide CMEs that did not produce SEP events at any of the three locations, Earth, STEREO-A, or STEREO-B. They discussed these events in terms of a deficit in the release of particles at the time of the eruption and the limited extent of the strongest regions of the shocks driven by the CMEs. In this paper, we presented the statistical trends found in a large number of events observed at GOES, STEREO-A and STEREO-B. Moreover,

we analyzed mostly solar cycle 24 events, whereas similar statistical studies dealt with solar cycle 23 events (e.g., Kahler, 2005, 2013; Pan et al., 2011) or partially included solar cycle 24 events (e.g., Papaioannou et al., 2016). Another difference from previous studies of SEP timescales is that we used the CME source longitude relative to the footpoint of the Parker spiral ($\Delta\Phi$) rather than to the observer. We noted that $\Delta\Phi$ has been used previously for discussing SEP intensities in multi-spacecraft observations (e.g., Richardson et al., 2014).

We found the source regions of 239 fast ($v_{CME} \geq 900$ km s^{-1}) and wide (angular width $\geq 60°$) CMEs. Thanks to STEREO data, we were able to determine the CME source regions accurately, even on the far side of the Sun from the Earth, which was not possible for the solar cycle 23 events. We looked for SEPs at each location, and we calculated the SEP association rate with respect to the CME source longitude relative to the observer (Figures 2.1(c) and 2.3). We discussed only >10 MeV protons here, partly because they define the space weather effects characterized by NOAA. We found higher SEP association rates for CMEs that originate in what we usually consider to be well-connected longitudes. This suggests that the acceleration of >10 MeV protons is more efficient at the nose of a CME-driven shock than elsewhere, which also has been suggested to be the case for higher-energy protons (Gopalswamy et al., 2013). On the other hand, the SEP association rate is non-zero over a wide range of longitudes, consistent with multi-spacecraft observations of SEP events (e.g., Richardson et al., 2014). For CMEs faster than 900 km s^{-1}, only the narrower range of longitudes E180-E135 may be SEP-free. In this work, we did not extensively study the effect of the CME width on SEP events except that we limited to CMEs that were wider than 60°. We, however, note that full halo CMEs that have angular width of 360° more often accompany an SEP event than other CMEs (93/136 vs 33/103), supporting the recent study by Lario et al. (2020) that CMEs without SEPs tend to be narrow.

At the other extreme, a CME from well-connected longitudes must be faster than 1900 km s^{-1} to be always associated with a SEP event (Figure 2.2(c)), suggesting the importance of shock waves, even when the CME originates in this longitude range. Moreover, the peak proton flux from the regression line of well-connected events are one order of magnitude higher than that of poorly connected events with 2000 km s^{-1}, while the peak proton flux of well-connected events vary by three orders of magnitude (see Figure 4(a)). It implies that some important factors (e.g., preconditioning by earlier events) other than CME speed and source longitudes exist. Another factor that may account for the scatter of the peak SEP flux is the spatial extension of the CME-driven shock wave, which can vary for CMEs with similar speeds. This has recently been diagnosed using the bandwidth of hectometric type II bursts (Iwai et al., 2020).

By analyzing the timescales of SEP events, we found that TO (the SEP onset time relative

to the CME launch) is correlated more tightly with $\Delta\Phi$ (the source longitude relative to the footpoint of the Parker spiral) than is TR (the SEP rise time) for $|\Delta\Phi| < 60°$ (Figure 6). The SEP onset is defined by the first-arriving particles. This finding seems to support the idea that only the first-arriving particles may be scatter-free. Particles that arrive later, even well before the peak, may undergo scattering, possibly by irregularities in the magnetic field, turbulence, etc., in the corona and interplanetary space. Past studies either showed no correlation (Kahler, 2005; Pan et al., 2011) or a weak inverse correlation (Kahler, 2013) between TO and v_{CME}. We followed Kahler (2013) in analyzing the grouping of v_{CME} into four subgroups and calculating median values—here we showed averages instead of medians. Our analysis also found weak inverse correlations between TO and v_{CME}, as shown by Kahler (2013) for the well-connected longitudes. Once protons are accelerated to >10 MeV, the strength of the shock, as approximated by the CME speed, may not affect the scatter-free transport of the first-arriving particles. As in previous works (Pan et al., 2011; Kahler, 2013), we found a positive correlation of TR and TD with v_{CME} (Figures 2.8(b) and 2.9(b)). The positive correlation of TR and TD with v_{CME} may be explained if faster CMEs somehow produce wider areas over the shock surface that are favorable for particle acceleration. As a result. the observer would be connected to the regions that accelerate particles for longer time even though the magnetic field connection may change. We did not use Tm for our analysis because, as discussed by Pan et al. (2011), the full peak times do not necessarily represent typical peak times for each event, since proton time profiles often show multiple peaks. Moreover, though we did not show the graph, the tendency of Tm was similar to that of TR, so there is no problem in assuming that TR represents a typical peak time.

Concerning the question of how the timescales are related to the SEP flux, we found an inverse correlation between the peak proton flux and TO (but not TR or TD), similar to Kahler (2013), who pointed out that coarse time bin (half-hour) compromise the timing analysis and instead introduced a background effect to explain the apparent inverse correlation. We measured timescales in five-minute data, and found a strong negative correlation especially around the footpoint of the Parker spiral (Figure 2.10). This could be a consequence of the correlations between CME speed and TO, and CME speed and peak proton flux, but we may speculate that, in SEP events with shorter TO, the observer may connect to the CME-driven shock wave close to the Sun, while it is still strong and efficient in accelerating particles.

We found that the peak SEP flux appears to be correlated with the magnitude of the solar flare (Figure 2.4(c)). This does not necessarily mean that solar flares produce SEPs. All the flares included in the plot are associated with fast CMEs, and their magnitude is also weakly correlated with the CME speed (Figure 2.4(b)). It is well-established that there are no SEPs from intense flares if there are no CMEs (e.g., flares in AR 12192 in late

October 2014; see Sun et al., 2015), and some of the most intense SEP events in solar cycle 23 were associated with flares that were quite modest (Cliver, 2016). However, the GOES soft X-ray flux data are more readily available for space weather operations in real time. If combined with EUV imagery that shows low coronal signatures for CMEs—such as coronal dimming and post-eruption arcades—the information on solar flares may contribute to SEP forecasting. Another advantage of solar flares is that projection effects may not be as severe as for CMEs in estimating the speed. It is well known that the true speed of a CME may differ from the projected speed, especially when it is launched far from the limb (Burkepile et al., 2004). In this study we used only the speed derived from LASCO observations, which may be an underestimate, especially for halo CMEs. In the future, we plan to compute the 3D speeds of CMEs, using the cone model (Xie et al., 2004) or the graduated cylindrical shell (GCS) model (Thernisien et al., 2006).

2.6 Summary

We conducted a statistical study of the SEP associations of all the fast and wide CMEs that occurred between December 2006 and October 2017. Our primary findings in this chapter are summarized as follows:

1. The SEP association rate is higher for CMEs that come from the range of longitude of E20 – W100 relative to the observer.
2. A CME originating in a well-connected longitude needs to be faster than $\sim$2000 km s^{-1} to ensure 100% association with a SEP event.
3. The correlation of the peak SXR flux with the peak SEP flux is comparable to that of the CME speed only when the flare is associated with a fast and wide CME.
4. The SEP onset time tends to be short when the CME source region is close in longitude (within $\pm 60^\circ$) to the footpoint of the Parker spiral. This trend is still present but weaker for the SEP rise time.
5. There are inverse correlations between the SEP onset timescale and the CME speed in events from regions close in longitude to the footpoint of the Parker spiral.
6. There are positive correlations of the SEP rise timescale and duration with the CME speed.
7. There are inverse correlations between the peak proton flux and onset timescale.

Table 2.1: Properties of Fast and Wide CMEs and Associated SEP Events

CME parameters					GOES		STEREO-A		STEREO-B	
Launch date time	Speed (km s^{-1})	Width (°)	Flare class	Flare site	Quality	Proton peak flux (pfu)	Quality	Proton peak flux (pfu)	Quality	Proton peak flux (pfu)
2006-12-13 02:25	1774	360	X3.4	S06W23	Good	698.0	Good	592.1	Good	567.4
2006-12-14 22:00	1042	360	X1.5	S06W46	Good	215.0	HiB_9	[23.6][a]	HiB_7	[22.1][a]
2007-01-25 06:33	1367	360	C6.3	S08E090	No SEP	—	No SEP	—	No SEP	—
2007-05-19 12:56	958	106	B9.5	N07W06	No SEP	—	No SEP[b]	—	No SEP[b]	—
2007-12-31 00:37	995	164	C8.3	S08E081	No SEP	—	No SEP	—	No SEP	—
2008-03-25 18:37	1103	112	M1.7	S13E078	No SEP	—	No SEP	—	No SEP	—
2010-02-12 22:13	1180	120	C3.0	N25W56	No SEP	—	No SEP	—	No SEP	—
2010-02-13 21:36	1005	63	—	N30W63	No SEP	—	No SEP	—	No SEP	—
2010-03-01 22:35	1518	87	—	N26E075	No SEP	—	No SEP	—	No SEP	—
2010-03-06 07:35	1009	127	B5.2	N25E15	No SEP	—	No SEP	—	No SEP	—
2010-03-13 16:45	1258	95	—	N31W73	No SEP	—	No SEP	—	No SEP	—
2010-08-14 09:49	1205	360	C4.4	N17W52	Good	14.2	No SEP[b]	—	No SEP[b]	—
2010-08-18 05:29	1471	184	C4.5	N17W101	Good	3.7	Good	3.7	No SEP[b]	—
2010-08-31 20:40	1304	360	—	S22W146	No SEP[b]	—	Good	1.2	No SEP	—
2011-02-24 07:16	1186	158	M3.5	N16E83	No SEP	—	No SEP	—	No SEP	—
2011-03-07 19:51	2125	360	M3.7	N30W48	Good	47.7	Contaminated	62.4	HiB_3	—
2011-03-19 12:03	1102	140	—	S25W109	No SEP	—	No SEP	—	No SEP	—
2011-03-21 02:13	1341	360	—	N16W129	Good	8.0	Good	1102.9	No SEP	—
2011-03-29 20:14	1264	195	—	N20E117	No SEP	—	Good	1.2	Good	4.1
2011-04-04 13:48	2081	109	—	N20E133	No SEP[b]	—	No SEP	—	No SEP	—
2011-04-27 02:21	924	257	C2.0	N17E57	No SEP	—	No SEP	—	No SEP	—
2011-05-06 08:36	1024	169	—	N17E139	No SEP	—	No SEP	—	No SEP	—
2011-05-09 20:39	1318	292	C5.4	N18E93	No SEP[b]	—	No SEP	—	Good	1.3
2011-05-18 18:02	1105	126	C2.0	N09W95	No SEP	—	No SEP[b]	—	No SEP	—

CME parameters					GOES		STEREO-A		STEREO-B	
Launch date time	Speed (km s^{-1})	Width (°)	Flare class	Flare site	Quality	Proton peak flux (pfu)	Quality	Proton peak flux (pfu)	Quality	Proton peak flux (pfu)
2011-05-29 20:53	1407	186	C8.7	S19E72	No SEP	—	No SEP	—	No data	—
2011-06-02 07:43	976	360	C3.7	S19E25	No SEP	—	No SEP	—	No SEP[b]	—
2011-06-04 06:26	1407	360	—	N16W144	No SEP	—	Contaminated	159.2	No SEP	—
2011-06-04 21:47	2425	360	—	N16W153	Contaminated	4.9	HiB_90	[777.0][a]	Good	20.7
2011-06-07 06:15	1255	360	M2.5	S21W54	Good	52.7	HiB_50	—	HiB_6	—
2011-06-13 03:37	957	360	—	S19E135	HiB_4	—	No SEP	—	HiB_2	—
2011-07-09 16:10	991	90	—	N24W120	No SEP	—	No SEP	—	No SEP	—
2011-08-04 03:39	1315	360	M9.3	N19W36	Contaminated	80.1	No SEP[b]	—	No SEP[b]	—
2011-08-08 17:53	1343	237	M3.5	N16W61	Good	4.0	No SEP	—	No SEP	—
2011-08-08 22:49	1070	74	C5.3	N19W65	HiB_1	—	No SEP	—	No SEP	—
2011-08-09 03:24	1146	141	M2.5	N18W68	HiB_0.7	—	No SEP	—	No SEP	—
2011-08-09 07:52	1610	360	X6.9	N17W69	Good	26.9	No SEP	—	No SEP	—
2011-08-11 10:10	1160	167	C6.2	N15W97	No SEP	—	No data	—	No SEP	—
2011-09-07 18:23	924	188	—	N19E142	HiB_3	—	No SEP[b]	—	No SEP	—
2011-09-08 21:53	983	281	—	N19W147	No SEP	—	No SEP[b]	—	No SEP	—
2011-09-21 22:00	1007	255	—	N19W120	No SEP[b]	—	No SEP[b]	—	No SEP	—
2011-09-22 10:33	1905	360	X1.4	N09E89	Contaminated	6.8	Good	11.0	Good	2095.7
2011-09-24 09:27	1936	145	X1.9	N12E60	HiB_10	—	HiB_3	—	Multiple	—
2011-09-24 12:38	1915	360	M7.1	N10E56	HiB_10	—	HiB_2	—	HiB_100	[396.8][a]
2011-09-24 19:07	972	360	M3.0	N12E42	HiB_10	—	HiB_1	—	Multiple	—
2011-10-01 20:28	1238	360	—	N24E119	No SEP	—	No SEP	—	No SEP	—
2011-10-04 12:32	1101	360	—	N26E153	No SEP	—	Good	4.8	Good	20.7
2011-10-22 10:18	1005	360	M1.3	N25W77	Good	4.0	No SEP[b]	—	No SEP	—
2011-11-03 21:42	991	360	—	N09E154	Good	3.7	Good	210.5	Good	4.1
2011-11-09 12:57	907	360	M1.1	N24E35	No SEP	—	No SEP	—	No SEP[b]	—
2011-11-17 20:15	1041	360	—	N18E120	No SEP	—	No SEP[b]	—	Good	3.1

CME parameters					GOES		STEREO-A		STEREO-B	
Launch date time	Speed (km s^{-1})	Width (°)	Flare class	Flare site	Quality	Proton peak flux (pfu)	Quality	Proton peak flux (pfu)	Quality	Proton peak flux (pfu)
2011-11-26 06:52	933	360	C1.2	N17W49	Good	80.3	Good	17.4	No SEP[b]	—
2011-12-17 10:23	987	247	—	N26W121	No SEP	—	No SEP[b]	—	No SEP	—
2011-12-19 12:12	1092	154	—	S16W150	No SEP	—	No SEP	—	No SEP	—
2011-12-21 02:39	1064	360	—	S22E151	No SEP	—	No SEP	—	No SEP	—
2011-12-30 19:02	960	179	—	N54W158	No SEP	—	No SEP	—	No SEP	—
2012-01-02 14:45	1138	360	C2.4	N08W104	No SEP[b]	—	No SEP[b]	—	No SEP	—
2012-01-16 02:54	1060	360	C6.5	N34E86	No SEP	—	No SEP	—	Good	1.6
2012-01-19 14:41	1120	360	M3.2	N32E22	Good	3.5	No SEP	—	Good	17.0
2012-01-23 03:45	2175	360	M8.7	N28W21	Contaminated	2820.0	Good	48.4	Good	55.1
2012-01-26 04:41	1194	360	C6.4	N35W60	HiB_70	—	HiB_40	—	HiB_1	—
2012-01-27 18:18	2508	360	X1.7	N27W78	Good	796.0	Multiple	—	HiB_1	—
2012-02-25 14:36	1039	97	—	N19E93	HiB_2	—	No SEP[b]	—	No SEP	—
2012-03-03 18:13	1078	192	C1.9	N17E67	No SEP	—	No SEP	—	No SEP[b]	—
2012-03-04 10:40	1306	360	M2.0	N19E61	Contaminated	3.9	No SEP	—	Good	209.6
2012-03-05 03:31	1531	360	X1.1	N17E52	HiB_1	—	No SEP[b]	—	HiB_100	—
2012-03-07 00:16	2684	360	X5.4	N17E27	Contaminated	1630.0	Contaminated	5.8	Contaminated	233.7
2012-03-07 00:56	1825	360	X1.3	N15E26	Multiple	—	Multiple	—	Multiple	—
2012-03-09 03:43	950	360	M6.3	N15W03	HiB_500	—	HiB_4	—	HiB_80	—
2012-03-10 17:35	1296	360	M8.4	N17W24	HiB_100	—	HiB_20	—	HiB_10	—
2012-03-13 17:20	1884	360	M7.9	N17W66	Good	469.0	HiB_10	—	HiB_3	—
2012-03-18 00:04	1210	360	—	N18W116	No SEP	—	Contaminated	3.0	No SEP[b]	—
2012-03-21 07:12	1178	360	—	N18W160	No SEP	—	Good	58.1	No SEP	—
2012-03-23 23:58	1152	360	—	N18E164	No SEP	—	Good	138.3	Contaminated	2.6
2012-03-26 22:38	1390	360	—	N17E124	No SEP	—	No SEP	—	HiB_6	[21.1][a]
2012-03-27 02:46	1148	162	C5.3	N19W05	No SEP	—	No SEP	—	HiB_20	[95.9][a]
2012-03-28 01:24	1033	360	—	N21E116	No SEP	—	No SEP	—	HiB_50	[89.0][a]

CME parameters					GOES		STEREO-A		STEREO-B	
Launch date time	Speed (km s^{-1})	Width (°)	Flare class	Flare site	Quality	Proton peak flux (pfu)	Quality	Proton peak flux (pfu)	Quality	Proton peak flux (pfu)
2012-04-09 12:11	921	360	C3.9	N20W65	No SEP	—	No SEP	—	No SEP	—
2012-04-15 02:06	1220	173	C1.7	N10E90	No SEP	—	No SEP[b]	—	No SEP[b]	—
2012-04-16 00:07	1128	81	C1.8	N12E88	No SEP	—	No SEP	—	No SEP	—
2012-04-16 17:16	1348	166	M1.7	N14E88	No SEP	—	No SEP	—	No SEP	—
2012-04-30 07:19	992	135	C3.9	S18W88	No SEP	—	No SEP	—	No SEP	—
2012-05-17 01:25	1582	360	M5.1	N11W76	Good	255.0	Contaminated	2.7[c]	No SEP[b]	—
2012-05-26 20:29	1966	360	—	N15W121	Good	14.5	Contaminated	13.5	No SEP[b]	—
2012-06-02 04:12	1175	130	C1.5	N16E42	No SEP	—	No SEP	—	No SEP	—
2012-06-08 00:18	992	72	—	N16W42	No SEP	—	No SEP	—	No SEP	—
2012-06-14 13:39	987	360	M1.9	S17E06	No SEP[b]	—	No SEP	—	No SEP[b]	—
2012-06-23 06:57	1263	360	C2.7	N18W101	No SEP	—	No SEP	—	No SEP	—
2012-06-26 12:28	920	89	C1.3	N21E77	No SEP	—	No SEP	—	No SEP	—
2012-06-28 19:29	1313	145	C1.7	N18E48	No SEP	—	Multiple	—	No SEP[b]	—
2012-07-02 06:10	988	134	—	S09W58	No SEP	—	Multiple	—	Multiple	—
2012-07-02 08:03	1074	360	—	S16E134	No SEP	—	No SEP[b]	—	Good	7.0
2012-07-05 21:15	980	94	M1.6	S12W46	No SEP	—	No SEP	—	No SEP	—
2012-07-06 02:34	1059	73	M1.0	S12W48	No SEP	—	No SEP	—	No SEP	—
2012-07-06 22:54	1828	360	X1.1	S13W59	Good	25.2	No SEP[b]	—	No SEP	—
2012-07-08 16:08	1572	157	M6.9	S17W74	HiB_2	[19.2][a]	Multiple	—	No SEP	—
2012-07-09 05:32	1199	63	C4.6	S14W91	HiB_20	—	HiB_10	—	No SEP	—
2012-07-17 14:03	958	176	C9.9	S15W65	Good	110.0	No SEP	—	No SEP	—
2012-07-19 05:13	1631	360	M7.7	S13W88	HiB_20	[79.6][a]	HiB_1	[13.9][a]	No SEP	—
2012-07-23 02:15	2003	360	—	S17W132	Good	12.8	Good	49778.4	Good	31.0
2012-08-17 04:42	931	137	C1.8	N19E98	No SEP	—	No SEP	—	No SEP	—
2012-08-17 12:07	910	64	B7.8	N19E99	No SEP	—	No SEP	—	No SEP	—
2012-08-18 00:35	986	145	C1.4	N19E86	No SEP	—	No SEP	—	No SEP	—

CME parameters					GOES		STEREO-A		STEREO-B	
Launch date time	Speed (km s^{-1})	Width (°)	Flare class	Flare site	Quality	Proton peak flux (pfu)	Quality	Proton peak flux (pfu)	Quality	Proton peak flux (pfu)
2012-08-21 19:52	1024	360	—	S22E156	No SEP	—	HiB_1	[1.6][a]	No SEP	—
2012-08-31 19:44	1442	360	C8.4	S19E42	Good	44.3	No SEP	—	Good	999.9
2012-09-20 14:31	1202	360	—	S15E155	No SEP	—	HiB_10	[281.8][a]	Contaminated	12.3
2012-09-23 14:51	939	258	C1.7	S08E105	No SEP[b]	—	HiB_5	—	HiB_20	—
2012-09-27 09:57	1319	360	—	S25W151	No SEP	—	Contaminated	95.4	No SEP	—
2012-09-27 23:31	947	360	C3.7	N09W31	Good	28.4	Multiple	—	Good	22.3
2012-10-14 00:14	987	360	—	N13E137	No SEP	—	Good	3.2	No SEP[b]	—
2012-11-08 10:38	972	360	—	S14W160	Good	2.4	Good	37.3	No SEP	—
2012-11-21 03:45	920	360	—	N11W99	No SEP	—	No SEP	—	No SEP	—
2012-11-23 23:00	1186	360	—	N14W130	No SEP	—	Good	5.1	No SEP	—
2012-12-05 00:01	963	231	C1.7	N14E83	No SEP	—	No SEP	—	No SEP	—
2013-01-15 03:55	966	81	C1.1	S32W58	No SEP	—	No SEP	—	No SEP	—
2013-02-06 00:06	1867	271	C8.7	N22E19	No SEP[b]	—	No SEP[b]	—	No SEP[b]	—
2013-02-12 22:52	1050	165	B5.9	S32W58	No SEP	—	No SEP	—	No SEP	—
2013-02-26 09:31	987	360	—	N07W123	No SEP[b]	—	No SEP[b]	—	No SEP	—
2013-03-05 03:23	1316	360	—	N10E144	No SEP	—	Good	1849.9	Good	140.8
2013-03-12 10:14	1024	196	C2.0	N25E001	No SEP	—	No SEP	—	No SEP	—
2013-03-15 06:42	1063	360	M1.1	N11E012	Good	14.7	No SEP	—	No SEP[b]	—
2013-03-22 08:17	972	123	—	N28W126	No SEP	—	No SEP	—	No SEP	—
2013-04-21 07:10	919	360	—	N10W119	Good	3.3	No SEP	—	No SEP	—
2013-05-13 02:00	1270	360	X1.7	N11E90	No SEP	—	No SEP	—	Good	17.8
2013-05-13 15:47	1850	360	X2.8	N11E85	Contaminated	1.3	No SEP[b]	—	Contaminated	108.3
2013-05-14 01:03	2625	360	X3.2	N08E77	HiB_1	—	No SEP	—	HiB_300	[621.0][a]
2013-05-14 22:23	971	63	—	N25E101	HiB_1	—	No SEP	—	HiB_30	—
2013-05-15 01:27	1366	360	X1.2	N12E64	Good	22.0	No SEP	—	HiB_30	—
2013-05-16 07:08	951	63	—	N10E115	HiB_20	—	No SEP	—	HiB_2	—

CME parameters					GOES		STEREO-A		STEREO-B	
Launch date time	Speed (km s^{-1})	Width (°)	Flare class	Flare site	Quality	Proton peak flux (pfu)	Quality	Proton peak flux (pfu)	Quality	Proton peak flux (pfu)
2013-05-17 08:46	1345	360	M3.2	N12E57	HiB_20	—	No SEP	—	No SEP	—
2013-05-22 12:55	1466	360	M5.0	N15W70	Good	1650.0	Contaminated	4.2	No SEP[b]	—
2013-06-16 14:13	1104	96	—	S14E132	No SEP	—	No SEP	—	No SEP[b]	—
2013-06-21 02:53	1900	207	M2.9	S16E73	Good	6.7	No SEP[b]	—	Good	51.4
2013-06-28 01:25	1037	360	C4.4	S18W19	No SEP	—	No SEP	—	No SEP	—
2013-07-18 19:41	939	63	C2.3	S09E77	No SEP	—	No SEP	—	No SEP	—
2013-07-22 05:57	1004	360	—	N16W155	No SEP	—	Good	5.3	No SEP[b]	—
2013-08-17 19:00	1202	360	M1.4	S05W30	No SEP[b]	—	No SEP	—	No SEP	—
2013-08-30 02:04	949	360	C8.3	N15E46	No SEP	—	No SEP	—	Good	4.1
2013-09-24 20:18	919	360	B6.5	N26E70	No SEP	—	No SEP	—	No SEP[b]	—
2013-09-29 21:52	1179	360	C1.3	N17W29	Good	182.0	No SEP[b]	—	Good	1.0
2013-10-05 06:41	964	360	—	S22E118	No SEP	—	Good	42.9	Good	2.3
2013-10-11 07:05	1200	360	—	N21E103	No SEP	—	Good	218.5	Good	21.8
2013-10-25 14:41	1081	360	X2.1	S06E69	No SEP[b]	—	No SEP[b]	—	HiB_20	[47.4][a]
2013-10-28 04:16	1201	156	M5.1	N08W71	Contaminated	4.0	No SEP	—	No SEP	—
2013-10-28 13:44	1073	93	M2.8	N06W75	HiB_3	—	No SEP[b]	—	Good	7.8
2013-10-29 21:28	1001	360	X2.3	N05W89	HiB_3	[4.8][a]	No SEP	—	HiB_2	—
2013-11-04 04:38	1040	360	—	N03W165	No SEP	—	HiB_5	[273.7][a]	HiB_5	—
2013-11-06 23:25	1033	360	M1.8	S11W97	Good	6.7	HiB_5	—	HiB_1	—
2013-11-07 10:03	1405	360	—	N02E151	HiB_3	—	Good	73.9	Good	997.5
2013-12-07 07:11	1085	360	M1.2	S16W49	No SEP	—	No data	—	No SEP	—
2013-12-12 03:08	1002	276	C4.6	S23W46	No SEP[b]	—	No SEP	—	No SEP	—
2013-12-23 07:58	1409	94	—	N25W103	No SEP	—	No SEP	—	No SEP	—
2013-12-26 02:41	1022	171	—	S27E137	Multiple	—	Multiple	—	Multiple	—
2013-12-26 03:02	1336	360	—	S09E166	Good	2.7	Good	54.6	Good	59.4
2013-12-28 17:09	1118	360	—	S15W125	Good	29.3	HiB_1	—	HiB_8	—

CME parameters					GOES		STEREO-A		STEREO-B	
Launch date time	Speed (km s^{-1})	Width (°)	Flare class	Flare site	Quality	Proton peak flux (pfu)	Quality	Proton peak flux (pfu)	Quality	Proton peak flux (pfu)
2013-12-31 10:15	1101	230	C8.8	S09E101	No SEP	—	No SEP	—	No SEP[b]	—
2014-01-04 19:00	977	360	M4.0	S11E34	No SEP[b]	—	No SEP	—	No SEP	—
2014-01-06 07:33	1402	360	—	S15W112	Good	40.1	No data	—	No SEP[b]	—
2014-01-06 09:58	957	76	—	S15E112	HiB_20	—	No data	—	No SEP[b]	—
2014-01-07 18:04	1830	360	X1.2	S15W11	HiB_10	[951.0][a]	No data	—	Good	6.7
2014-01-21 18:16	1035	113	—	S16W115	No SEP	—	Multiple	—	Multiple	—
2014-01-21 20:41	1065	221	—	S13E162	No SEP	—	Good	3.7	Multiple	—
2014-01-24 07:11	973	173	—	S14E130	No SEP	—	No SEP	—	No SEP	—
2014-01-26 08:03	1088	255	C1.5	S16E106	No SEP	—	No SEP	—	No SEP	—
2014-01-30 15:47	1087	360	M6.6	S13E58	No SEP	—	No SEP	—	No SEP[b]	—
2014-02-09 15:38	908	360	M1.0	S15E103	No SEP	—	Good	2.0	No SEP	—
2014-02-14 08:05	1165	360	—	S13W142	No SEP	—	No SEP	—	No SEP	—
2014-02-20 02:33	993	360	—	S17E143	HiB_3	—	No SEP	—	No SEP	—
2014-02-20 07:28	948	360	M3.0	S15W73	Good	22.3	No SEP	—	No SEP	—
2014-02-21 15:28	1252	360	—	S15E121	No SEP	—	No SEP[b]	—	Good	16.1
2014-02-22 12:04	1023	233	—	S34W145	No SEP	—	HiB_1	—	HiB_10	—
2014-02-25 00:32	2147	360	X4.9	S12E82	Contaminated	23.9	Good	205.2	Good	316.7
2014-03-04 21:16	911	86	—	N09E57	HiB_1	—	HiB_3	—	No SEP[b]	—
2014-03-12 14:08	972	360	—	N18E158	No SEP	—	Good	46.1	Good	4.7
2014-04-02 13:22	1471	360	M6.5	N11E53	No SEP	—	No SEP	—	Good	184.4
2014-04-02 23:13	1367	64	—	N14E152	No SEP	—	No SEP	—	HiB_50	—
2014-04-03 06:38	1156	71	C5.5	N10E50	No SEP	—	No SEP	—	HiB_20	—
2014-04-12 06:59	1016	139	C5.0	S12E86	No SEP	—	No SEP	—	No SEP	—
2014-04-18 12:43	1203	360	M7.3	S20W34	Contaminated	58.5	No SEP	—	No SEP	—
2014-05-05 14:57	1069	124	—	N04E102	No SEP	—	No SEP	—	No SEP	—
2014-05-07 15:44	923	360	M1.2	S11W100	No SEP[b]	—	No SEP	—	No SEP	—

CME parameters					GOES		STEREO-A		STEREO-B	
Launch date time	Speed (km s^{-1})	Width (°)	Flare class	Flare site	Quality	Proton peak flux (pfu)	Quality	Proton peak flux (pfu)	Quality	Proton peak flux (pfu)
2014-05-09 01:53	1099	360	—	S11W122	No SEP	—	No SEP	—	No SEP	—
2014-05-10 04:06	1086	360	—	S11W136	No SEP	—	No SEP[b]	—	No SEP	—
2014-06-06 13:28	1200	360	—	S19E132	No SEP	—	No SEP[b]	—	No SEP[b]	—
2014-06-10 11:29	925	111	X2.2	S15E80	No SEP	—	Multiple	—	Multiple	—
2014-06-10 12:44	1469	360	X1.5	S17E82	No SEP	—	Multiple	—	Good	12.3
2014-06-15 12:42	958	190	M1.1	S21W92	No SEP	—	No SEP	—	No SEP	—
2014-06-16 01:24	1088	69	C8.3	S14W107	No SEP	—	No SEP	—	No SEP	—
2014-06-17 08:29	1198	360	—	S13W123	No SEP	—	No SEP	—	No SEP	—
2014-07-01 23:12	969	84	—	S21E112	No SEP	—	No SEP	—	No SEP	—
2014-07-10 06:56	928	275	C1.9	S14W92	No SEP	—	No data	—	No SEP	—
2014-07-28 13:41	1110	127	C2.4	S08E51	No SEP	—	No SEP	—	No SEP[b]	—
2014-08-08 16:13	1137	360	—	S10W160	No SEP	—	No SEP[b]	—	No SEP	—
2014-09-01 10:48	1901	360	—	N14E127	Good	3.5	No data	—	Good	2777.8
2014-09-01 21:58	1404	360	—	S13E113	HiB_0.3	—	No data	—	HiB_3000	—
2014-09-02 02:10	1141	226	—	S15E114	HiB_0.3	—	No data	—	HiB_3000	—
2014-09-08 23:45	920	360	M4.5	N12E029	HiB_4	—	No data	—	HiB_1	—
2014-09-10 17:00	1071	134	—	N11W169	Multiple	—	No data	—	Multiple	—
2014-09-10 17:27	1267	360	X1.6	N14E002	Contaminated	28.7	No data	—	Good	2.3
2014-09-24 20:50	1350	360	—	N13E179	No SEP	—	No data	—	Contaminated	40.5
2014-09-26 04:15	1469	360	—	S13E111	No SEP	—	No data	—	HiB_200	—
2014-11-01 04:54	1628	159	C2.7	S26E052	Good	4.9	No data	—	No Data	—
2014-12-10 17:56	1086	228	C5.9	S21W104	No SEP	—	No data	—	No Data	—
2014-12-12 04:02	1133	127	C1.2	N16W05	No data	—	No data	—	No Data	—
2014-12-13 14:02	2222	360	—	S20W143	No data	—	No data	—	No Data	—
2014-12-18 22:02	1195	360	M6.9	S11E015	No SEP	—	No data	—	No Data	—
2014-12-26 05:10	1097	156	—	S15W110	No SEP	—	No SEP	—	No Data	—

CME parameters					GOES		STEREO-A		STEREO-B	
Launch date time	Speed (km s^{-1})	Width (°)	Flare class	Flare site	Quality	Proton peak flux (pfu)	Quality	Proton peak flux (pfu)	Quality	Proton peak flux (pfu)
2014-12-30 20:14	902	126	—	S14W147	No SEP	—	No data	—	No Data	—
2015-01-12 15:11	1078	210	C3.7	S12E041	No SEP	—	No data	—	No Data	—
2015-02-09 23:14	1106	360	M2.4	N12E061	No SEP	—	No data	—	No Data	—
2015-02-21 09:18	1120	360	—	S16W164	Good	1.3	No data	—	No Data	—
2015-03-07 21:58	1261	360	M9.2	S19E074	No SEP	—	No data	—	No Data	—
2015-03-09 23:25	995	360	M5.8	S18E045	No SEP	—	No data	—	No Data	—
2015-03-10 03:01	1040	360	M5.1	S15E040	No SEP	—	No data	—	No Data	—
2015-04-21 12:53	1079	83	—	N21E088	No SEP[b]	—	No Data	—	No Data	—
2015-06-09 19:48	1036	262	C2.8	S03E025	No SEP	—	No Data	—	No Data	—
2015-06-14 04:11	1228	195	C5.9	S12W34	No SEP	—	No Data	—	No Data	—
2015-06-18 00:55	1714	195	M1.2	S16W81	Good	16.8	No Data	—	No Data	—
2015-06-18 16:55	1305	360	M3.0	N15E050	HiB_10	—	No Data	—	No Data	—
2015-06-21 02:15	1366	360	M2.6	N12E016	Contaminated	114.0	No Data	—	No Data	—
2015-06-22 17:58	1209	360	M6.5	N12W08	HiB_300	—	No Data	—	No Data	—
2015-06-25 08:17	1627	360	M7.9	N09W42	Good	16.3	No Data	—	No Data	—
2015-09-20 18:00	1239	360	M2.1	S20W24	Good	3.2	No data	—	No Data	—
2015-10-07 07:29	900	145	—	S25W69	No SEP	—	No data	—	No Data	—
2015-11-09 13:06	1041	273	M3.9	S11E041	Good	3.7	No data	—	No Data	—
2015-12-28 11:56	1212	360	M1.8	S23W11	Good	3.7	No SEP	—	No Data	—
2016-01-01 23:15	1730	360	M2.3	S25W82	Good	21.5	No SEP	—	No Data	—
2016-01-06 13:51	969	360	—	S20W133	No SEP	—	No SEP	—	No Data	—
2016-01-29 20:57	901	118	C2.0	S24W66	No SEP	—	No SEP	—	No Data	—
2016-04-18 00:14	1084	162	M6.7	N12W62	No SEP[b]	—	No SEP	—	No Data	—
2016-05-15 15:20	1118	176	C3.2	N10W62	Good	2.2	No SEP	—	No Data	—
2017-04-18 19:27	926	360	C5.5	N14E77	No SEP	—	Good	10.8	No Data	—
2017-07-14 01:12	1200	360	M2.4	S06W29	Good	13.6	No SEP	—	No Data	—

CME parameters					GOES		STEREO-A		STEREO-B	
Launch date time	Speed (km s^{-1})	Width (°)	Flare class	Flare site	Quality	Proton peak flux (pfu)	Quality	Proton peak flux (pfu)	Quality	Proton peak flux (pfu)
2017-07-23 04:33	1848	360	—	S09W151	No SEP	—	Good	1523.2	No Data	—
2017-09-04 20:21	1418	360	M5.5	S10W12	Good	106.0	No SEP	—	No Data	—
2017-09-06 12:01	1571	360	X9.3	S08W33	HiB_20	[352.0][a]	No SEP	—	No Data	—
2017-09-09 22:33	1019	138	M1.1	S09W89	HiB_1	—	No SEP	—	No Data	—
2017-09-10 15:50	3163	360	X8.2	S09W90	Good	1040.0	Contaminated	6.9	No Data	—
2017-09-17 11:37	1385	360	—	S08E170	No SEP	—	HiB_7	—	No Data	—
2017-10-18 05:24	1576	360	—	S12E122	No SEP	—	Good	5.2	No Data	—

[a] We found a SEP event around the peak even though we missed the onset.

[b] The proton flux increased, but did not reach 1 pfu.

[c] The peak proton flux may be underestimated due to an energetic storm particle (ESP).

Table 2.2: Timescales of SEP Events

CME parameters					GOES		STEREO-A		STEREO-B	
Launch date time	Speed (km s^{-1})	Width (°)	Flare site	Instrument	quality	Proton peak flux (pfu)	TO (min)	TR (min)	TD (min)	Tm (min)
2006-12-13 02:25	1774	360	S06W23	GOES	Good	698.0	30.0	180.0	605	420.0
2006-12-14 22:00	1042	360	S06W46	GOES	Good	215.0	65.0	45.0	75	135.0
2010-08-14 09:49	1205	360	N17W52	GOES	Good	14.2	76.0	50.0	280	176.0
2010-08-18 05:29	1471	184	N17W101	GOES	Good	3.7	171.0	70.0	630	321.0
2011-03-07 19:51	2125	360	N30W48	GOES	Good	47.7	114.0	240.0	1415	539.0
2011-03-21 02:13	1341	360	N16W129	GOES	Good	8.0	122.0	180.0	1785	522.0
2011-06-04 21:47	2425	360	N16W153	GOES	Contaminated	4.9	658.0	870.0	—	1818.0
2011-06-07 06:15	1255	360	S21W54	GOES	Good	52.7	65.0	125.0	1115	245.0
2011-08-04 03:39	1315	360	N19W36	GOES	Contaminated	80.1	56.0	150.0	—	411.0
2011-08-08 17:53	1343	237	N16W61	GOES	Good	4.0	57.0	45.0	115	127.0
2011-08-09 07:52	1610	360	N17W69	GOES	Good	26.9	28.0	30.0	465	258.0
2011-09-22 10:33	1905	360	N09E89	GOES	Contaminated	6.8	342.0	785.0	—	1347.0
2011-10-22 10:18	1005	360	N25W77	GOES	Good	4.0	172.0	380.0	3005	767.0
2011-11-03 21:42	991	360	N09E154	GOES	Good	3.7	188.0	405.0	1460	683.0
2011-11-26 06:52	933	360	N17W49	GOES	Good	80.3	88.0	480.0	1330	1113.0
2012-01-19 14:41	1120	360	N32E22	GOES	Good	3.5	1074.0	545.0	570	1749.0
2012-01-23 03:45	2175	360	N28W21	GOES	Contaminated	2820.0	60.0	305.0	—	705.0
2012-01-27 18:18	2508	360	N27W78	GOES	Good	796.0	37.0	230.0	1250	467.0
2012-03-04 10:40	1306	360	N19E61	GOES	Contaminated	3.9	670.0	645.0	—	1790.0
2012-03-07 00:16	2684	360	N17E27	GOES	Contaminated	1630.0	154.0	660.0	—	919.0
2012-03-13 17:20	1884	360	N17W66	GOES	Good	469.0	45.0	65.0	355	205.0
2012-05-17 01:25	1582	360	N11W76	GOES	Good	255.0	30.0	100.0	305	185.0
2012-05-26 20:29	1966	360	N15W121	GOES	Good	14.5	156.0	345.0	495	586.0
2012-07-06 22:54	1828	360	S13W59	GOES	Good	25.2	81.0	230.0	695	531.0

CME parameters					GOES		STEREO-A		STEREO-B	
Launch date time	Speed (km s^{-1})	Width (°)	Flare site	Instrument	quality	Proton peak flux (pfu)	TO (min)	TR (min)	TD (min)	Tm (min)
2012-07-17 14:03	958	176	S15W65	GOES	Good	110.0	107.0	240.0	705	547.0
2012-07-23 02:15	2003	360	S17W132	GOES	Good	12.8	320.0	275.0	3790	1170.0
2012-08-31 19:44	1442	360	S19E42	GOES	Good	44.3	341.0	790.0	2015	1586.0
2012-09-27 23:31	947	360	N09W31	GOES	Good	28.4	109.0	140.0	175	314.0
2012-11-08 10:38	972	360	S14W160	GOES	Good	2.4	232.0	765.0	1800	1062.0
2013-03-15 06:42	1063	360	N11E012	GOES	Good	14.7	763.0	900.0	1435	2348.0
2013-04-21 07:10	919	360	N10W119	GOES	Good	3.3	165.0	70.0	1440	570.0
2013-05-13 15:47	1850	360	N11E85	GOES	Contaminated	1.3	323.0	205.0	—	1018.0
2013-05-15 01:27	1366	360	N12E64	GOES	Good	22.0	288.0	435.0	2450	1048.0
2013-05-22 12:55	1466	360	N15W70	GOES	Good	1650.0	65.0	660.0	670	1010.0
2013-06-21 02:53	1900	207	S16E73	GOES	Good	6.7	707.0	475.0	1570	1797.0
2013-09-29 21:52	1179	360	N17W29	GOES	Good	182.0	138.0	775.0	1825	1333.0
2013-10-28 04:16	1201	156	N08W71	GOES	Contaminated	4.0	139.0	225.0	—	1014.0
2013-11-06 23:25	1033	360	S11W97	GOES	Good	6.7	155.0	55.0	455	310.0
2013-12-26 03:02	1336	360	S09E166	GOES	Good	2.7	358.0	495.0	1630	1428.0
2013-12-28 17:09	1118	360	S15W125	GOES	Good	29.3	121.0	180.0	370	366.0
2014-01-06 07:33	1402	360	S15W112	GOES	Good	40.1	42.0	100.0	1380	282.0
2014-02-20 07:28	948	360	S15W73	GOES	Good	22.3	52.0	35.0	150	117.0
2014-02-25 00:32	2147	360	S12E82	GOES	Contaminated	23.9	183.0	685.0	—	1418.0
2014-04-18 12:43	1203	360	S20W34	GOES	Contaminated	58.5	62.0	330.0	—	742.0
2014-09-01 10:48	1901	360	N14E127	GOES	Good	3.5	677.0	1175.0	10495	3402.0
2014-09-10 17:27	1267	360	N14E002	GOES	Contaminated	28.7	248.0	345.0	—	708.0
2014-11-01 04:54	1628	159	S26E052	GOES	Good	4.9	541.0	270.0	2600	921.0
2015-02-21 09:18	1120	360	S16W164	GOES	Good	1.3	312.0	85.0	2240	607.0
2015-06-18 00:55	1714	195	S16W81	GOES	Good	16.8	200.0	285.0	1365	830.0
2015-06-21 02:15	1366	360	N12E016	GOES	Contaminated	114.0	70.0	1290.0	—	1540.0

CME parameters					GOES		STEREO-A		STEREO-B	
Launch date time	Speed (km s^{-1})	Width (°)	Flare site	Instrument	quality	Proton peak flux (pfu)	TO (min)	TR (min)	TD (min)	Tm (min)
2015-06-25 08:17	1627	360	N09W42	GOES	Good	16.3	103.0	885.0	2160	1563.0
2015-09-20 18:00	1239	360	S20W24	GOES	Good	3.2	75.0	75.0	185	165.0
2015-11-09 13:06	1041	273	S11E041	GOES	Good	3.7	404.0	215.0	385	674.0
2015-12-28 11:56	1212	360	S23W11	GOES	Good	3.7	144.0	570.0	395	834.0
2016-01-01 23:15	1730	360	S25W82	GOES	Good	21.5	60.0	255.0	200	335.0
2016-05-15 15:20	1118	176	N10W62	GOES	Good	2.2	195.0	145.0	245	360.0
2017-07-14 01:12	1200	360	S06W29	GOES	Good	13.6	158.0	140.0	1860	583.0
2017-09-04 20:21	1418	360	S10W12	GOES	Good	106.0	129.0	280.0	1415	659.0
2017-09-10 15:50	3163	360	S09W90	GOES	Good	1040.0	35.0	85.0	2075	175.0
2006-12-13 02:25	1774	360	S06W23	STEREO-A	Good	592.1	42.5	155.0	705	372.5
2010-08-18 05:29	1471	184	N17W101	STEREO-A	Good	3.7	78.5	145.0	190	228.5
2010-08-31 20:40	1304	360	S22W146	STEREO-A	Good	1.2	132.5	140.0	530	377.5
2011-03-07 19:51	2125	360	N30W48	STEREO-A	Contaminated	62.4	361.5	1845.0	—	2266.5
2011-03-21 02:13	1341	360	N16W129	STEREO-A	Good	1102.9	39.5	80.0	320	159.5
2011-03-29 20:14	1264	195	N20E117	STEREO-A	Good	1.2	518.5	470.0	550	1168.5
2011-06-04 06:26	1407	360	N16W144	STEREO-A	Contaminated	159.2	136.5	475.0	—	646.5
2011-09-22 10:33	1905	360	N09E89	STEREO-A	Good	11.0	304.5	610.0	1865	984.5
2011-10-04 12:32	1101	360	N26E153	STEREO-A	Good	4.8	210.5	405.0	1570	880.5
2011-11-03 21:42	991	360	N09E154	STEREO-A	Good	210.5	80.5	125.0	320	315.5
2011-11-26 06:52	933	360	N17W49	STEREO-A	Good	17.4	510.5	1015.0	1005	2295.5
2012-01-23 03:45	2175	360	N28W21	STEREO-A	Good	48.4	357.5	1585.0	3350	2297.5
2012-03-07 00:16	2684	360	N17E27	STEREO-A	Contaminated	5.8	196.5	500.0	—	1686.5
2012-03-18 00:04	1210	360	N18W116	STEREO-A	Contaminated	3.0	178.5	55.0	—	318.5
2012-03-21 07:12	1178	360	N18W160	STEREO-A	Good	58.1	75.5	85.0	515	315.5
2012-03-23 23:58	1152	360	N18E164	STEREO-A	Good	138.3	54.5	75.0	165	179.5
2012-05-17 01:25[a]	1582	360	N11W76	STEREO-A	Contaminated	2.7	647.5	1015.0	—	2107.5

CME parameters					GOES		STEREO-A		STEREO-B	
Launch date time	Speed (km s^{-1})	Width (°)	Flare site	Instrument	quality	Proton peak flux (pfu)	TO (min)	TR (min)	TD (min)	Tm (min)
2012-05-26 20:29	1966	360	N15W121	STEREO-A	Contaminated	13.5	58.5	45.0	—	113.5
2012-07-23 02:15	2003	360	S17W132	STEREO-A	Good	49778.4	62.5	995.0	160	1117.5
2012-09-27 09:57	1319	360	S25W151	STEREO-A	Contaminated	95.4	85.5	130.0	—	220.5
2012-10-14 00:14	987	360	N13E137	STEREO-A	Good	3.2	83.5	65.0	1040	323.5
2012-11-08 10:38	972	360	S14W160	STEREO-A	Good	37.3	39.5	80.0	2560	269.5
2012-11-23 23:00	1186	360	N14W130	STEREO-A	Good	5.1	117.5	575.0	655	927.5
2013-03-05 03:23	1316	360	N10E144	STEREO-A	Good	1849.9	29.5	120.0	790	354.5
2013-05-22 12:55	1466	360	N15W70	STEREO-A	Contaminated	4.2	517.5	315.0	—	977.5
2013-07-22 05:57	1004	360	N16W155	STEREO-A	Good	5.3	95.5	125.0	235	260.5
2013-10-05 06:41	964	360	S22E118	STEREO-A	Good	42.9	86.5	380.0	715	756.5
2013-10-11 07:05	1200	360	N21E103	STEREO-A	Good	218.5	42.5	80.0	385	237.5
2013-11-07 10:03	1405	360	N02E151	STEREO-A	Good	73.9	54.5	50.0	725	249.5
2013-12-26 03:02	1336	360	S09E166	STEREO-A	Good	54.6	115.5	390.0	1375	660.5
2014-01-21 20:41	1065	221	S13E162	STEREO-A	Good	3.7	166.5	325.0	695	521.5
2014-02-09 15:38	908	360	S15E103	STEREO-A	Good	2.0	124.5	40.0	435	244.5
2014-02-25 00:32	2147	360	S12E82	STEREO-A	Good	205.2	60.5	115.0	825	325.5
2014-03-12 14:08	972	360	N18E158	STEREO-A	Good	46.1	69.5	70.0	110	164.5
2017-04-18 19:27	926	360	N14E77	STEREO-A	Good	10.8	110.5	115.0	635	310.5
2017-07-23 04:33	1848	360	S09W151	STEREO-A	Good	1523.2	149.5	925.0	1390	1519.5
2017-09-10 15:50	3163	360	S09W90	STEREO-A	Contaminated	6.9	907.5	1630.0	—	2702.5
2017-10-18 05:24	1576	360	S12E122	STEREO-A	Good	5.2	93.5	690.0	1100	973.5
2006-12-13 02:25	1774	360	S06W23	STEREO-B	Good	567.4	37.5	165.0	705	342.5
2011-03-29 20:14	1264	195	N20E117	STEREO-B	Good	4.1	703.5	770.0	1595	1578.5
2011-05-09 20:39	1318	292	N18E93	STEREO-B	Good	1.3	213.5	265.0	725	598.5
2011-06-04 21:47	2425	360	N16W153	STEREO-B	Good	20.7	755.5	3115.0	5350	5285.5
2011-09-22 10:33	1905	360	N09E89	STEREO-B	Good	2095.7	44.5	520.0	1875	989.5

CME parameters					GOES		STEREO-A		STEREO-B	
Launch date time	Speed (km s^{-1})	Width (°)	Flare site	Instrument	quality	Proton peak flux (pfu)	TO (min)	TR (min)	TD (min)	Tm (min)
2011-10-04 12:32	1101	360	N26E153	STEREO-B	Good	20.7	160.5	170.0	675	530.5
2011-11-03 21:42	991	360	N09E154	STEREO-B	Good	4.1	110.5	85.0	1730	250.5
2011-11-17 20:15	1041	360	N18E120	STEREO-B	Good	3.1	262.5	370.0	655	827.5
2012-01-16 02:54	1060	360	N34E86	STEREO-B	Good	1.6	358.5	1295.0	1885	1803.5
2012-01-19 14:41	1120	360	N32E22	STEREO-B	Good	17.0	186.5	365.0	1595	776.5
2012-01-23 03:45	2175	360	N28W21	STEREO-B	Good	55.1	137.5	190.0	2610	377.5
2012-03-04 10:40	1306	360	N19E61	STEREO-B	Good	209.6	262.5	500.0	355	927.5
2012-03-07 00:16	2684	360	N17E27	STEREO-B	Contaminated	233.7	71.5	85.0	—	221.5
2012-03-23 23:58	1152	360	N18E164	STEREO-B	Contaminated	2.6	384.5	355.0	—	854.5
2012-07-02 08:03	1074	360	S16E134	STEREO-B	Good	7.0	834.5	1610.0	335	2574.5
2012-07-23 02:15	2003	360	S17W132	STEREO-B	Good	31.0	957.5	1460.0	5335	2942.5
2012-08-31 19:44	1442	360	S19E42	STEREO-B	Good	999.9	53.5	495.0	1430	1053.5
2012-09-20 14:31	1202	360	S15E155	STEREO-B	Contaminated	12.3	46.5	830.0	—	1171.5
2012-09-27 23:31	947	360	N09W31	STEREO-B	Good	22.3	191.5	160.0	160	386.5
2013-03-05 03:23	1316	360	N10E144	STEREO-B	Good	140.8	134.5	2475.0	895	3409.5
2013-05-13 02:00	1270	360	N11E90	STEREO-B	Good	17.8	72.5	65.0	255	217.5
2013-05-13 15:47	1850	360	N11E85	STEREO-B	Contaminated	108.3	95.5	110.0	—	300.5
2013-06-21 02:53	1900	207	S16E73	STEREO-B	Good	51.4	94.5	155.0	1115	469.5
2013-08-30 02:04	949	360	N15E46	STEREO-B	Good	4.1	103.5	95.0	350	293.5
2013-09-29 21:52	1179	360	N17W29	STEREO-B	Good	1.0	640.5	505.0	1510	1475.5
2013-10-05 06:41	964	360	S22E118	STEREO-B	Good	2.3	596.5	840.0	1740	1996.5
2013-10-11 07:05	1200	360	N21E103	STEREO-B	Good	21.8	72.5	215.0	2005	682.5
2013-10-28 13:44	1073	93	N06W75	STEREO-B	Good	7.8	183.5	245.0	930	1138.5
2013-11-07 10:03	1405	360	N02E151	STEREO-B	Good	997.5	79.5	345.0	1360	704.5
2013-12-26 03:02	1336	360	S09E166	STEREO-B	Good	59.4	100.5	355.0	2300	750.5
2014-01-07 18:04	1830	360	S15W11	STEREO-B	Good	6.7	253.5	1395.0	1390	2023.5

CME parameters					GOES		STEREO-A		STEREO-B	
Launch date time	Speed (km s^{-1})	Width (°)	Flare site	Instrument	quality	Proton peak flux (pfu)	TO (min)	TR (min)	TD (min)	Tm (min)
2014-02-21 15:28	1252	360	S15E121	STEREO-B	Good	16.1	74.5	170.0	1115	539.5
2014-02-25 00:32	2147	360	S12E82	STEREO-B	Good	316.7	65.5	185.0	2445	610.5
2014-03-12 14:08	972	360	N18E158	STEREO-B	Good	4.7	129.5	290.0	800	719.5
2014-04-02 13:22	1471	360	N11E53	STEREO-B	Good	184.4	120.5	55.0	315	220.5
2014-06-10 12:44	1469	360	S17E82	STEREO-B	Good	12.3	128.5	140.0	445	388.5
2014-09-01 10:48	1901	360	N14E127	STEREO-B	Good	2777.8	49.5	140.0	1925	489.5
2014-09-10 17:27	1267	360	N14E002	STEREO-B	Good	2.3	220.5	205.0	1815	955.5
2014-09-24 20:50	1350	360	N13E179	STEREO-B	Contaminated	40.5	92.5	385.0	—	677.5

[a] Peak proton flux and timescales may be underestimated due to an energetic storm particle (ESP).

CHAPTER 3

Solar Energetic Particle Events with Short and Long Onset Times

The content of this chapter is based on Kihara et al. (2022, submitted). Some content has been changed due to the structure of the thesis.

3.1 Introduction

The three timescales introduced by Kahler (2005) and the associated results presented in Chapters 1 and 2 are summarized again. The three timescales are as follows, TO: the SEP onset time with respect to the CME launch, TR: the rise time from the SEP onset time to the SEP half-peak during the rising phase, TD: the duration between SEP half-peak during the rising and declining phases. Kahler (2005) and Kahler (2013) revealed that TR and TD were positively correlated with CME speed, and interpreted that fast CME continued to drive the shock wave and injected SEPs for a long time. They also revealed that TO was related to CME speed and peak proton flux, but no correlation with the acceleration of CME was found. Pan et al. (2011) estimated the speed and the width of CMEs more accurately using the ice-cream cone model, a 3D reconstruction model of CME, and showed that they correlate with TR and TD, supporting the claim of Kahler (2005). TO is particularly challenging to understand, as we know of some events with short TO from likely far side regions that are almost certainly ill-connected (e.g., Cliver et al., 2005; Gómez-Herrero et al., 2015; Kahler, 2016). TO, as determined by first-arriving particles, may contain more information on acceleration processes close to the Sun than TR and TD, which may be more susceptible to transport processes.

In a recent statistical study of the association of fast CMEs with SEP events mostly during solar cycle 24 described in Chapter 2 (Kihara et al., 2020), the three timescales were

measured and compared with the source locations and CME speeds. In particular, TO was found to be short if the source region was within 60° in longitude from the footpoint of the Parker spiral (median: 86 minutes but 308 minutes in other longitudinal ranges), and negatively correlated with the CME speed for better connected events. But the scatter was quite large even for events with small longitudinal separations from the footpoint of the Parker spiral.

There are previous studies investigating the timing or height of acceleration and release of SEPs without using the timescales described above. Classically, by assuming an appropriate value for the length of the Parker spiral, the particle release time can be calculated. The path length of the Parker spiral corresponding to a typical solar wind speed of 400 km s^{-1} is about 1.2 AU. As a more practical method, there is a method called Velocity Dispersion Analysis (VDA). Assuming that particles with different energies (i.e., different relativistic velocities) are simultaneously released from the acceleration site and reach the observation instrument without being scattered in interplanetary space, the particle release time at the Sun and the path length can be calculated from the difference in the onset of each energy channel of the instrument. In gradual SEP events, it has been reported that the particle release times obtained by VDA are after gamma-ray peak (Tylka et al., 2003) and after the onset of type II emission (30 cases of GLE: mean 13.3 min, median 9.4 min, maximum 43 min; Reames, 2009a). Gopalswamy et al. (2012) calculated particle release times for 16 cases of GLE events assuming a path length of 1.2 AU and reported that delays from metric type II radio bursts were mean 17.2 min, median 15 min, maximum 44 min. In addition, compared with results by Reames (2009a) which used VDA, the particle release times independently calculated from two methods (VDA and fixed path length) had very small errors (within 5 min) in many cases (10/13). Vainio et al. (2013) performed VDA on 115 SEP events, and revealed that the path lengths were distributed around 1.4 AU; on the other hand, the Parker spiral length calculated from the solar wind speed did not generally exceed 1.2 AU. There was a discrepancy between the path length obtained from VDA and the Parker spiral length. Although similar results have been reported in several studies (e.g., Krucker & Lin, 2000; Kouloumvakos et al., 2015), several simulation results suggest that scattering in interplanetary space can increase the path length (Lintunen & Vainio, 2004; Rouillard et al., 2012).

At what height the particles are released can be estimated from the observation of where the leading edge of the CME is at the particle release time. It was Kahler (1994) who first linked the two. At the particle release time calculated with a path length of 1.3 AU, the height of the CME interpolated/extrapolated from the LASCO FOV assuming constant velocity was 2.5 – 4 $R_\odot$. Huttunen-Heikinmaa et al. (2005) calculated the released heights from proton and He observations and reported them as 2 – 10 $R_\odot$. Reames (2009a,b) performed VDA on GLE events and showed that the heights of CMEs at particle release times

are located at 2 – 6 $R_\odot$ and increase as the difference between the source longitude and the foot of the magnetic field line connected to the Earth increases. Similar longitudinal dependency of released height has been reported by Gopalswamy et al. (2012) as a difference between well-connected (W20 – W90) SEP events (mean 3.09 $R_\odot$, range: 1.71 – 4.09 $R_\odot$) and poorly connected events (mean 5.18 $R_\odot$, range: 2.75 – 8.49 $R_\odot$). However, the analysis of 44 SEP events by Kouloumvakos et al. (2015) showed no longitudinal dependency, although the peak SEP height was 3 – 4 $R_\odot$ and the maximum SEP height was 8 $R_\odot$. Thus, the timing and height of particle release have been studied in various ways but a unified understanding has not yet been made. They are directly related to TO and more knowledge is needed to understand the overall timescales of SEPs.

In this chapter, we further investigate two events from Table 2.2 that apparently had different TO, despite their similar source locations in the western hemisphere and similar CME speeds of $\sim$1200 km s^{-1}. We explore the possibility that the event with longer TO may reflect a slow growth of the CME-driven shock wave that becomes strong enough for particle acceleration only at later times. Combining CME height-time profiles with radio dynamic spectra that contain type II radio bursts, we follow the temporal evolution of the Alfvén Mach number of the shock wave with time above the two active regions without conducting advanced modeling. In Section 3.2, we describe the event selection and give an overview of the two events. We revisit in Section 3.3 the SEP timescales that are used for the subsequent analysis. In Section 3.4, we study how the shock waves develop in the two events in relation to TO or the SEP release times. In addition we study other factors that may affect these times. We summarize our findings in Section 3.5.

3.2 Observations

3.2.1 Event Selection

Chapter 2 (Kihara et al., 2020) conducted a statistical study of energetic CMEs that occurred between December 2006 and October 2017 in terms of their associations with SEP events. We also studied the timescales of the associated SEP events with respect to the speeds and source locations of the CMEs as shown in Table 2.2. Those analyses based on data from the Energetic Particle Sensor (Onsager et al., 1996) on the Geostationary Operations Environmental Satellite (GOES), and the High-Energy Telescope (HET; von Rosenvinge et al., 2008) and the Low-Energy Telescope (LET; Mewaldt et al., 2008), which belong to the suite of instruments for the In Situ Measurements of Particles and CME Transients (IMPACT; Luhmann et al., 2008) on the Solar-Terrestrial Relations Observatory (STEREO; Kaiser et al., 2008). The SEP events were identified when the >10 MeV proton flux exceeded 1 particle flux unit (pfu; defined as particles s^{-1} sr^{-1} cm^{-2}). The

CMEs responsible for the SEP events and the associated flares were found in white-light coronagraph and EUV low-coronal images produced by the instruments on the Solar and Heliospheric Observatory (SOHO; Domingo et al., 1995), Solar Dynamics Observatory (SDO; Pesnell et al., 2012), and STEREO. As expected, Kihara et al. (2020) found that SEP events that occurred in regions not far from the magnetic footpoints of the observer tend to have shorter timescales (in both TO and TR, see Figure 6 of the paper). However, TO mostly (77/82) ranges from 0.5 to 4 hours even when the longitudinal separation of the region from the Parker spiral footpoint is less than 60°. TO also appears to depend on the speed of the associated CME.

Table 3.1: Basic Parameters of the Two SEP Events

ID	CME				type II radio burst[e]		SEP event	
	launch[a] date and time	speed[b] (km s^{-1})	width[c] (deg)	source[d] location	frequency (MHz)	time	I_p[f] (pfu)	TO[g] (min)
Event 1	2014-04-18 12:43	1203	360	S20W34	60	12:55	58.5	62
Event 2	2017-07-14 01:12	1200	360	S06W29	14	01:20	13.6	158

[a] The launch time of CME calculated by extrapolating the height-time relations from the LASCO C2 and C3 data to the solar surface. Cited from the LASCO CME catalog.
[b] The linear speed obtained by fitting whole data points in LASCO C2 and C3. Cited from the LASCO CME catalog.
[c] The width in the plane of the sky of CME measured in LASCO C2 FOV. Cited from the LASCO CME catalog.
[d] The location of associated flare analyzed in Chapter 2.
[e] Frequency and time at the onset of the associated type II radio burst in each event.
[f] The peak proton flux with energies above 10 MeV observed by GOES satellite. Defined in Table 2.2.
[g] The >10 MeV proton onset time with respect to the launch of the CME. Defined in Table 2.2.

We selected two events that have widely different TO (i.e., 62 and 158 minutes) even though they came from regions in similar longitudes and were associated with halo CMEs with similar speeds. They occurred on 2014 April 18 and 2017 July 14. We hereafter refer to these SEP events as Event 1 and Event 2, respectively. Their basic parameters are shown in Table 3.1. The primary purpose of this chapter is to explain this wide difference in TO. We also revise the SEP onset times in Section 3.3, which we will use in the subsequent analyses.

3.2.2 Overview of the Events

In Figure 3.1 we plot the soft X-ray (SXR) and SEP (proton) time profiles of the two events over two-day intervals. The flare associated with Event 1 (in panel (a)) is M7.3 in the GOES classification (the peak 1 – 8 Å flux of 7.3×10^{-5} W m^{-2}), whereas the one associated with Event 2 (in panel (c)) is M2.4. The latter flare is of much longer duration, staying above the pre-event level in the GOES 1 – 8 Å channel for more than two days. Both flares are associated with halo CMEs, whose mean linear speed is ∼1200 km s^{-1}

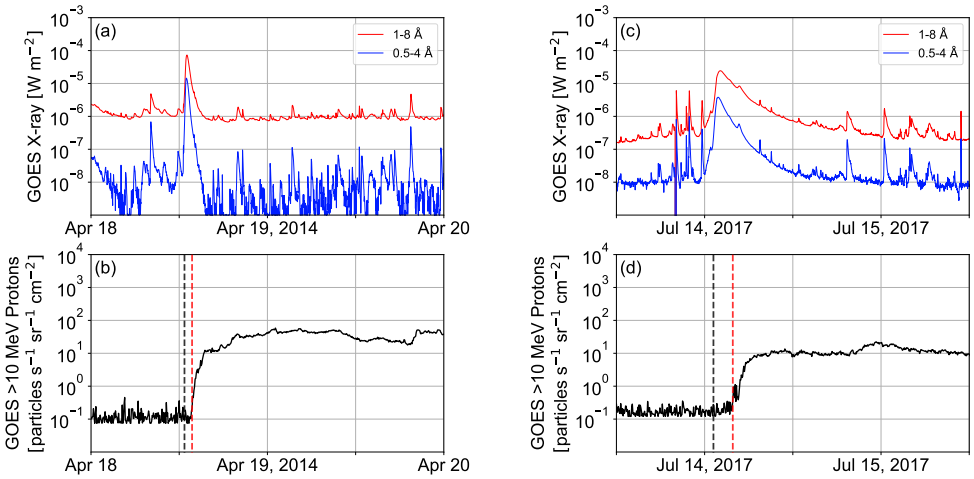

Figure 3.1: The soft X-ray (SXR) and the integrated flux of >10 MeV protons observed by GOES satellite for Event 1 ((a) and (b)) and for Event 2 ((c) and (d)). In panels (a) and (c), red and blue lines correspond to 1-8 Å and 0.5-4 Å. In panels (b) and (d), the launch time of CME and the time of proton onset are indicated by the black and red dashed lines, respectively.

across the combined FOV of the C2 and C3 telescopes of the Large Angle Spectrometric Coronagraph (LASCO; Brueckner et al., 1995) on board SOHO. The CME launch times in black dashed lines are calculated by extrapolating the height-time relations from the LASCO C2 and C3 data to the unit height (1 solar radius $R_\odot$), i.e. the solar surface.

Both Event 1 and Event 2 are accompanied by type II radio bursts, while their appearances are quite different as found in Figure 3.2, where we show radio dynamic spectra between 180 MHz and 0.1 MHz that consist of data from ground-based observatories and the Radio and Plasma Wave Experiment (WAVES; Bougeret et al., 1995) on the Wind spacecraft. In Event 1 (Figure 3.2(a)), the type II radio burst started at 12:55 UT from about 60 MHz (fundamental), which is 12 minutes after the CME launch (12:43 UT) and 8 minutes before the SXR peak (13:03 UT). It is preceded by strong type III radio bursts during the flare impulsive phase.

In Event 2 (Figure 3.2(b)), the type II radio burst is weak and intermittent and seen only in Wind/WAVES data below 14 MHz. It started at 01:20 UT, which is 12 minutes after the CME launch (01:12 UT) and 49 minutes before the SXR peak (02:09 UT). Type III radio bursts are also weak in Event 2, mostly at frequencies below the type II radio burst, sometimes categorized as shock-accelerated events (Cane et al., 1981). Although type II radio bursts are widely considered to signify shock waves, accelerating $\lesssim$10 keV electrons,

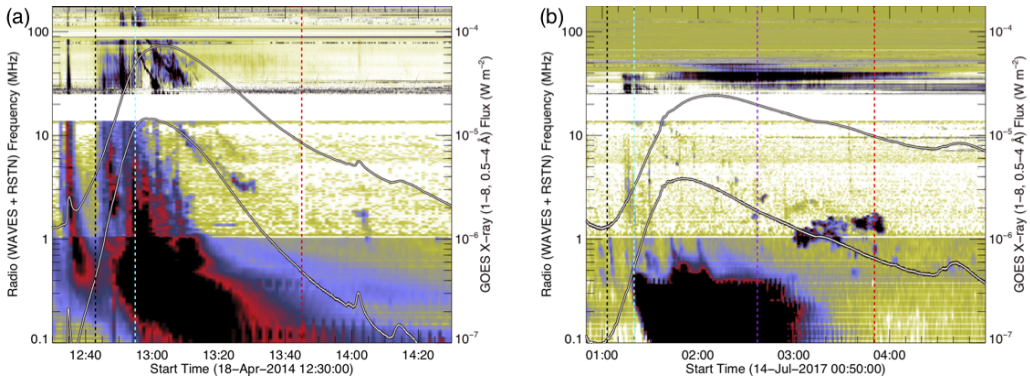

Figure 3.2: Radio dynamic spectra of the two events in the combined metric and DH ranges. The latter data are obtained with the Wind/WAVES instrument, and the metric data obtained at (a) RSTN/San Vito for Event 1 and (b) Culgoora Observatories for Event 2, respectively. The black (red) dashed lines indicate the CME launch times (the onset times of >10 MeV protons as observed by GOES), which replicate those in Figure 3.1. The cyan dashed lines indicate the start times of the type II radio bursts. The purple line in (b) indicates a proton onset time from SOHO/ERNE (see Section 3.3).

the proton onset is delayed in Event 2 much more than expected of ∼10 MeV protons, as reflected in larger TO. Lastly, note strong emissions starting around 03:00 UT in Figure 3.2(b). They do not follow the frequency drift of the type II radio burst. These features may indicate an interaction of the CME in Event 2 with a previously-launched CME (Gopalswamy et al., 2002). In Section 3.4.2 we will briefly discuss the possible effect of this CME-CME interaction on the observed SEPs in Event 2.

Spatially-resolved coronal observations of the two events are given in Figure 3.3, where panels (a) – (d) and (e) – (h) cover Event 1 and Event 2, respectively. Low coronal images (panels (a), (b), (e), and (f)) come from 211 Å channel of the Atmospheric Imaging Assembly (AIA; Lemen et al., 2012) on board SDO. The remaining panels consist of coronagraph images that come from LASCO. The origins of the eruptions – NOAA AR 12036 at S17W35 for Event 1 and NOAA AR 12665 at S06W29 for Event 2 – are contained in the yellow boxes in Figures 3.3(a) and 3.3(d), in which we note coronal dimmings in pre-event subtracted images (Figures 3.3(b) and 3.3(f)). Both events are associated with a halo CME, although asymmetric, as seen in Figures 3.3(d) and 3.3(h).

Figures 3.3(c) and 3.3(g) show the first available LASCO C2 images of the CMEs in the two events. It appears that we miss an early development of the CME in Event 1 due to the data gap of ∼40 minute preceding the image in Figure 3.3(c). The CME in Event 2 was preceded by a narrower CME, which was associated with a C3.0 flare from AR 12667 around N12W71. This region, indicated by a green arrow in Figure 3.3(e), produced C2.0, C5.9, and C3.0 flares starting, respectively, at 21:27, 21:46, and 23:30 UT on July 13.

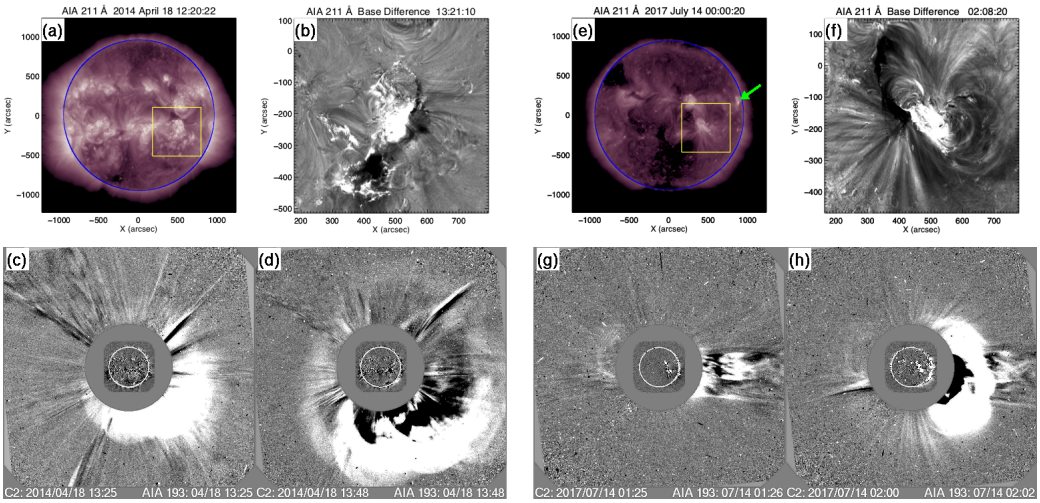

Figure 3.3: Low coronal and coronagraph images for Event 1 ((a) – (d)) and Event 2 ((e) – (h)). (a) and (e): AIA 211 Å images prior to the eruptions that led to the CMEs. The active regions that hosted the eruptions are included in the yellow boxes, in which coronal dimmings are noted in difference images with the pre-eruption image subtracted ((b) and (f)). (c) and (g): first available LASCO images of the CMEs in Event 1 and Event 2. (d) and (h): later LASCO images. The green arrow in (e) points to AR 12667, which produced narrower and slower CMEs than that in Event 2.

All of them produced a slow and narrow CME, and an electron event across the 10 keV – 2 MeV range but not a proton event. When protons increased in Event 2, the electron background was still elevated due to the electron event associated with the C3.0 flare, so it is not clear whether Event 2 produced an electron event. In contrast, Event 1 was accompanied by a strong electron event well above the elevated background in Event 2. The CME in Event 2 apparently caught up with the narrow CME and possibly resulted in a CME-CME interaction suggested in Figure 3.3(h). However, this is an hour earlier than the CME-CME interaction indicated in radio data (Figure 3.2(b)).

3.3 Further Analysis of SEP Events

Here, we re-evaluate TO of the two events. The GOES energetic particle data suffer from high background, which may prevent the SEP onset from being properly captured if the particle flux rises slowly from a low level. Another problem may be a possibly inadequate energy discrimination because the detector is only passively shielded (Posner, 2007; Kühl & Heber, 2019). These issues drive us to study similar data from other instruments. Here we analyze data from the High Energy Detector (HED) of the Energetic and Relativistic Nuclei and Electron (ERNE; Torsti et al., 1995) on board SOHO, which measures protons

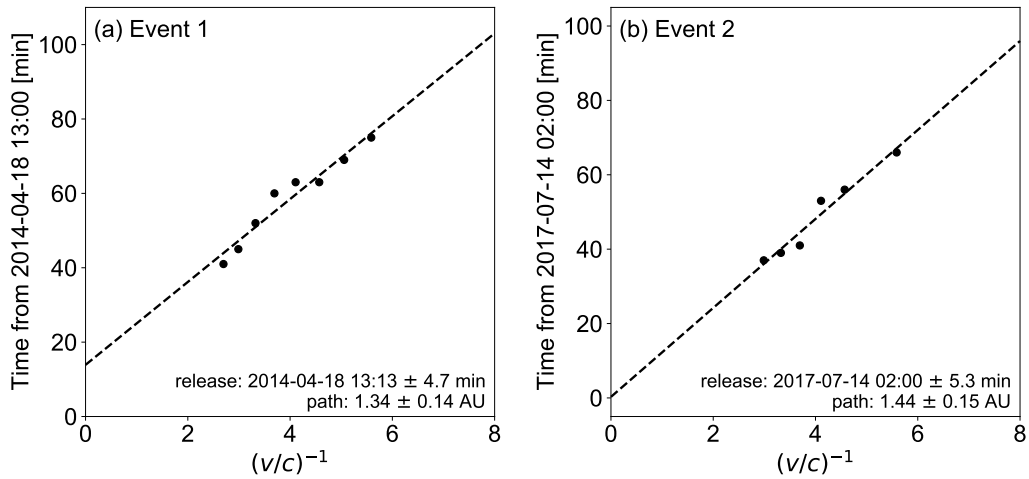

Figure 3.4: VDA analysis based on ERNE/HED data. The observed onset times are plotted against the inverse velocities $(v/c)^{-1}$ calculated from the effective energies of the individual channels. The vertical axis is the elapsed time since (a) 2014 Apr 18 13:00 and (b) 2017 July 14 2:00, respectively.

in the energy range of 13 – 130 MeV divided into 10 channels and has much lower background. In Event 1, protons were detected above the background up to the 64 – 80 MeV channel, where the onset time is found to be the same ($\pm$5 minutes) as that of the GOES $>$10 MeV integral channel; the onset time of the 13 – 16 MeV channel comes $\sim$30 minutes later. We keep the same TO that was calculated by Kihara et al. (2020) for Event 1, noting that it refers to the ERNE 64 – 80 MeV channel. In Event 2, on the other hand, the onset times of all the ERNE/HED channels that detected protons above the background (up to the 50 – 64 MeV channel) are much earlier than that of the GOES $>$10 MeV integral channel, suggestive of an effect of the high background of the latter. The "revised" onset time, coming from the 50 – 64 MeV channel of ERNE/HED, is used to redefine TO as indicated by the purple line in Figure 3.2(b). This gives TO=85 minutes (down from 158 minutes). The updated TO for Event 2 is still $\sim$25 minutes longer than TO for Event 1.

We also conduct the Velocity Dispersion Analysis (VDA), using all the ERNE/HED channels in which protons were detected above the background (up to the 64 – 80 MeV channel for Event 1 and the 50 – 64 MeV channel for Event 2). We plot the onset times (per visual inspection) against the inverse of speed $(v/c)^{-1}$, which corresponds to the effective energy of the channel (Figure 3.4). A least-square fit yields the proton release time of 2014 April 18 13:13 UT$\pm$4.7 minutes and 2017 July 14 02:00 UT$\pm$5.3 minutes for Event 1 and Event 2, respectively. The associated path lengths come out as 1.32$\pm$0.14 AU and 1.44$\pm$0.15 AU, which are somewhat longer than the lengths of the nominal Parker Spiral

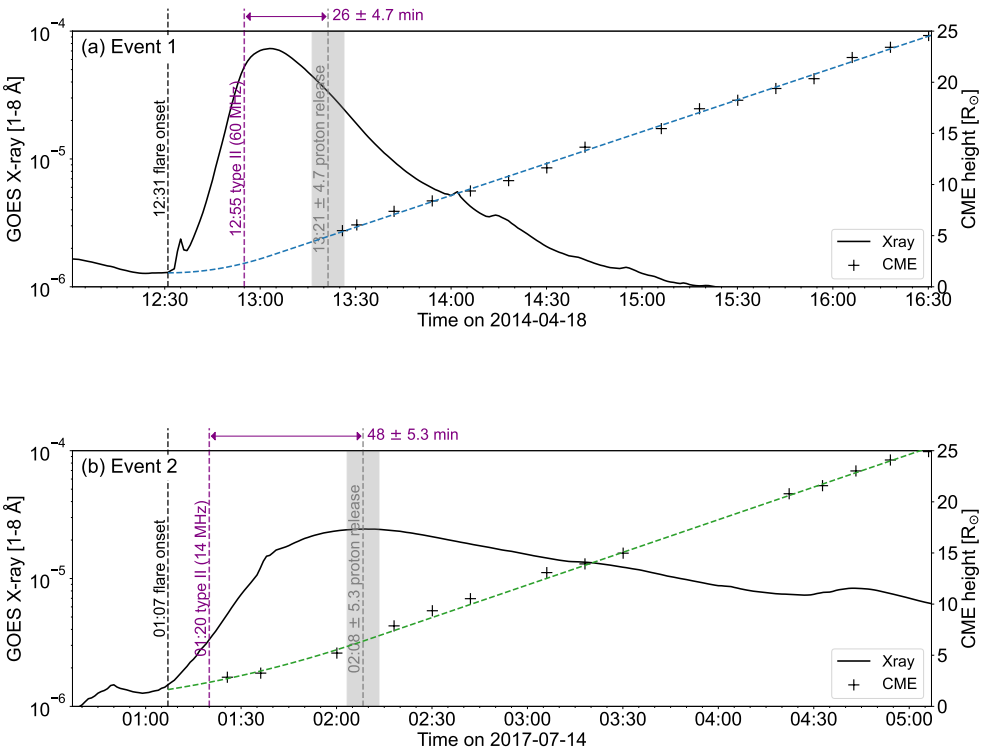

Figure 3.5: Summary of the timeline for (a) Event 1 and (b) Event 2. SXR (1 – 8Å) flux observed by the GOES satellite is shown as solid curves (black). The height of the leading edge of the CME is shown as crosses (measurements) and dashed curves (models). The vertical dashed lines in black and purple indicate the onset times of the flare and type II radio burst, respectively. The shaded areas in red indicates the proton release times with uncertainties (described in Section 3.3). The purple arrow indicates the interval between the type II onset and the estimated proton release from the VDA analysis.

for the observed solar wind speeds but within a range that suggests no major effect of scattering in the interplanetary space. Figure 3.5 shows the summary of the timeline of each event. We indicate the proton release times with 8.3 minutes added to account for the 1 AU travel time of light so that we can compare them with other electromagnetic-wave-based observations. From now on, instead of TO, we shall investigate the proton release time corrected for the 1 AU travel time of light, even though we originally aimed at explaining different TO. Moreover, we concern the proton release time with respect to the start time of the type II radio burst rather than the CME launch time. The proton release is delayed by 26±4.7 minutes for Event 1 and 48±5.3 minutes for Event 2. So the difference still exists between Event 1 and Event 2, although not as large as in the original TO.

Lastly, the multi-channel data from ERNE let us obtain fluence energy spectra of the two events. We integrate the background-subtracted proton flux in each channel while it is

above the background. The spectral fitting gives the power-law index of 3.65 for Event 1 and 4.18 for Event 2. These are close to the value of 3.83, that is the averaged indices of fluence spectra of well-connected SEP events reported by Gopalswamy et al. (2016). The slightly softer index in Event 2 may be an indication of a weaker shock, possibly related to a longer delay of the SEP onset time, but the difference may not be large enough to be conclusive.

3.4 Factors that may control the particle release time

As shown in Section 3.3, protons are not released immediately after the formation of the shock wave as manifested in type II radio bursts. However, the time difference is longer for Event 2. What is the reason for varying proton release times? In the following, we consider the evolution of the CME-driven shock wave, CME-CME interaction and properties of the active region that produces the CME.

3.4.1 Evolution of Shock Waves with Height

In this section, we investigate the possibility that particles (protons) are accelerated and released only when the shock wave becomes strong enough. Specifically, we study how the Alfvén Mach number (M_A) of the shock wave changes with time. The Alfvén Mach number is expressed as $M_A = (v_s - v_{sw})/v_A$, where v_s is the shock speed, v_{sw} is the solar wind speed, and v_A is the Alfvén speed.

For the shock speed, we could simply use the linear or quadratic fits to the height of the leading edge of the CME, as published in the CDAW LASCO CME catalog* (Yashiro et al., 2004). However, these fits are made on the height measurements in the whole (C2 and C3) FOV and may be too coarse to discuss the CME kinematics in the height range that likely corresponds to the SEP onset (e.g., below 10 $R_\odot$). Here we instead model the height-time profiles of CMEs such that they undergo constant acceleration from the onset to the peak of the SXR flux. This may be justified by the general tendency of CMEs to accelerate in the flare impulsive phase (e.g., Zhang et al., 2004; Temmer et al., 2010). We further assume that CMEs move with a constant speed in the LASCO FOV after the SXR peak. This modeled CME height-time profile is meant to better reproduce the behavior of the shock speed near the proton release time, and does not necessarily match the information from the CME catalog, including the estimated time of CME launch. The dashed curves in Figures 3.5(a) and 3.5(b) show the modeled CME height-time profiles of Event 1 (blue) and Event 2 (green), respectively. For each event the shock speed v_s is calculated using

*https://cdaw.gsfc.nasa.gov/CME_list/

the modeled CME height-time profile (Figure 3.6(a)). Even though the average speeds in the LASCO FOV are similar in both CMEs, their height-speed profiles are very different. The Event 1 CME (blue) accelerates quickly with a large acceleration of 627 m s^{-2} and reaches ∼1200 km s^{-1} before 3 $R_\odot$, while the Event 2 CME (green) accelerates slowly (188 m s^{-2}) and reaches ∼1300 km s^{-1} at 6.6 $R_\odot$.

The Alfvén speed, v_A, depends on the density and magnetic field, neither of which is directly observed, so we must rely on models. In order to address the inherently model-dependent nature of our attempt to calculate the Alfvén Mach number of the shock waves, we use the frequency drift of the type II radio burst to constrain the density profile with height. We choose the density model that places the shock wave of the type II radio burst at heights closest to the modeled CME heights at overlapping times. Consider the frequency (fundamental) of the type II radio burst to be the local plasma frequency, and we can get the density. For both events, the 3-fold (multiplied by 3) Saito model (Saito et al., 1977) yields the heights of the shock wave of the type II burst that best match the modeled CME heights. For the magnetic field, we consider the following three models:

$$B_1(r) = 2.2r^{-2} \tag{3.1}$$

$$B_2(r) = 6r^{-3} + 1.18r^{-2} \tag{3.2}$$

$$B_3(r) = 0.5(r-1)^{-1.5} \tag{3.3}$$

These are (1) the model assuming magnetic flux conservation (Mann et al., 1999), (2) the model based on measurement of Faraday rotation (Patzold et al., 1987), and (3) the empirical model by Dulk & McLean (1978). Three Alfvén speed profiles derived from these three magnetic field models (B_1, B_2, and B_3) are shown in the red solid ($v_{A,1}$), dash-dotted ($v_{A,2}$), and dotted lines ($v_{A,3}$) in Figure 3.6(a), respectively.

For the solar wind speed, v_{sw}, the model by Sheeley et al. (1997) has been widely used, but it starts only at 4.5 $R_\odot$. Recently, v_{sw} closer to the Sun (down to 1.53 $R_\odot$) has been obtained by Bemporad et al. (2021). We use the latter model up to the height of 5.07 $R_\odot$ (where v_{sw} from the former model becomes larger), and the former model at greater heights. The solar wind speed profile is shown as the black line in Figure 3.6(a).

We finally calculate three versions of M_A, based on the three magnetic field models B_1, B_2, and B_3 that were used to calculate v_A. Figure 3.6(b) shows the evolution of M_A with time for Event 1. The different types of lines for $M_{A,1}$, $M_{A,2}$, and $M_{A,3}$, distinguish the corresponding magnetic field models, B_1, B_2, and B_3. The vertical lines and the shaded area are identical to those in Figure 3.5. Figure 3.6(c) is the same as Figure 3.6(b) but for Event 2. Note that the reliability of the magnetic field models may be somewhat compromised near the solar surface. For example, the model of B_2 was originally calculated only in the range of 2 – 15 $R_\odot$. Accordingly, Figure 3.6 show the result only in >1.5 $R_\odot$.

Despite an apparent dependence of M_A on the assumed magnetic field models, we may understand the proton release times in relation to M_A. In both cases, all the three models of magnetic field yield M_A that increase toward the proton release times. Including errors, M_A reaches 1.6 – 2.6 for Event 1 and 2.0 – 3.0 for Event 2 during the estimated proton release time. Although it is beyond the scope of our work to discuss the critical Mach number (e.g., Bemporad & Mancuso, 2011; Rouillard et al., 2016), M_A in the above ranges may serve as thresholds, above which protons can be accelerated.

In Event 1, when the CME ceases to accelerate at ∼3 $R_\odot$ and ∼10 minutes after the onset of the type II radio burst, the shock speed already reaches ∼1200 km s^{-1}. However, the Alfvén Mach number remains low, because of the high Alfvén speed due to strong magnetic field at a low altitude. M_A reaches the critical value only ∼20 minutes after the CME stops accelerating as v_A decreases. In Event 2, on the other hand, the CME continues to accelerate for ∼50 minutes after the onset of the type II radio burst until it travels to the height of ∼6.6 $R_\odot$. During the acceleration phase, M_A only slowly increases, until it reaches the threshold as the CME attains the speed of ∼1200 km s^{-1}. This may explain why the proton release is delayed more in Event 2 than in Event 1. It also aligns with a longer duration of the flare in Event 2.

3.4.2 CME-CME Interaction

As an alternative explanation for a later particle release in Event 2, let us assume that the shock is in fact too weak for particle acceleration, irrespective of the analysis given in Section 3.4.1. Then what distinguishes Event 2 is the CME-CME interaction, which may compensate for the weak shock. It is proposed that when a fast CME catches up with a preceding CME, preconditioning by the preceding CME results in efficient particle acceleration (e.g., Gopalswamy et al., 2002; Li & Zank, 2005; Li et al., 2012). The calculated proton release time is around 02:00 UT (Section 3.3), which is close to the time the CME in Event 2 caught up with the preceding narrow CME associated with a C3.0 flare in AR 12667 (Figure 3.3(h)). Note that the radio signatures that may indicate a CME-CME interaction starts only around 03:00 UT (Figure 3.2(b)). However, it is not clearly understood at which timing during a CME-CME interaction such signatures appear in radio spectra.

The possibility that Event 2 originally produced a weak shock wave with poor acceleration efficiency may be supported by the bandwidth of the type II radio burst. Iwai et al. (2020) reported a positive correlation between the bandwidth of the type II radio burst and the peak proton flux, and proposed that the bandwidth represents the strength of the shock wave. In our examples, the time-averaged bandwidth for Event 1 was $>$ 1000 kHz, wider than that for Event 2 ($<$ 500 kHz), suggesting that the shock wave in Event 2 was weaker.

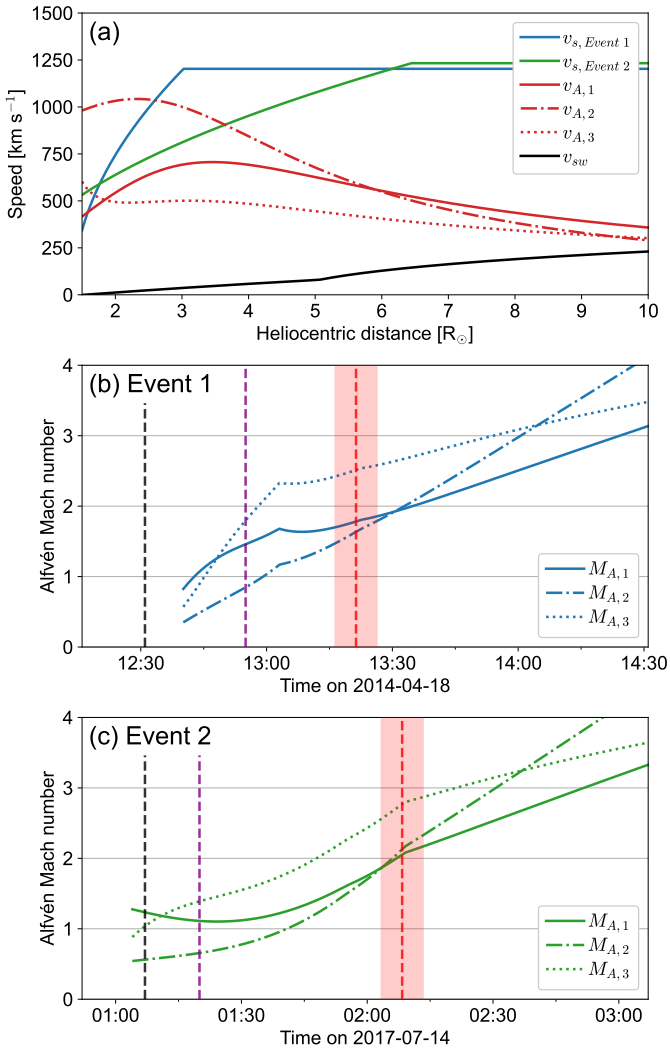

Figure 3.6: (a): Shock speed for Event 1 (blue, solid) and Event 2 (green, solid) calculated from the modeled height-time profiles. The red lines represent the Alfvén speeds based on the three models of magnetic field. v_{sw} is shown as the black solid line. (b) and (c): M_A for Event 1 and Event 2, respectively, calculated with all the information presented in (a). As in Figure 3.5, the dashed lines in black and purple indicate the onset times of the flare and type II radio burst, respectively, and the shaded areas in red the proton release times with uncertainties.

3.4.3 Properties of the Active Regions

We discuss how different proton release times may be traced back to the properties of the active regions that produced the CMEs. Figure 3.7 shows Hα images and magnetograms of the active regions that produced the two events (AR 12036 and AR 12665). For each of the regions, the top three rows display Hα images taken at three times (before and around the flare peak and during the decay phase) that are indicated by black dashed lines on the GOES 1 – 8 Å light curves in the bottom panels. The fourth row gives a line-of-sight magnetogram from the Helioseismic and Magnetic Imager (HMI; Scherrer et al., 2012) on board SDO, taken in the early phase of the flare (see the black solid line in the bottom row). The Hα data come from the Global Oscillation Network Group (GONG*; Harvey et al., 1996) for Event 1 and the Solar Dynamics Doppler Imager (SDDI; Ichimoto et al., 2017) installed on the Solar Magnetic Activity Research Telescope (SMART; Ueno et al., 2004) at Hida Observatory.

We readily note from the magnetograms that the region for Event 1 is more magnetically complex than the one for Event 2, which is dominated by essentially a simple bipolar topology. This difference is also noted in the pre-flare Hα images (the top row of Figure 3.7). The complex magnetic field configuration of the region for Event 1 may be reflected also in the complex evolution of the flare ribbons in Hα images as shown in the second and third rows of Figure 3.7. However, the apparent difference of the complexity of the two regions may not be reflected in basic magnetic parameters from the Space-Weather HMI Active Region Patches (SHARP; Bobra et al., 2014) over several (e.g., 6 hour, 12 hour, 24 hour) intervals preceding the flare onsets. None of them seem to distinguish the two regions in a significant way.

Flare ribbons contain additional information of flares. Concerning our examples, the initial distance of the flare ribbons for Event 1 is shorter ($\sim$20 Mm) than that for Event 2 ($\sim$50 Mm). This is consistent with the result that those with widely separated ribbons in the beginning tend to be of long duration (Toriumi et al., 2017). Accordingly, the flare loops are longer in the region for Event 2 than in the region for Event 1, which may translate to a higher initial reconnection point in Event 2. The magnetic field strength near the reconnection point is, therefore, expected to be weaker in Event 2, suggesting that it could not drive the faster ejection near the solar surface.

Another information we can get from the area of flare ribbons is the reconnection flux, which may be related to the photospheric magnetic flux traversed by the flare ribbons (e.g., Forbes & Priest, 1984; Kazachenko et al., 2017). Analyzing the flare ribbons in AIA 1600 Å images, Kazachenko et al. (2017) created a database of the reconnected flux of 3137 $\gtrsim$C1 flares up to April 2016. The reconnection flux of the flare for Event 1 is

*https://gong.nso.edu

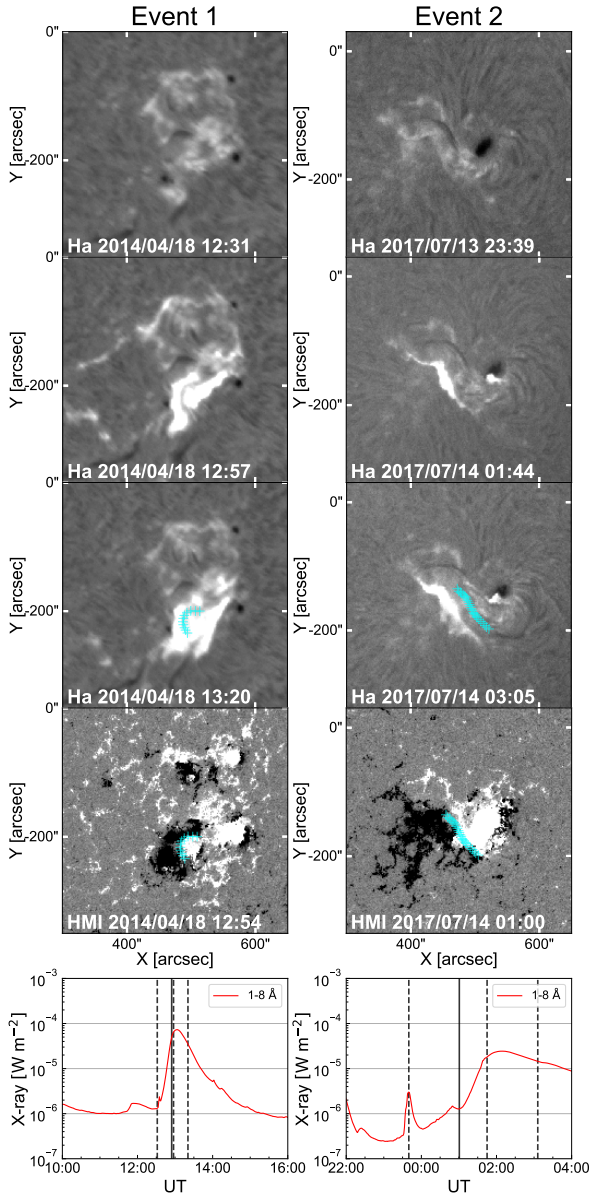

Figure 3.7: The observations of the solar surface at each event. The top three panels are Hα ground-based observations, and the bottom is HMI line-of-sight magnetogram. The bottom panel is a $1-8$Å light curve of SXR, and the black dashed and solid lines correspond to the observation times of Hα and the magnetic field, respectively. The cyan cross markers indicate the location of the top of the post-flare loop with reference to the flare ribbon and polarity inversion line.

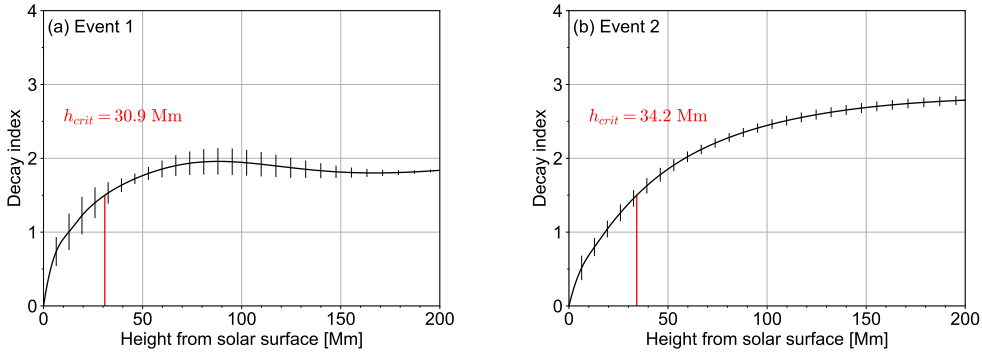

Figure 3.8: The decay index vs height for the regions responsible for (a) Event 1 and (b) Event 2. The red line corresponds to the critical height at which the decay index becomes 1.5. The error bars show the standard deviation at each height.

9.44×10^{21}Mx, according to the database. A new calculation shows that for Event 2 to be 2.92×10^{21}Mx (M. Kazachenko, 2021, private communication). However, the reconnection rate normalized by the duration of the flare is 3.21×10^{18} Mx s^{-1} in Event 1 and 3.53×10^{17} Mx s^{-1} in Event 2, which is smaller by one order of magnitude.

Lastly, to address the possible difference of the overlying magnetic structure in the regions responsible for Event 1 and Event 2, we calculate the decay index, $n = -d\ln B/d\ln h$, which shows how quickly the magnetic field weakens with height over the polarity inversion lines that align with the tops of the post-flare loops (cyan marks in the third and fourth rows of Figure 3.7). The PFSS model* is used to calculate the coronal magnetic field. The bottom boundary is the downsized (720×360 pixels) standard HMI Carrington synoptic map, embedded with the original HMI magnetogram of an area of $(200'')^2$ around the core of the active region, which is taken just before the flare. The decay index gives a criterion for torus instability to trigger an eruption (Kliem & Török, 2006). In Figure 3.8, the decay index over the height up to 200 Mm is shown for the two regions. We find almost no difference in the so-called critical height (h_{crit}) at which n_{crit}=1.5.

However, the decay index above 50 Mm tends to be larger in the region for Event 2, meaning the magnetic field decreases more quickly with height. Indeed, $|B_r|$ at the source surface of 2.5 $R_\odot$, which is the upper boundary of the calculation domain, is smaller in Event 2 region than that in Event 1 region. We note that even the value in Event 1 is smaller than calculated with any of the magnetic field models that are used in Section 3.4.1. A similar finding was reported for example by Rouillard et al. (2016), consistent with the smaller open flux at 1 AU as predicted with photospheric magnetograms than actually

*https://github.com/dstansby/pfsspy/ developed by Stansby et al. (2020)

observed (e.g., Linker et al., 2017).

3.5 Summary

In this chapter, we choose two events that had widely different TO, the time of the SEP onset (found in GOES >10 MeV proton data) from the onset of the CME, although they occurred at similar longitudes and were associated with CMEs that had similar speeds (Kihara et al., 2020). After reviewing SOHO/ERNE data, we decided to use these data with much lower background and better energy discrimination. The revised TO, or particle (proton) release time (as obtained with a VDA) from the onset of the type II radio burst, shows a smaller difference between the two events. However, the difference of 20 – 25 minutes is still significant, unaccounted for by different path lengths (1.34 AU vs 1.44 AU, see Figure 3.4) from the VDA.

In order to understand the longer delay of the proton release time in Event 2, we focus on how the shock wave grows close to the Sun as characterized by the Alfvén Mach number M_A of the shock waves, by more closely examining the height-time profiles of the CMEs than single fits over the entire FOV covered by LASCO data. Despite strong model dependency of the Alfvén speed v_A especially on the magnetic field, M_A keeps rising and reaches certain thresholds around the proton release times. It has been shown with more sophisticated tools (e.g., Rouillard et al., 2016; Kouloumvakos et al., 2019) that protons are released when M_A reaches a critical value. We note that slow acceleration of the CME over long time while the soft X-ray flux was on the rise is a key to the delayed acceleration/release of protons in Event 2.

Another possibility is that the shock wave driven by the CME in Event 2 was intrinsically weak, as suggested by small bandwidths of the type II radio burst (cf., Iwai et al., 2020), not being capable of accelerating protons on its own, but that interaction with the previous CME may have been instrumental in the production of energetic protons (e.g., Gopalswamy et al., 2002; Li & Zank, 2005; Li et al., 2012). The timing of the possible CME-CME interaction is consistent with the proton release as far as LASCO imagery is concerned, but radio signatures come an hour later. This may not be a problem until we better understand at what timing during CME-CME interactions we expect to observe the radio signatures.

In either case, we try to find different properties of the active regions that hosted the CMEs. The region for Event 2 had much simpler magnetic field configurations, consistent with the way flare ribbons developed. The eruption involved a larger volume, producing a flare that lasted for more than a day. Even though it is not straightforward to extract the possible differences of active regions in the forms of the routinely calculated magnetic field prop-

erties with HMI data (SHARP; Bobra et al., 2014), reconnection flux from flare ribbons (Kazachenko et al., 2017), or the decay index (Kliem & Török, 2006), the overall simple magnetic configurations allowed slow but steady acceleration of the CME in Event 2. They should also be conducive to the long-duration flare. Although the energy release was not intense at first, the injection of magnetic energy lasted for a long time. Eventually a shock wave strong enough to generate SEPs was formed, or a CME fast enough to catch up with the former one was formed.

We close with a cautionary note that GOES EPS data may not be suitable for scientific analyses of onset times in particular for events like our Event 2, where protons increase slowly from a low level. The smaller difference in the proton release time as found using ERNE data may explain only marginal differences in active region properties. We suggest that the past and ongoing results based on GOES EPS data should be calibrated with other data.

CHAPTER 4

Concluding Remarks

4.1 Conclusion

The aim of this thesis is to clarify the relationship between gradual SEP events and CMEs, especially how CMEs affect the timescales of SEPs. Associated SEP events were extracted starting from CMEs, and statistical analysis and detailed analysis focusing on individual events were performed. In this section, the current understanding of the three questions described in Section 1.2.4 is concluded based on the findings of the two studies.

Q1. How are SEPs associated with CMEs?

A1. With respect to 239 fast ($v_{CME} \geq 900$ km s^{-1}) and wide (angular width $\geq 60°$) CMEs with specified source location and an unbiased distribution, when CMEs are launched in the E20 – W100 range from the observer, the so-called well-connected longitude, the SEP association rate is high, up to over 50%. The SEP association rate is non-zero except when CMEs are launched in a small longitudinal range (E180 – E135), and almost all fast and wide CMEs have the potential to generate SEPs. In addition, CMEs exceeding ∼2000 km s^{-1} are almost certainly associated with SEP events.

It was confirmed that there is a positive correlation between CME speed and peak proton flux, which is well-known in previous studies (e.g., Kahler, 2001). Well-connected events have a larger variation in the peak proton flux of SEP events that can occur from CMEs of similar speeds than poorly connected events. This suggests that some important factors other than CME speeds and source longitudes determine the peak proton flux.

Q2. How are the timescales of SEPs related to the parameters of the CMEs?

A2. In Chapter 2, the following three timescales were investigated, TO: the SEP onset time with respect to the CME launch, TR: the rise time from the SEP onset time to

the SEP half-peak during the rising phase, TD: the duration between SEP half-peak during the rising and declining phases. In addition, $\Delta\Phi$ (the source longitude relative to the footpoint of the Parker spiral) was measured for each event and correlated with the three timescales. The results show that all timescales tend to become longer as $|\Delta\Phi|$ increased, but it is most remarkable in TO, is slightly weak in TR, and is further weak in TD. This supports the idea that the SEP onset time is determined by the first accelerated particles near the Sun and strongly reflects the situation of the acceleration site. There was a weak negative correlation between TO and the CME speed in well-connected events. Faster CMEs can drive stronger shock waves and can accelerate and release SEPs sooner, while the CME speed, which is a parameter that implies typical "shock wave strength", may not affect particles that are immediately accelerated to $>$10 MeV and released.

Q3. What are the factors that determine the timescales of SEPs with large variations between events, especially the SEP onset time (TO)?

A3. In Chapter 3, the SEP event with long TO even though they originated from the fast well-connected CME was investigated. Compared to the event with similar CME which has a typical short TO, it was characterized by relatively simple magnetic field configurations and a longer timescale of associated flares and radio bursts. In the event in question, the long TO was directly due to the long interval between the occurrence of the type II radio burst and the particle release time. One scenario to explain this observation could be that the growth of the shock wave, represented by Alfvén Mach Number M_A, was slow in that event. Since the process of energy release by the associated flare was gradual, the CME could be slowly accelerated. This result suggests that it took time for the shock wave to reach a certain threshold of M_A required to accelerate SEPs and that particles were released with a delay from the CME launch or the start of the type II radio burst.

4.2 Future Direction

One of the most important contributions of this thesis is the construction of the largest SEP event list including timescales. In Chapter 2, we focused on gradual SEP events, that is, the contribution of CMEs. In our event list, there are events with large solar flares and events with increases in electrons. Expanding the event list by examining not only the relationship between CMEs and protons, but also the relationship between solar flares and electrons and other ions, and also considering the possibility of impulsive SEP events, would allow validation of the flare contribution to the gradual SEP events recently claimed (e.g., Cane et al., 2010), and would limit the acceleration mechanism of SEPs. The analysis

presented in Chapter 3 is only one topic departing from the results of the statistical analysis of the event list, and thus possesses various directions of analysis. The results of the two events selected for the detailed analysis suggest a relationship between the timescales of flares, CMEs, and SEPs. This analysis is the first step in a comprehensive analysis of solar active phenomena, including solar flares and CMEs, with the aim of limiting the timescales of SEPs. The hypothesis obtained in this thesis should be verified and supported by further analysis of a larger set of events. It is also an interesting result that the relationship between the complexity of the active region and the timescales of SEPs has been suggested. It was proposed that the timescales of solar flares are correlated with the complexity of active regions (Toriumi et al., 2017). They suggest a unified understanding of the parameters of flares, CMEs, and SEPs, as well as active regions, or the existence of subgroups with common characteristics.

These implications are also of critical importance in the practical forecasting of SEPs. At present, real-time observations with short-time cadence are mainly available for Hα, EUV, and magnetogram observations of the full solar disk, for X-ray observations integrated over the solar disk, and for temporal data such as particles and magnetic fields around the Earth. Since the current coronagraph observations of CMEs are deficient in time cadence and real-time performance, particles can reach the Earth almost at the same time as the observation of CME at the earliest. In order to prevent radiation hazards, it is necessary to alert the possibility of the arrival of SEPs at an early stage of the event, that is, by making full use of information on the solar surface that can be currently observed.

In very recent years, the results of "in situ" observations of SEPs by the Parker Solar Probe (PSP; Fox et al., 2016) and the Solar Orbiter (SolO; Müller et al., 2020) have started to appear (e.g., McComas et al., 2019; Giacalone et al., 2020; Hill et al., 2020; Mitchell et al., 2020; Leske et al., 2020; Joyce et al., 2020; Schwadron et al., 2020; Wiedenbeck et al., 2020; Kouloumvakos et al., 2020; Chhiber et al., 2021; Mason et al., 2021a; Gómez-Herrero et al., 2021; Wimmer-Schweingruber et al., 2021; Bučík et al., 2021, 2023) and the results of simultaneous observations in the inner heliosphere and 1 AU started to be obtained (e.g., Lario et al., 2021; Mason et al., 2021b; Mitchell et al., 2021; Cohen et al., 2021a; Kollhoff et al., 2021; Lario et al., 2022). In addition, further event-to-event variations are also being found (e.g., Cohen et al., 2021b). Although it is not yet possible to capture the moment of particle release in situ, the observation at the midpoint between the acceleration region and 1 AU makes the timescale measurements of SEPs more robust. These observations will provide important clues to verify the particle release process and mechanism obtained so far and to understand the possibility of scattering in interplanetary space, which has not been addressed in this thesis.

Bibliography

Al-Omari, M., Qahwaji, R., Colak, T., & Ipson, S. 2010, SoPh, 262, 511, doi: 10.1007/s11207-010-9516-5

Asai, A., Ishii, T. T., Isobe, H., et al. 2012, ApJL, 745, L18, doi: 10.1088/2041-8205/745/2/L18

Aschwanden, M. J. 2002, SSRv, 101, 1, doi: 10.1023/A:1019712124366

Athay, R. G., & Moreton, G. E. 1961, ApJ, 133, 935, doi: 10.1086/147098

Bemporad, A., Giordano, S., Zangrilli, L., & Frassati, F. 2021, A&A, 654, A58, doi: 10.1051/0004-6361/202141276

Bemporad, A., & Mancuso, S. 2011, ApJL, 739, L64, doi: 10.1088/2041-8205/739/2/L64

Benz, A. O. 2017, Living Reviews in Solar Physics, 14, 2, doi: 10.1007/s41116-016-0004-3

Bobra, M. G., Sun, X., Hoeksema, J. T., et al. 2014, SoPh, 289, 3549, doi: 10.1007/s11207-014-0529-3

Bougeret, J. L., Kaiser, M. L., Kellogg, P. J., et al. 1995, SSRv, 71, 231, doi: 10.1007/BF00751331

Brueckner, G. E., Howard, R. A., Koomen, M. J., et al. 1995, SoPh, 162, 357, doi: 10.1007/BF00733434

Burkepile, J. T., Hundhausen, A. J., Stanger, A. L., St. Cyr, O. C., & Seiden, J. A. 2004, Journal of Geophysical Research (Space Physics), 109, A03103, doi: 10.1029/2003JA010149

Bučík, R., Mason, G. M., Gómez-Herrero, R., et al. 2021, A&A, 656, L11, doi: 10.1051/0004-6361/202141009

—. 2023, A&A, 669, A13, doi: 10.1051/0004-6361/202245037

Cane, H. V., Erickson, W. C., & Prestage, N. P. 2002, Journal of Geophysical Research (Space Physics), 107, 1315, doi: 10.1029/2001JA000320

Cane, H. V., McGuire, R. E., & von Rosenvinge, T. T. 1986, ApJ, 301, 448, doi: 10.1086/163913

Cane, H. V., Reames, D. V., & von Rosenvinge, T. T. 1988, J. Geophys. Res., 93, 9555, doi: 10.1029/JA093iA09p09555

Cane, H. V., Richardson, I. G., & von Rosenvinge, T. T. 2010, Journal of Geophysical Research (Space Physics), 115, A08101, doi: 10.1029/2009JA014848

Cane, H. V., Stone, R. G., Fainberg, J., et al. 1981, Geophys. Res. Lett., 8, 1285, doi: 10.1029/GL008i012p01285

Carmichael, H. 1964, A Process for Flares, Vol. 50, 451

Carrington, R. C. 1859, MNRAS, 20, 13, doi: 10.1093/mnras/20.1.13

Chen, P. F., & Wu, Y. 2011, ApJL, 732, L20, doi: 10.1088/2041-8205/732/2/L20

Chhiber, R., Matthaeus, W. H., Cohen, C. M. S., et al. 2021, A&A, 650, A26, doi: 10.1051/0004-6361/202039816

Cliver, E. W. 1982, SoPh, 75, 341, doi: 10.1007/BF00153481

—. 2016, ApJ, 832, 128, doi: 10.3847/0004-637X/832/2/128

Cliver, E. W., Thompson, B. J., Lawrence, G. R., et al. 2005, in International Cosmic Ray Conference, Vol. 1, 29th International Cosmic Ray Conference (ICRC29), Volume 1, 121

Cohen, C. M. S., Christian, E. R., Cummings, A. C., et al. 2021a, A&A, 656, A29, doi: 10.1051/0004-6361/202140967

—. 2021b, A&A, 650, A23, doi: 10.1051/0004-6361/202039299

Delaboudinière, J. P., Artzner, G. E., Brunaud, J., et al. 1995, SoPh, 162, 291, doi: 10.1007/BF00733432

Desai, M., & Giacalone, J. 2016, Living Reviews in Solar Physics, 13, 3, doi: 10.1007/s41116-016-0002-5

Desai, M. I., Mason, G. M., Dwyer, J. R., et al. 2001, ApJL, 553, L89, doi: 10.1086/320503

Dierckxsens, M., Tziotziou, K., Dalla, S., et al. 2015, SoPh, 290, 841, doi: 10.1007/s11207-014-0641-4

Domingo, V., Fleck, B., & Poland, A. I. 1995, SoPh, 162, 1, doi: 10.1007/BF00733425

Dulk, G. A., & McLean, D. J. 1978, SoPh, 57, 279, doi: 10.1007/BF00160102

Fisher, G. H., Canfield, R. C., & McClymont, A. N. 1985, ApJ, 289, 414, doi: 10.1086/162901

Forbes, T. G., & Acton, L. W. 1996, ApJ, 459, 330, doi: 10.1086/176896

Forbes, T. G., & Priest, E. R. 1984, SoPh, 94, 315, doi: 10.1007/BF00151321

Forbush, S. E. 1946, Physical Review, 70, 771, doi: 10.1103/PhysRev.70.771

Fox, N. J., Velli, M. C., Bale, S. D., et al. 2016, SSRv, 204, 7, doi: 10.1007/s11214-015-0211-6

Giacalone, J., Mitchell, D. G., Allen, R. C., et al. 2020, ApJS, 246, 29, doi: 10.3847/1538-4365/ab5221

Ginzburg, V. L., & Zhelezniakov, V. V. 1958, Soviet Ast., 2, 653

Giovanelli, R. G. 1946, Nature, 158, 81, doi: 10.1038/158081a0

Gómez-Herrero, R., Dresing, N., Klassen, A., et al. 2015, ApJ, 799, 55, doi: 10.1088/0004-637X/799/1/55

Gómez-Herrero, R., Pacheco, D., Kollhoff, A., et al. 2021, A&A, 656, L3, doi: 10.1051/0004-6361/202039883

Gopalswamy, N. 2010, in Solar and Stellar Variability: Impact on Earth and Planets, ed. A. G. Kosovichev, A. H. Andrei, & J.-P. Rozelot, Vol. 264, 326–335, doi: 10.1017/S1743921309992870

Gopalswamy, N., Mäkelä, P., & Yashiro, S. 2019, Sun and Geosphere, 14, 111, doi: 10.31401/SunGeo.2019.02.03

Gopalswamy, N., Xie, H., Akiyama, S., et al. 2013, ApJL, 765, L30, doi: 10.1088/2041-8205/765/2/L30

Gopalswamy, N., Xie, H., Yashiro, S., et al. 2012, SSRv, 171, 23, doi: 10.1007/s11214-012-9890-4

Gopalswamy, N., Yashiro, S., Krucker, S., Stenborg, G., & Howard, R. A. 2004, Journal of Geophysical Research (Space Physics), 109, A12105, doi: 10.1029/2004JA010602

Gopalswamy, N., Yashiro, S., Michałek, G., et al. 2002, ApJL, 572, L103, doi: 10.1086/341601

Gopalswamy, N., Yashiro, S., Michalek, G., et al. 2009, Earth Moon and Planets, 104, 295, doi: 10.1007/s11038-008-9282-7

Gopalswamy, N., Yashiro, S., Thakur, N., et al. 2016, ApJ, 833, 216, doi: 10.3847/1538-4357/833/2/216

Gosling, J. T. 1993, J. Geophys. Res., 98, 18937, doi: 10.1029/93JA01896

Gosling, J. T., Hildner, E., MacQueen, R. M., et al. 1974, J. Geophys. Res., 79, 4581, doi: 10.1029/JA079i031p04581

Gosling, J. T., McComas, D. J., Phillips, J. L., & Bame, S. J. 1991, J. Geophys. Res., 96, 7831, doi: 10.1029/91JA00316

Grechnev, V. V., Kiselev, V. I., Meshalkina, N. S., & Chertok, I. M. 2015, SoPh, 290, 2827, doi: 10.1007/s11207-015-0797-6

Guo, J., Dumbović, M., Wimmer-Schweingruber, R. F., et al. 2018, Space Weather, 16, 1156, doi: 10.1029/2018SW001973

Harvey, J. W., Hill, F., Hubbard, R. P., et al. 1996, Science, 272, 1284, doi: 10.1126/science.272.5266.1284

Hill, M. E., Mitchell, D. G., Allen, R. C., et al. 2020, ApJS, 246, 65, doi: 10.3847/1538-4365/ab643d

Hirayama, T. 1974, SoPh, 34, 323, doi: 10.1007/BF00153671

Hodgson, R. 1859, MNRAS, 20, 15, doi: 10.1093/mnras/20.1.15

Howard, R. A., Michels, D. J., Sheeley, N. R., J., & Koomen, M. J. 1982, ApJL, 263, L101, doi: 10.1086/183932

Howard, R. A., Sheeley, N. R., J., Michels, D. J., & Koomen, M. J. 1985, J. Geophys. Res., 90, 8173, doi: 10.1029/JA090iA09p08173

Howard, R. A., Moses, J. D., Vourlidas, A., et al. 2008, SSRv, 136, 67, doi: 10.1007/s11214-008-9341-4

Hoyle, F. 1949, Some recent researches in solar physics.

Hudson, H. S., & Cliver, E. W. 2001, J. Geophys. Res., 106, 25199, doi: 10.1029/2000JA904026

Hundhausen, A. J. 1993, J. Geophys. Res., 98, 13177, doi: 10.1029/93JA00157

Huttunen-Heikinmaa, K., Valtonen, E., & Laitinen, T. 2005, A&A, 442, 673, doi: 10.1051/0004-6361:20042620

Ichimoto, K., Ishii, T. T., Otsuji, K., et al. 2017, SoPh, 292, 63, doi: 10.1007/s11207-017-1082-7

Illing, R. M. E., & Hundhausen, A. J. 1985, J. Geophys. Res., 90, 275, doi: 10.1029/JA090iA01p00275

Iwai, K., Yashiro, S., Nitta, N. V., & Kubo, Y. 2020, ApJ, 888, 50, doi: 10.3847/1538-4357/ab57ff

Joyce, C. J., McComas, D. J., Christian, E. R., et al. 2020, ApJS, 246, 41, doi: 10.3847/1538-4365/ab5948

Kahler, S. 1994, ApJ, 428, 837, doi: 10.1086/174292

Kahler, S. W. 1982, J. Geophys. Res., 87, 3439, doi: 10.1029/JA087iA05p03439

—. 2001, J. Geophys. Res., 106, 20947, doi: 10.1029/2000JA002231

—. 2005, ApJ, 628, 1014, doi: 10.1086/431194

—. 2013, ApJ, 769, 110, doi: 10.1088/0004-637X/769/2/110

—. 2016, ApJ, 819, 105, doi: 10.3847/0004-637X/819/2/105

Kahler, S. W., Hildner, E., & Van Hollebeke, M. A. I. 1978, SoPh, 57, 429, doi: 10.1007/BF00160116

Kahler, S. W., Reames, D. V., & Sheeley, N. R., J. 2001, ApJ, 562, 558, doi: 10.1086/323847

Kahler, S. W., Sheeley, N. R., J., Howard, R. A., et al. 1984, J. Geophys. Res., 89, 9683, doi: 10.1029/JA089iA11p09683

Kahler, S. W., & Vourlidas, A. 2005, Journal of Geophysical Research (Space Physics), 110, A12S01, doi: 10.1029/2005JA011073

Kaiser, M. L., Kucera, T. A., Davila, J. M., et al. 2008, SSRv, 136, 5, doi: 10.1007/s11214-007-9277-0

Kallenrode, M. B. 2003, Journal of Physics G Nuclear Physics, 29, 965

Kane, S. R. 1974, in Coronal Disturbances, ed. G. A. Newkirk, Vol. 57, 105

Kazachenko, M. D., Lynch, B. J., Welsch, B. T., & Sun, X. 2017, ApJ, 845, 49, doi: 10.3847/1538-4357/aa7ed6

Khan, J. I., & Aurass, H. 2002, A&A, 383, 1018, doi: 10.1051/0004-6361:20011707

Khan, J. I., & Hudson, H. S. 2000, Geophys. Res. Lett., 27, 1083, doi: 10.1029/1999GL010730

Kihara, K., Asai, A., Yashiro, S., & Nitta, N. V. 2022, submitted

Kihara, K., Huang, Y., Nishimura, N., et al. 2020, ApJ, 900, 75, doi: 10.3847/1538-4357/aba621

Klein, K.-L., & Dalla, S. 2017, SSRv, 212, 1107, doi: 10.1007/s11214-017-0382-4

Kliem, B., & Török, T. 2006, PhRvL, 96, 255002, doi: 10.1103/PhysRevLett.96.255002

Kollhoff, A., Kouloumvakos, A., Lario, D., et al. 2021, A&A, 656, A20, doi: 10.1051/0004-6361/202140937

Koomen, M. J., Detwiler, C. R., Brueckner, G. E., Cooper, H. W., & Tousey, R. 1975, ApOpt, 14, 743, doi: 10.1364/AO.14.000743

Kopp, R. A., & Pneuman, G. W. 1976, SoPh, 50, 85, doi: 10.1007/BF00206193

Kouloumvakos, A., Rouillard, A. P., Wu, Y., et al. 2019, ApJ, 876, 80, doi: 10.3847/1538-4357/ab15d7

Kouloumvakos, A., Vourlidas, A., Rouillard, A. P., et al. 2020, ApJ, 899, 107, doi: 10.3847/1538-4357/aba5a1

Kouloumvakos, A., Nindos, A., Valtonen, E., et al. 2015, A&A, 580, A80, doi: 10.1051/0004-6361/201424397

Krucker, S., & Lin, R. P. 2000, ApJL, 542, L61, doi: 10.1086/312922

Kühl, P., & Heber, B. 2019, Space Weather, 17, 84, doi: 10.1029/2018SW002114

Lario, D., Kwon, R. Y., Balmaceda, L., et al. 2020, ApJ, 889, 92, doi: 10.3847/1538-4357/ab64e1

Lario, D., Richardson, I. G., Palmerio, E., et al. 2021, ApJ, 920, 123, doi: 10.3847/1538-4357/ac157f

Lario, D., Wijsen, N., Kwon, R. Y., et al. 2022, ApJ, 934, 55, doi: 10.3847/1538-4357/ac6efd

Laurenza, M., Cliver, E. W., Hewitt, J., et al. 2009, Space Weather, 7, S04008, doi: 10.1029/2007SW000379

Lemen, J. R., Title, A. M., Akin, D. J., et al. 2012, SoPh, 275, 17, doi: 10.1007/s11207-011-9776-8

Leske, R. A., Cummings, J. R., Mewaldt, R. A., Stone, E. C., & von Rosenvinge, T. T. 1995, ApJL, 452, L149, doi: 10.1086/309718

Leske, R. A., Christian, E. R., Cohen, C. M. S., et al. 2020, ApJS, 246, 35, doi: 10.3847/1538-4365/ab5712

Li, G., Moore, R., Mewaldt, R. A., Zhao, L., & Labrador, A. W. 2012, SSRv, 171, 141, doi: 10.1007/s11214-011-9823-7

Li, G., & Zank, G. P. 2005, in International Cosmic Ray Conference, Vol. 1, 29th International Cosmic Ray Conference (ICRC29), Volume 1, 173

Linker, J. A., Caplan, R. M., Downs, C., et al. 2017, ApJ, 848, 70, doi: 10.3847/1538-4357/aa8a70

Lintunen, J., & Vainio, R. 2004, A&A, 420, 343, doi: 10.1051/0004-6361:20034247

Luhmann, J. G., Curtis, D. W., Schroeder, P., et al. 2008, SSRv, 136, 117, doi: 10.1007/s11214-007-9170-x

Magara, T., Mineshige, S., Yokoyama, T., & Shibata, K. 1996, ApJ, 466, 1054, doi: 10.1086/177575

Malandraki, O. E., & Crosby, N. B. 2018, in Astrophysics and Space Science Library, Vol. 444, Solar Particle Radiation Storms Forecasting and Analysis, ed. O. E. Malandraki & N. B. Crosby, 1–26, doi: 10.1007/978-3-319-60051-2_1

Mann, G., Aurass, H., Klassen, A., Estel, C., & Thompson, B. J. 1999, in ESA Special Publication, Vol. 446, 8th SOHO Workshop: Plasma Dynamics and Diagnostics in the Solar Transition Region and Corona, ed. J. C. Vial & B. Kaldeich-Schü, 477

Mason, G. M., Ho, G. C., Allen, R. C., et al. 2021a, A&A, 656, L1, doi: 10.1051/0004-6361/202039752

Mason, G. M., Cohen, C. M. S., Ho, G. C., et al. 2021b, A&A, 656, L12, doi: 10.1051/0004-6361/202141310

Masuda, S., Kosugi, T., Hara, H., Tsuneta, S., & Ogawara, Y. 1994, Nature, 371, 495, doi: 10.1038/371495a0

McComas, D. J., Christian, E. R., Cohen, C. M. S., et al. 2019, Nature, 576, 223, doi: 10.1038/s41586-019-1811-1

Mewaldt, R. A., Cohen, C. M. S., Cook, W. R., et al. 2008, SSRv, 136, 285, doi: 10.1007/s11214-007-9288-x

Miller, J. A., Cargill, P. J., Emslie, A. G., et al. 1997, J. Geophys. Res., 102, 14631, doi: 10.1029/97JA00976

Mitchell, D. G., Giacalone, J., Allen, R. C., et al. 2020, ApJS, 246, 59, doi: 10.3847/1538-4365/ab63cc

Mitchell, J. G., De Nolfo, G. A., Hill, M. E., et al. 2021, ApJ, 919, 119, doi: 10.3847/1538-4357/ac110e

Moreton, G. E. 1960, AJ, 65, 494, doi: 10.1086/108346

Moreton, G. E., & Ramsey, H. E. 1960, PASP, 72, 357, doi: 10.1086/127549

Moses, D., Clette, F., Delaboudinière, J. P., et al. 1997, SoPh, 175, 571, doi: 10.1023/A:1004902913117

Muhr, N., Veronig, A. M., Kienreich, I. W., et al. 2014, SoPh, 289, 4563, doi: 10.1007/s11207-014-0594-7

Müller, D., St. Cyr, O. C., Zouganelis, I., et al. 2020, A&A, 642, A1, doi: 10.1051/0004-6361/202038467

Munro, R. H., Gosling, J. T., Hildner, E., et al. 1979, SoPh, 61, 201, doi: 10.1007/BF00155456

Narukage, N., Hudson, H. S., Morimoto, T., et al. 2002, ApJL, 572, L109, doi: 10.1086/341599

Nitta, N. V., Aschwanden, M. J., Freeland, S. L., et al. 2014, SoPh, 289, 1257, doi: 10.1007/s11207-013-0388-3

Nitta, N. V., Reames, D. V., De Rosa, M. L., et al. 2006, ApJ, 650, 438, doi: 10.1086/507442

Nitta, N. V., Schrijver, C. J., Title, A. M., & Liu, W. 2013, ApJ, 776, 58, doi: 10.1088/0004-637X/776/1/58

Oetliker, M., Klecker, B., Hovestadt, D., et al. 1997, ApJ, 477, 495, doi: 10.1086/303679

Ogawara, Y., Takano, T., Kato, T., et al. 1991, SoPh, 136, 1, doi: 10.1007/BF00151692

Onsager, T., Grubb, R., Kunches, J., et al. 1996, Society of Photo-Optical Instrumentation Engineers (SPIE) Conference Series, Vol. 2812, Operational uses of the GOES energetic particle detectors, ed. E. R. Washwell, 281–290, doi: 10.1117/12.254075

Pallavicini, R., Serio, S., & Vaiana, G. S. 1977, ApJ, 216, 108, doi: 10.1086/155452

Pan, Z. H., Wang, C. B., Wang, Y., & Xue, X. H. 2011, SoPh, 270, 593, doi: 10.1007/s11207-011-9763-0

Papaioannou, A., Sandberg, I., Anastasiadis, A., et al. 2016, Journal of Space Weather and Space Climate, 6, A42, doi: 10.1051/swsc/2016035

Parenti, S. 2014, Living Reviews in Solar Physics, 11, 1, doi: 10.12942/lrsp-2014-1

Parker, E. N. 1957, J. Geophys. Res., 62, 509, doi: 10.1029/JZ062i004p00509

—. 1958, ApJ, 128, 664, doi: 10.1086/146579

Patzold, M., Bird, M. K., Volland, H., et al. 1987, SoPh, 109, 91, doi: 10.1007/BF00167401

Pesnell, W. D., Thompson, B. J., & Chamberlin, P. C. 2012, SoPh, 275, 3, doi: 10.1007/s11207-011-9841-3

Petschek, H. E. 1964, Magnetic Field Annihilation, Vol. 50, 425

Posner, A. 2007, Space Weather, 5, 05001, doi: 10.1029/2006SW000268

Reames, D. V. 1995, Reviews of Geophysics, 33, 585, doi: 10.1029/95RG00188

—. 1999, SSRv, 90, 413, doi: 10.1023/A:1005105831781

—. 2009a, ApJ, 693, 812, doi: 10.1088/0004-637X/693/1/812

—. 2009b, ApJ, 706, 844, doi: 10.1088/0004-637X/706/1/844

—. 2013, SSRv, 175, 53, doi: 10.1007/s11214-013-9958-9

Reid, H. A. S., & Ratcliffe, H. 2014, Research in Astronomy and Astrophysics, 14, 773, doi: 10.1088/1674-4527/14/7/003

Richardson, I. G., von Rosenvinge, T. T., Cane, H. V., et al. 2014, SoPh, 289, 3059, doi: 10.1007/s11207-014-0524-8

Riley, P., Lionello, R., Mikić, Z., & Linker, J. 2008, ApJ, 672, 1221, doi: 10.1086/523893

Rodriguez, J. V., Sandberg, I., Mewaldt, R. A., Daglis, I. A., & Jiggens, P. 2017, Space Weather, 15, 290, doi: 10.1002/2016SW001533

Rouillard, A. P., Sheeley, N. R., Tylka, A., et al. 2012, ApJ, 752, 44, doi: 10.1088/0004-637X/752/1/44

Rouillard, A. P., Plotnikov, I., Pinto, R. F., et al. 2016, ApJ, 833, 45, doi: 10.3847/1538-4357/833/1/45

Saito, K., Poland, A. I., & Munro, R. H. 1977, SoPh, 55, 121, doi: 10.1007/BF00150879

Scherrer, P. H., Schou, J., Bush, R. I., et al. 2012, SoPh, 275, 207, doi: 10.1007/s11207-011-9834-2

Schwadron, N. A., Bale, S., Bonnell, J., et al. 2020, ApJS, 246, 33, doi: 10.3847/1538-4365/ab5527

Sheeley, N. R., J., Bohlin, J. D., Brueckner, G. E., et al. 1975, SoPh, 45, 377, doi: 10.1007/BF00158457

Sheeley, N. R., Wang, Y. M., Hawley, S. H., et al. 1997, ApJ, 484, 472, doi: 10.1086/304338

Shibata, K. 1996, Advances in Space Research, 17, 9, doi: 10.1016/0273-1177(95)00534-L

Shibata, K. 1997, in ESA Special Publication, Vol. 404, Fifth SOHO Workshop: The Corona and Solar Wind Near Minimum Activity, ed. A. Wilson, 103

—. 1999, Ap&SS, 264, 129, doi: 10.1023/A:1002413214356

Shibata, K., & Magara, T. 2011, Living Reviews in Solar Physics, 8, 6, doi: 10.12942/lrsp-2011-6

Shibata, K., Masuda, S., Shimojo, M., et al. 1995, ApJL, 451, L83, doi: 10.1086/309688

Smart, D. F., & Shea, M. A. 1996, Advances in Space Research, 17, 113, doi: 10.1016/0273-1177(95)00520-O

Stansby, D., Yeates, A., & Badman, S. 2020, The Journal of Open Source Software, 5, 2732, doi: 10.21105/joss.02732

Sturrock, P. A. 1966, Nature, 211, 695, doi: 10.1038/211695a0

Sun, X., Bobra, M. G., Hoeksema, J. T., et al. 2015, ApJL, 804, L28, doi: 10.1088/2041-8205/804/2/L28

Sweet, P. A. 1958, in IAU Symposium, Vol. 6, Electromagnetic Phenomena in Cosmical Physics, ed. B. Lehnert, 123

Temmer, M., Veronig, A. M., Kontar, E. P., Krucker, S., & Vršnak, B. 2010, ApJ, 712, 1410, doi: 10.1088/0004-637X/712/2/1410

Thernisien, A. F. R., Howard, R. A., & Vourlidas, A. 2006, ApJ, 652, 763, doi: 10.1086/508254

Thompson, B. J., Plunkett, S. P., Gurman, J. B., et al. 1998, Geophys. Res. Lett., 25, 2465, doi: 10.1029/98GL50429

Toriumi, S., Schrijver, C. J., Harra, L. K., Hudson, H., & Nagashima, K. 2017, ApJ, 834, 56, doi: 10.3847/1538-4357/834/1/56

Torsti, J., Valtonen, E., Lumme, M., et al. 1995, SoPh, 162, 505, doi: 10.1007/BF00733438

Tousey, R. 1973, in Space Research Conference, Vol. 2, 713–730

Trottet, G., Samwel, S., Klein, K. L., Dudok de Wit, T., & Miteva, R. 2015, SoPh, 290, 819, doi: 10.1007/s11207-014-0628-1

Tsuneta, S. 1996, ApJ, 456, 840, doi: 10.1086/176701

Tsuneta, S., Hara, H., Shimizu, T., et al. 1992, PASJ, 44, L63

Tsurutani, B. T., Gonzalez, W. D., Lakhina, G. S., & Alex, S. 2003, Journal of Geophysical Research (Space Physics), 108, 1268, doi: 10.1029/2002JA009504

Tylka, A. J., Cohen, C. M. S., Dietrich, W. F., et al. 2003, in International Cosmic Ray Conference, Vol. 6, International Cosmic Ray Conference, 3305

Uchida, Y. 1968, SoPh, 4, 30, doi: 10.1007/BF00146996

—. 1974, SoPh, 39, 431, doi: 10.1007/BF00162436

Ueno, S., Nagata, S., Kitai, R., & Kurokawa, H. 2004, in Astronomical Society of the Pacific Conference Series, Vol. 325, The Solar-B Mission and the Forefront of Solar Physics, ed. T. Sakurai & T. Sekii, 319

Vainio, R., Valtonen, E., Heber, B., et al. 2013, Journal of Space Weather and Space Climate, 3, A12, doi: 10.1051/swsc/2013030

Van Hollebeke, M. A. I., Ma Sung, L. S., & McDonald, F. B. 1975, SoPh, 41, 189, doi: 10.1007/BF00152967

von Rosenvinge, T. T., Reames, D. V., Baker, R., et al. 2008, SSRv, 136, 391, doi: 10.1007/s11214-007-9300-5

Webb, D. F., & Howard, T. A. 2012, Living Reviews in Solar Physics, 9, 3, doi: 10.12942/lrsp-2012-3

Whitman, K., Egeland, R., Richardson, I. G., et al. 2022, Advances in Space Research, doi: https://doi.org/10.1016/j.asr.2022.08.006

Wiedenbeck, M. E., Bučík, R., Mason, G. M., et al. 2020, ApJS, 246, 42, doi: 10.3847/1538-4365/ab5963

Wild, J. P., Smerd, S. F., & Weiss, A. A. 1963, ARA&A, 1, 291, doi: 10.1146/annurev.aa.01.090163.001451

Wimmer-Schweingruber, R. F., Janitzek, N. P., Pacheco, D., et al. 2021, A&A, 656, A22, doi: 10.1051/0004-6361/202140940

Xie, H., Ofman, L., & Lawrence, G. 2004, Journal of Geophysical Research (Space Physics), 109, A03109, doi: 10.1029/2003JA010226

Yashiro, S., Gopalswamy, N., Michalek, G., et al. 2004, Journal of Geophysical Research (Space Physics), 109, A07105, doi: 10.1029/2003JA010282

Zhang, J., Dere, K. P., Howard, R. A., & Vourlidas, A. 2004, ApJ, 604, 420, doi: 10.1086/381725

Zhang, J., Richardson, I. G., Webb, D. F., et al. 2007, Journal of Geophysical Research (Space Physics), 112, A10102, doi: 10.1029/2007JA012321

Zhang, M., Qin, G., & Rassoul, H. 2009, ApJ, 692, 109, doi: 10.1088/0004-637X/692/1/109